Department of Medical Physics and Biomedical Engineering
University College London
University of London

Haemoglobin sensing with optical spectroscopy during minimally invasive procedures

Rocío del Pilar Soto Astorga

Supervisors:

Prof. Jeremy C. Hebden
Dr. Adrien E. Desjardins

A thesis submitted for the degree of Doctor of Philosophy at
University College London

2014

I, Rocio del Pilar Soto Astorga confirm that the work presented in this thesis is my own. Where information has been derived from other sources, I confirm that this has been indicated in the thesis.

Signature

Abstract

Many clinical procedures involve the use of minimally invasive devices such as needles and catheters. Providing increased information about tissues that are adjacent to the device tips could reduce the probability of complications in these procedures. Optical fibres are well suited for integration into medical devices and they can be used to provide information relevant to tissue characterisation.

This dissertation is centred on the integration of optical fibres into needles and catheters to obtain information about haemoglobin. In two studies, reflectance spectroscopy was performed. Two optical fibre geometries were tested, and for each, Monte Carlo simulations were used to estimate the reflectance values and the photon penetration depths. In the first study, reflectance spectroscopy was performed with a double clad fibre. Experiments using expired human red blood cells were performed to determine the sensitivity of the measurements to oxygen saturation variation at physiological levels. Distinction between normal oxygen saturation values in veins and arteries was possible, making this fibre potentially useful to verify needle placement during a venous catheterisation or during a transseptal puncture. In the second study, two polymer optical light fibres were directly integrated into an epidural catheter. This optical catheter was tested during an ex-vivo swine laminectomy in the lumbar region. Another ex-vivo experiment was performed on chicken wings to discern blood vessels from other tissues. This information could be used during anaesthesic procedures to reduce the risk of toxicity from an intravascular injection.

With reflectance spectroscopy, the depth in tissue from which signal is obtained is limited by the inter-fibre distance. This limitation motivated a third study, in which photoacoustic imaging was used to obtain image contrast for haemoglobin.

The results of the three studies suggest that the integration of optical fibres into medical devices during minimally invasive procedures can allow for clinically

relevant measurements of tissue properties in real-time.

Acknowledgements

I thank God for all the chances.
This thesis is for my grandmother.

This thesis as well as the wonderful three years and some that it took to finish, would not have been possible without the gracious help of many.

Firstly, I want to express my love to my grandmother and grandfather, to whom I owe what I am. I want to thank Suna for being always kind and supportive during this stage of our lives, and for enduring my anxiety during this journey. I would like to thank my parents, my brother, and all my family for their support during my PhD.

I would like to thank my supervisors Prof. Jem Hebden and Dr. Adrien Desjardins, for their constant support and guidance. Jem was always accessible, whether I needed advice on a particular topic or guidance from project to project. I am also indebted to him for his wise council and generosity offered through tough times. Adrien taught me the lot of what I know about communicating ideas through scientific writing. I was always enriched by our discussions on the topics throughout this thesis and hope that I have been able to learn if only a bit of his ability of communicating results to a wider audience.

My special thanks to our medical collaborators Dr. Simeon West and Dr. Malcolm Finlay, for their crucial contributions to the projects described herein. I also wish to acknowledge the help provided by Dr. Edward Zhang during my constant requests in the first year.

This work would not have been possible without the constant mentoring from Dr. Jean Martial Mari. He has been a constant source of all sorts of advice. His daily support and encouragement (and constant influx of chocolate) helped me keep going.

I'm also grateful for all the memories that I have made with my colleagues in the department of Medical Physics, especially to those in the BORL group with whom I spent most of the time at the office. I will also remember my time at the lab with the invaluable help from Daniil and Jean Martial during my last year .

Thanks to my old and new friends, to Monica, Mauricio, Juan, Itzel, Paulina, Carrie, Isabel, Edgar, Joanna...

Contents

List of Tables

List of Figures

Introduction

Motivation

Open surgery is a procedure involving incisions or punctures large enough to access a cavity of a patient's body. Although direct visualization during surgery gives surgeons control over the target and instruments, surgery is traumatic to the patient, involving high-risk procedures that may endanger the patient's life, and which require a substantial period of time for recovery. While risks associated with open surgery depend on the procedure, there are potential complications common to all types of surgery, such as excess bleeding and accidental tissue damage [Kama et al., 2001; Nuttall et al., 2000].

Minimally invasive procedures, which require a minute incision into the body, are being widely explored as alternatives to open surgery, resulting in less trauma to the patient and shorter convalescence periods [Kehlet and Wilmore, 2002; Hu et al., 2009]. During these procedures, an instrument enters the body through a small incision or opening, and is monitored and manoeuvred from the outside. For instance, a number of cardiac procedures such as radio-frequency ablation for atrial fibrillation [1], percutaneous repair of atrial septal defect [2], and advance aid for devices sent to mitral valves repair [Babaliaros et al., 2008] make use of catheters and needles to get access to the heart. Another example of invasive procedures are needle biopsies that provide information when evaluating suspicious masses through the ex-situ interrogation of samples aspirated directly out of the patient's tissue [Crockett, 2011; Meloni et al., 2002; Boschiero et al., 1992]. Cannulas and needles also enable the practising clinician to reach otherwise inaccessible regions of the patient's body during anaesthetic and analgesic techniques. In this case, a drug is injected into

---

[1] Atrial fibrillation is a condition in which an abnormal heart rhythm is present due to disorganised electrical impulses.

[2] Atrial septal defect refers to a congenital defect in which the foramen ovale, a hole between the atria that bypass the lungs in the fetus heart, was not entirely closed after birth.

tissue surrounding nerves, the epidural space, or into a vein in order to prepare the patient for surgery, or to mitigate pain [The Royal College of Anaesthetists].

The use of interventional devices comes at the cost of losing visibility and control over the tools inserted into the patient. Some procedures such as laparoscopy commonly introduce probes up to 12 mm in diameter [McKay and Blake, 2006] which provide a relatively large field of view that enables the use of a lens and CCD detector to acquire an image of tissue at the distal end. However, management of smaller probes such as needles and catheters require additional equipment for their correct placement, such as ultrasound or X-ray imaging systems.

There are several potential risks linked to needle and catheter misplacement such as complications derived from pseudoaneurysm [3] and bleeding that may occur during cardiac catheterisation [Chandrasekar et al., 2001; Cale and Constantino, 2012], and nerve puncture and systemic toxicity during anaesthesiology procedures [4]. Therefore, to obtain the full benefits of minimally invasive interventions and anaesthetic and analgesic techniques, the physician must not only correctly guide the intervention tools towards their target, but also be in complete control of the instrument when navigating through critical structures in the intervention path. Because of their widespread use, increasing placement accuracy by determining information about the tissue at the distal end of these devices would considerably improve the quality of health care and reduce the probability of tissue damage.

Many directions have been taken in creating novel technologies for visualizing the placement and location of invasive probes. Examples of these technologies include ultrasound and X-radiography. X-radiography produces images by sending an X-ray to the body and detecting the non absorbed signal, while ultrasound imaging, on the other hand, delivers high frequency sound waves and processes the signal from the waves being reflected by the tissue. X-ray and ultrasound guided placement is routine in critical interventions on many organs such as the liver, brain, pancreas kidney, lungs, and diverse types of biopsies; this guidance is also commonly used during operations where fluid aspiration, agent injection, catheter introduction is needed [Machi et al., 1990]; however, these tools are expensive, cannot accurately differentiate between tissues, and may rely on ionizing radiation. Recent research have also explored the use of computed tomography for needle guidance [Wagner, 2004; Kranz et al., 2012; Koizuka et al., 2014]. In computed tomography techniques,

---

[3]Pseudoaneurysm is a blood leakage from an injured blood vessel. The blood accumulates between the vessel wall and adjacent tissues [UC Davis Vascular Center].

[4]Systemic toxicity refers to a number of complications associated to the entrance of anaesthetic to the cerebral circulation [Mulroy, 2002].

the patient is exposed to X-ray radiation in order to acquire 2D images of the needles, guide wires, dilators, or catheters that are being placed, but this relies again in some amount of radiation being delivered to the body.

To place an invasive device in a target tissue stereotactic surgery can be used. This technique employs an external mechanical device that provides a referential frame to soft tissues, but can fail if patient movement occurs [Dillon et al., 2005; Meloni et al., 2002]. If the final position of a device needs to be verified, for instance during venous cannulation and some anaesthesiology techniques, an aspiration can be perform to evaluate the tissues at the tip's vicinity. However, this technique may not yield reliable information in some cases. For instance, withdrawn blood originally regarded as venous from its apparent dark colour, may reveal to be arterial blood after a large cannula is inserted and pulsatile flow is observed [Guilbert et al., 2008; Shah et al., 2004; Arendt and Segal, 2008].

In an effort to address the need of correct placement verification during minimally invasive procedures, there has been an increase in the use of optical fibre technology based on in situ tissue differentiation. Optical fibres can be easily coupled into needles and catheters, and can be used to differentiate tissues by exploiting their ability to resolve the tissue's spectral absorbing and scattering properties. Recent studies have implemented the use of optical methods such as spectroscopy and optical coherence tomography to carry out diagnosis of tissues of interest, allowing for real time and in situ clinical assessment [Quirk et al., 2011; Utzinger and Richards-Kortum, 2003; Lin et al., 2001; Wang et al., 2009]. The devices used to induce and gather information about the histological optical response, mainly comprised of optical fibre systems, can be easily inserted into commonly used clinical probes. Once the probe is inserted, no further damage to the tissue is made since, to perform optical spectroscopy analysis, only the spectral response of the tissue is needed. The spectrum can be obtained by simply illuminating the regions of interest and detecting the back-reflected response through the same or a different fibre. The fast acquisition and analysis of spectral data may allow for real-time diagnosis.

In the course of collaborating with physicians in the UCL hospital, I observed a pervasive need for haemoglobin detection using relatively simple equipment. This need was present in different areas such as cardiac cathetherisations and anaesthesiology procedures. To address these needs, reflectance spectroscopy with a double clad system was identified as a possible optical sensor during catheterisations, while an optical epidural catheter working under the same principle was proposed to monitor continuous epidural anaesthesia. Further, for the acquisition of new pho-

toacoustic instrumentation, and the increased interest of prompt blood detection, I explored the potential use of photoacoustic imaging to interrogate deeper tissues with interventional devices.

Project aims

The location of blood vessels is of paramount importance during needle and catheter placement, and as mentioned above, accidental puncture of a blood vessel may produce complications such as bleeding and toxicity. Therefore a question central to the present study is whether optical techniques can be used in combination with needles and catheters to provide pertinent information on blood within a region of interest and in surrounding tissues, reducing the likelihood of trauma.

The general scenario is shown in Fig. 1, where a needle is to be inserted in a tissue containing different structures such as blood vessels, nerves, or ligaments. Depending on the procedure one of these structures is being targeted. Puncturing another structure may carry out different risks ranging from an unsuccessful procedure with non severe impact [Collier, 1996], to life-threatening complications [Guilbert et al., 2008].
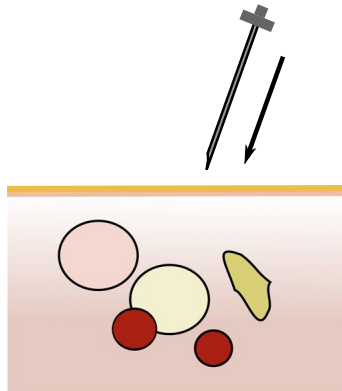
Figure 1: During minimally invasive interventions and anaesthetic techniques the physician must guide the device towards their target, while being aware of critical structures in the intervention path.

Unintended puncture of a blood vessel can lead to dangerous consequences such as bleeding and toxicity [Chandrasekar et al., 2001; Cale and Constantino, 2012; Faccenda and Finucane, 2001]. The aim of this thesis is to tackle the problem of preventing unintentional vascular puncture by optically detecting the presence of

haemoglobin.
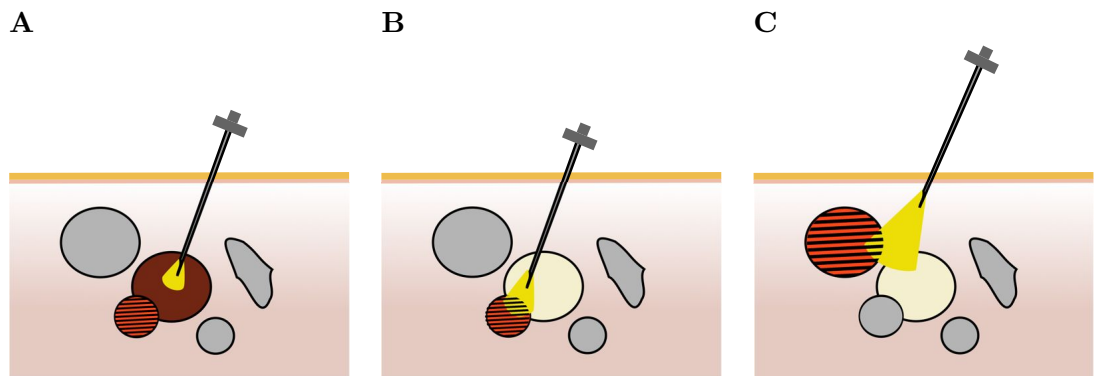
Figure 2: The three scenarios to be discussed in this thesis. **A** Verification of the device placement within a vein. **B** Continuous monitoring of the device to prevent migration into a blood vessel. **C** Prompt detection of vascularities.

Three scenarios have been distinguished and will be explored in this thesis. In the first one, the device is believed to have reached the target, but confirmation is crucial before the next medical gesture is taken (Fig. 2 A). This situation will be addressed using a very small fibre ($125\mu m$ diameter) for the differentiation between venous and arterial blood, which may be useful during a venous catheterisation. Here, the dimensions of the fibre would allow for prompt verification of correct placement of needles (or catheters) if the fibre is embedded into their small accessories of it such as stylets or guidewires (or finders - small needles). Commonly during a catheterisation a small needle (e.g. 22G with 0.718/0.413mm OD/ID) is first used to find the vessel. After the vein is located, a larger needle may be used to introduce a guide-wire to insert the catheter [Oliver Jr. et al., 1997]. A major risk is to puncture an artery with the large bore catheter, therefore it is desirable to detect any incorrect placement in the first stages of the procedure where small diameter devices are being used.

For the second scenario, the device needs to stay within the target for a period of time, in which case its location needs to be monitored given the proximity of risky structures (Fig. 2 B). An example of this is the migration of epidural catheters delivering anaesthesia. Hence an optical epidural catheter was be investigated in this thesis.

The last scenario depicted in Fig. 2 C corresponds to the case in which the target need to be identified among other structures prior to further advancement of the device. While the first two situations were addressed by means of optical reflectance spectroscopy, for the last case photoacoustic imaging was used since its

deeper penetration capabilities allow the identification of blood while the device is not yet in contact with any structure.

Thesis Overview

The structure of this thesis is as follows. In the first chapter a review will be presented of the theory associated with the technologies explored during this project, such as reflectance spectroscopy and photoacoustic imaging.

Chapter two explores the scenario in which it is necessary to determine when an invasive probe has reached its target, and prevent further advancement. This is important in order to avoid accidental puncturing of an important structure and to verify the device location prior to procedures such as drug injection. Examples where this situation arises include the confirmation of venous puncture during a venous cannulation, and the assessment of venous-arterial blood during a transseptal needle procedure. In this work, a small double clad fibre was tested with optical reflectance spectroscopy for its use in venous-arterial blood differentiation at the very tip of the device. The small fibre diameter (125 µm) was chosen to be easily fitted within small needles. Chapter two also gives an overview of the Monte Carlo algorithm that was used to estimate the viability of the method for specific probe geometries.

Chapter three explores the situation of a correctly placed invasive device whose position needs to be monitored to prevent any movement into a possibly dangerous location. Specifically, the case is examined of an epidural catheter used during anaesthetic procedures. The catheter is placed into the epidural space to provide gradual delivery of medication. The movement of the catheter into a blood vessel is a potential risk that can lead to systemic toxicity. Reflectance spectroscopy was employed with a custom catheter with embedded optical guides for the detection of blood-rich structures in the vicinity of the catheter tip.

With reflectance spectroscopy, the tissue depth at which a signal can be obtained is limited by the inter-fibre distance and the attenuation of light. This limits its use for a third scenario, in which a target needs to be identified among other tissues before any further medical procedure takes place. This issue is addressed in chapter four, where the use of photoacoustic imaging is explored to obtain image contrast based on haemoglobin concentration. This feature may allow one to detect blood vessels prior to further advance of a needle during insertion, which may be important in situations such as nerve blocks to avoid bleeding and toxicity.

This thesis explores the use of optical methods coupled to invasive devices in order to securely place them during an invasive procedure. The results of the experimental work and simulations presented here for the detection of blood in the three aforementioned situations of a device insertion, encourage the integration of optical fibres into needles and catheters to improve patient's safety.

Chapter 1

Light in Tissue

When light interacts with matter, several phenomena such as light reflection, emission, absorption, or scattering can take place depending on the object in question, and normally occur as a function of its material composition and geometry. Optical spectroscopy studies these phenomena as a function of wavelength. When applying optical spectroscopy methodologies in clinical settings, the technique is mostly concerned with the analysis of light absorption, scattering and fluorescence, since these are the main interactions between biological tissue and light.

When a photon interacts with a tissue molecule, it raises the energy level of the molecule. The molecule then may change back to its ground state, producing elastic scattering, or alternatively the energy may be transformed into another form (e.g. thermal energy), in which case it is said that the molecule has absorbed the photon.

In the case of extremely heterogeneous and composite objects such as biological samples, the observed scattering and absorption is a function of each tissue component. Thus, measuring the aggregate scattering and absorption values of a sample of interest can give insights into the characteristics of its components.

Fluorescence and inelastic scattering, in which energy is not conserved due to either an increase or a loss of energy, can occur in tissue but attribute insignificantly to the methods explored in this thesis. Thus, the discussion below will only focus on the dominant interactions of absorption and scattering.

1.1   Light-Tissue interactions

1.1.1   Absorption

The absorption of light by an idealised volume of identical molecules can be expressed in terms of the absorption coefficient μ_a (in mm^{-1}), which represents the probability that a photon is absorbed by the medium per unit pathlength. The reciprocal of μ_a is called the mean absorption length and denotes the average distance travelled before a photon suffers absorption.

Assuming a homogeneous medium composed by absorbing molecules, herein called chromophores, immersed in a non-absorbing medium, the absorption coefficient of this medium is defined as:

$$\mu_a = \rho_a \sigma_a \tag{1.1}$$

where ρ_a is the volume density of the chromophore in the medium, and σ_a is the absorption cross section. The absorption cross section is a measure of the rate at which energy is being absorbed from an incident plane wave.
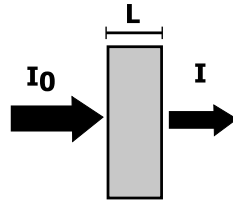
Figure 1.1: Absorption of light by a tissue layer of thickness L

In a layer of a homogeneous absorbing medium with no scattering (see Fig. 1.1), the incident light intensity I_0 decreases exponentially according to Beer's Law as shown in Eq. 1.2 where I is the emergent intensity, and L is the layer thickness.

$$I = I_0 e^{-\mu_a L} \tag{1.2}$$

In a medium with more than one type of chromophore, the total absorption coefficient follows a linear dependency on the absorption coefficients of all the chromophores. This can be expressed by:

$$\mu_a = \ln(10) \sum_{i=1}^{n} \epsilon_i \, c_i \qquad (1.3)$$

where ϵ_i is the specific extinction coefficient in $\frac{mm^{-1}}{M}$, and c_i is the molar concentration in M ($\frac{mol}{L}$), for the ith chromophore. The specific extinction coefficient measures the absorption capability of a given chromophore.

In biomedical applications, the optical window, or therapeutic window, is the range of optical wavelengths from 600 to 1300 nm at which biological tissue has a relatively low absorption. This optical window is limited by the haemoglobin absorption at the shorter wavelengths and by the water absorption at the larger wavelengths. In addition to haemoglobin and water, other chromophores in tissue are melanin, lipids, proteins and enzymes. The tissue's total absorption coefficient is determined by the different concentrations of these key elements. Figure 1.2 shows the extent of this wavelength range, and the absorption coefficient of water, fat and whole blood (80 % oxygenated) to illustrate their low absorption within the window.
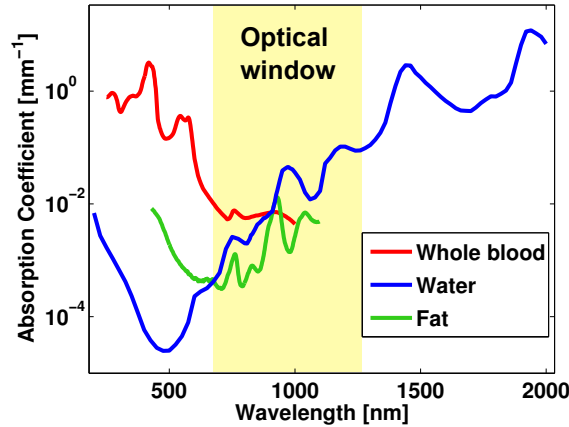
Figure 1.2: Optical window for which principal chromophores in tissue (water and the haemoglobin present in blood) exhibit low absorption. Fat is also shown in the figure for comparison (data from [Prahl]).

The importance of water and haemoglobin in tissues also resides in their quantities found in the body. Water in tissue accounts for about 71% to 74% of the body weight [Friedl et al., 1992], while a healthy individual has approximately 5 L of blood [Pallister and M.S., 2011]. In turn, normal concentrations of haemoglobin, the protein present in the red blood cells, are from 13.3 to 17.7 g/dL in men, and from 11.7 to 15. 7 g/dL in women [Pallister and M.S., 2011]. Blood is differen-

tially distributed between different kind of tissues. For instance, the liver, lungs and heart are among the blood richest tissues, while muscles, skin and adipose tissue are among the lowest blood content [Yu et al., 1991].

Absorption by blood

Blood is composed of about 45% red blood cells, 1% white blood cells and platelets, and 54% plasma (which is more than 90% water) [Rogers, 2010]. Therefore the principal absorbers in blood are water and haemoglobin contained in the red blood cells.

There are various forms of haemoglobin such as met-haemoglobin, carboxy-haemoglobin, deoxy-haemoglobin, and oxy-haemoglobin [Bunn and Forget, 1986] from which oxy and deoxy-haemoglobin are found in major concentrations [1]. Fig. 1.3 shows the extinction coefficient of these two forms for a total haemoglobin concentration of 15 g/dL.
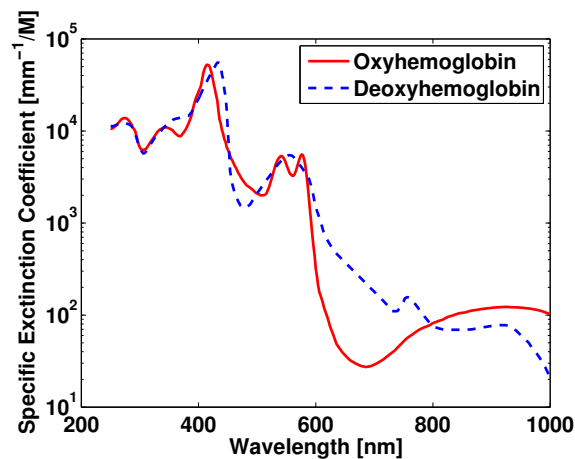
Figure 1.3: Specific extinction coefficient of two haemoglobin forms: oxy and deoxy-haemoglobin (data from [Prahl]).

---

[1] Normal levels of met-haemoglobin are less than 1% of the total haemoglobin content, while for carboxyhaemoglobin normal leveles are also around 1%, but can reach up to 10% in heavy smokers [Shinton, 2007].

1.1.2   Scattering

The elastic scattering for independent scattering events [2] in a medium can be described analogously to absorption: the scattering coefficient μ_s (in mm^{-1}) is the probability of photon scattering per unit pathlength. The reciprocal of μ_s is called the scattering length and denotes the average distance travelled between consecutive scattering events. The scattering coefficient is then defined as:

$$\mu_s = \rho_s \sigma_s \tag{1.4}$$

where ρ_s is the volume density of the scatterers in the medium, and σ_s is the scattering cross section, which is a measure of the rate at which energy is being scattered out from the initial propagation of a plane wave.

The probability that the photon will be scattered into a new direction $\hat{s}$ from the initial direction $\hat{s}'$ (see Fig. 1.4) is further needed to describe the scattering into the medium. This probability is denoted by the phase function p defined as:

$$p = \frac{1}{\sigma_s} \frac{d\sigma_s}{d\Omega} \tag{1.5}$$

where the term $\frac{d\sigma_s}{d\Omega}$ is the differential scattering cross section, which describes the light scattered into a unit solid angle, on the new direction $\hat{s}$.
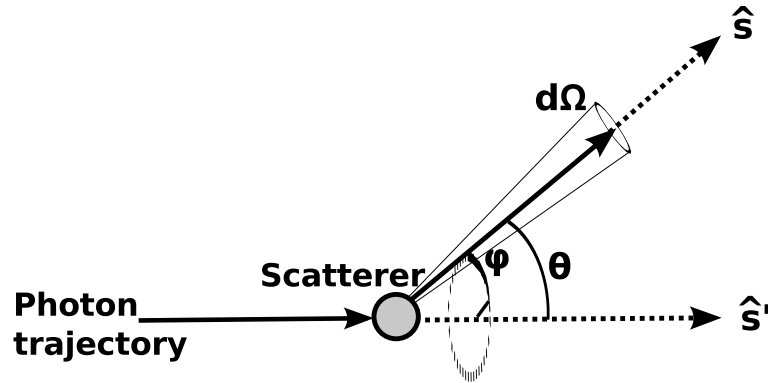
Figure 1.4: A photon initially travelling along $\hat{s}'$ is scattered into a differential solid angle $d\Omega$ about $\hat{s}$. In this figure, θ corresponds to the polar angle from the original trajectory, and φ the azimuthal angle.

---

[2]Independent scattering refers to the case in which the separation between scatterers is greater than the scatter size and the light wavelength [Wang and Wu, 2007].

The phase function is normalised according to Eq. 1.6, where $d\Omega$ is the differential solid angle. In an isotropic medium, azimuthal symmetry is assumed. Therefore, the probability distribution of the phase function can be expressed for spherical coordinates in terms of the polar angle θ (Eq. 1.7).

$$\int_{4\pi} p \, d\Omega = 1 \tag{1.6}$$

$$2\pi \int_0^\pi p(\theta) \sin\theta \, d\theta = 1 \tag{1.7}$$

Another parameter used for the characterisation of light in tissue is the average cosine of scattering, $g = \langle \cos\theta \rangle$. Commonly known as the anisotropy parameter, this dimensionless value describes the directionality of the scattered light. Values of g may vary between -1 and 1, where negative values represent a backward scattering, and positive values represent forward scattering.

The average cosine of scattering can be determined from the phase function p as shown in Eq. 1.8, and its simplification in terms of the polar angle in Eq. 1.9.

$$g = \langle \cos\theta \rangle = \int_{4\pi} p \, \cos\theta \, d\Omega \tag{1.8}$$

$$g = \langle \cos\theta \rangle = 2\pi \int_0^\pi p(\theta) \, \cos\theta \sin\theta \, d\theta \tag{1.9}$$

The Henyey-Greenstein (HG) phase function, shown in Eq. 1.10, has been widely used to describe the scattering of light in average tissue. Figure 1.5 shows the HG function describing the light propagation at different values of g. Values of g between 0.7 and 0.9 are commonly used to describe average biological tissue.

$$p(\mu) = \frac{1}{2} \frac{(1 - g^2)}{(1 + g^2 - 2g\,\mu)^{3/2}} \tag{1.10}$$

Principal scatterers in tissue are membranes, nuclei, mitochondria, and other cell components that, in total, dictate the tissue's scattering coefficient and anisotropy. The scattering coefficient depends on the sizes, distributions, and concentrations of these structures, as they create a network of refractive mismatches that shape the
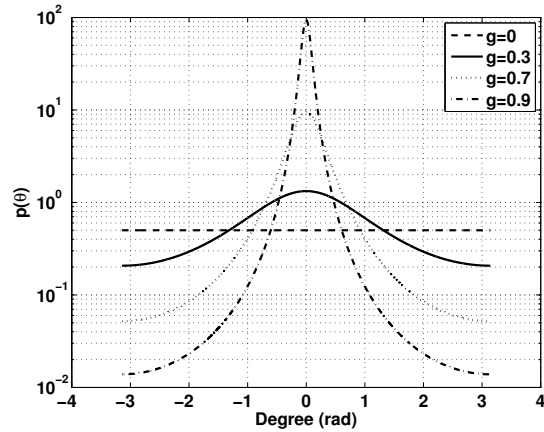
Figure 1.5: Henyey-Greenstein function illustrating the effect of different anisotropy values in the light distribution.

paths that light can take through them. The organelles mentioned above also lead to a high anisotropy for photon flow in the forward direction. Fig. 1.6 shows the approximation of the scattering for three different tissues [Bashkatov et al., 2005], where the reduced scattering coefficient, μ_s', refers to the relation $(1 - g)\mu_s$.
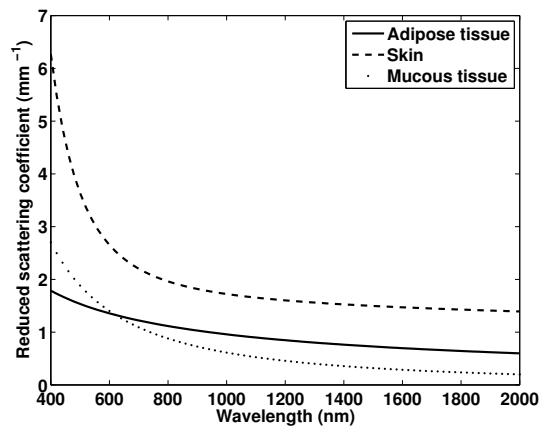
Figure 1.6: Reduced scattering coefficient from skin, adipose, and mucous tissue (data from [Bashkatov et al., 2005]).

Table 1.1: Different methods used to extract scattering properties of blood [Yaroslavsky et al., 1996; Roggan et al., 1999; Friebel et al., 2006, 2009][1]

	Hct (%)	SO_2 (%)	Shear rate (s^{-1})	Technique [2]	Wavelength (nm)	Highlights
Yaroslavsky (Whole blood)	45-46	> 98	0	Double integrating sphere and goniophotometry	632, 700-1200	g increases with wavelength, while μ'_s mostly decreases. Approximate values in the range 700-800 nm: $g \approx 0.99$, μ'_s from 70 to 75 mm^{-1}.
Roggan(a) (RBCs)	0-70	> 98	500	Double integrating sphere	633	μ_s maximum at 500 nm (40 mm^{-1}) decreasing to 30 mm^{-1} in the range 550-800 nm and a faster decrease afterwards. Values of g above 0.98 between 400 and 1400 nm.
Roggan(b) (RBCs)	5	0, 100	0-3000	Double integrating sphere	400-2500	μ'_s increase with increasing haematocrit with values between 1.5 and 2 mm^{-1} at physiological levels. No significant changes of μ'_s were observed due to oxygenation.
Friebel (2006) (RBCs)	0.84, 42.1	> 99	600	Integrating sphere	250-1100	Values of g below 0.97 from 600 to 1100 nm, and decreasing under 600 nm following Hb absorption. Between 600-1100 nm, μ'_s ranged from 1.9 to 2.27 mm^{-1}.
Friebel (2009) (RBCs)	33.2	0, 100	600	Integrating sphere	250-2000	μ_s values from 250 to 600 nm correlates to Hb absorption with a maximum at 600 nm (83-88 mm^{-1}), and a continuous decrease above 800 nm to 30 mm^{-1} at 2000 nm. Anisotropy correlates inversely with Hb absorption; after 600 nm g decreases from 0.977 to 0.96 ar 1800. Overall an increase of absorption due to SO_2 reflected a decrease of g and an increase of μ'_s.

[1] In [Roggan et al., 1999] two studies are presented, one at 633 nm analysing the variation of ..., and the other at 400 to 2500 nm to study the influence of .. These studies are referred in this table as Roggan(a) and Roggan(b) respectively.
[2] Data was analysed using Inverse Monte Carlo in these works.

Scattering of blood

Several studies have dealt with the characterization of the scattering properties of blood. These studies, however do not follow the same experimental procedures. Table 1.1, differentiates few aspects of the methods used in selected papers regarding the scattering properties of blood at physiological haematocrit [3].

For haematocrit level dependence, light travelling in blood has shown to have a scattering increment when haematocrit level increases [Roggan et al., 1999; Friebel et al., 2006]. On the other hand, studies related to oxygen saturation dependence of the scattering properties at different wavelengths [Faber et al., 2004; Friebel et al., 2009], provide reasonable evidence that there is no significant dependence to oxygen saturation; in fact, mismatches in observed and calculated spectral parameters in both studies can be traced back to the difference in sample preparation.

Phase function for blood

Two phase functions were considered for the movement of the photons in the tissue, the Gegenbauer kernel (GK) function, and the aforementioned Henyey-Greenstein (HG) function. The GK is shown in Eq. 1.11, where μ is the cosine of the polar angle: $\mu = \cos\theta$. The GK function depends on two parameters: α, and g'; the HG function, results from having the α parameter in the GK function set to 0.5 [Reynolds and McCormick, 1980]. In the particular case of the HG function, the parameter g' equals g, the average cosine of scattering.

$$ p(\mu) = \frac{\alpha g'}{\pi} \frac{(1 - g'^2)^{2\alpha}}{[(1 + g')^{2\alpha} - (1 - g')^{2\alpha}](1 + g'^2 - 2g'\,\mu)^{1+\alpha}} \tag{1.11} $$

A number of studies [Yaroslavsky et al., 1996; Hammer et al., 1998; Roggan et al., 1999; Yaroslavsky et al., 1999; Hammer et al., 2001; Friebel et al., 2006, 2009] have suggested that, when simulating light propagation in blood, the use of the GK function is more appropriate given the high directionality of the scattering. However the value assigned to the parameters α and g differs between these studies, and there is a lack of homogeneity in the methods, e.g. the haematocrit of the samples, and the wavelengths under study. It is also possible that the high anisotropy found in the aforementioned studies, is an aftermath of the imposition of a flow of the blood,

---

[3]Haematocrit (packed cell volume) refers to the volume occupied by red blood cells in the whole blood. Normal values in women range: 42 ± 5 %, and in men 47 ± 7 % [Shinton, 2007]
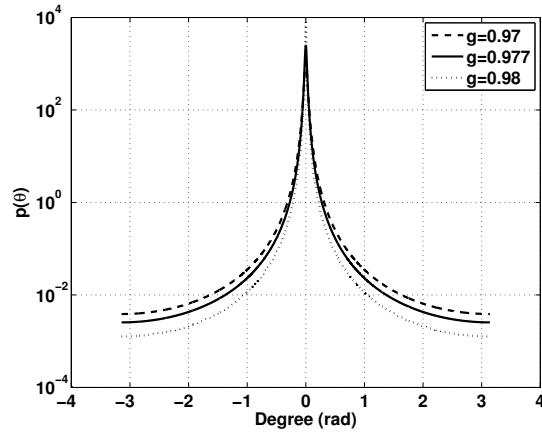
Figure 1.7: Henyey-Greenstein function for values of g used for describing light propagation in whole blood.

a condition that is not being applied in the present work.

Here, the assumption by Hammer et. al. [Hammer et al., 2001] will be used, in which the GK function is more appropriate to model highly concentrated red blood cells, while the HG function accommodates well for the modelling of scattering of red blood cells at physiological concentrations. Figure 1.7 shows the scattering distribution as obtained with the HG phase function at three values of g: 0.970, 0.977. and 0.980, found to describe light propagation in blood.

1.1.3 Refractive index

The refractive index n of a medium is defined as the ratio of the velocity of light travelling in vacuum c to the velocity of light in that medium, ν: $n = \frac{c}{\nu}$. When a plane electromagnetic wave encounters a boundary between two homogeneous media with different refractive indices, part of the wave is reflected and part is transmitted into the second medium. The angle at which the wave is being refracted into a second medium is determined by the Snell law:

$$n_i \sin \theta_i = n_t \sin \theta_t \tag{1.12}$$

where θ_i and θ_t are the angle of incidence and angle of transmission, and n_i and n_t the refractive indices of the first and second medium respectively.

On the other hand the fraction of the incident power that is being reflected (R), and transmitted (T) at a boundary between two media with different refractive
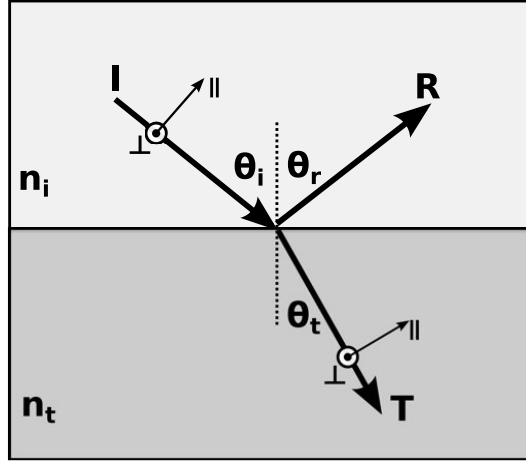
Figure 1.8: Plane of incidence with the incident wave **I**, the reflected wave **R**, and the transmitted wave **T**.

indices can be obtained by:

$$R = |r|^2; \qquad T = \frac{n_t \cos \theta_t}{n_i \cos \theta_i} |t|^2 \tag{1.13}$$

where the parameters r and t are the reflection and transmission coefficients of the wave as shown in Fig. 1.8. The value of the components parallel and perpendicular to the plane of incidence of these coefficients can be written in terms of the refractive index of each medium and the angles of incidence and transmission as given by the Fresnel equations shown in 1.14:

$$t_{\parallel} = \frac{2n_i \cos \theta_i}{n_t \cos \theta_i + n_i \cos \theta_t}; \qquad t_{\perp} = \frac{2n_i \cos \theta_i}{n_i \cos \theta_i + n_t \cos \theta_t}$$

$$r_{\parallel} = \frac{n_t \cos \theta_i - n_i \cos \theta_t}{n_t \cos \theta_i + n_i \cos \theta_t}; \qquad r_{\perp} = \frac{n_i \cos \theta_i - n_t \cos \theta_t}{n_1 \cos \theta_i + n_t \cos \theta_t} \tag{1.14}$$

For heterogeneous medium such as tissue, the average value of the refractive index can be used as a bulk property. However, tissues are comprised by multiple layers of possibly heterogeneous components, where multiple reflections and refractions may take place during photon propagation, in which cases the tissue can be modelled as a multi-layered structure [Wang et al., 1995].

While the absorption and scattering of tissue will be used to model the photon at each interaction site, the refractive index will be applied to Fresnel equations to model the reflection at the boundary between two media.

1.2 Photon Transport in Tissue

Different analytical and computational methods can be used to describe light travelling in tissue based on tissue's optical properties. The analytical radiative transfer theory and diffusion approximation, as well as the Monte Carlo computational method will be briefly explained in this section.

1.2.1 Radiative Transfer Equation

Photon transport in tissue has been described by using radiative transport theory (RT). RT states the conservation of the radiant energy $L(r, \hat{s})$, at position r and direction $\hat{s}$ as a the result of energy lost due to absorption and scatter, and energy gained due to the scattering into the propagation direction $\hat{s}$ (see Fig. 1.4) and a source of photons $S(r, \hat{s})$ [Patterson et al., 1991] as shown in Eq. 1.15.

$$\overbrace{\hat{s} \cdot \nabla L(r, \hat{s})}^{\text{Change due to energy flow}} = \underbrace{\mu_s \int_{4\pi} p(\hat{s}' \cdot \hat{s})\, L(r, \hat{s}') d\hat{\Omega}'}_{\text{Energy scattered into } d\Omega \text{ about } \hat{s}} \overbrace{- \mu_t(r) L(r, \hat{s})}^{\text{Loss due to scattering and absorption}} + \underbrace{S(r, \hat{s})}_{\text{Source of photons}} \qquad (1.15)$$

where $\mu_t = \mu_a + \mu_s$ is defined as the attenuation coefficient, and $d\hat{\Omega}'$ is the differential solid angle in the direction $\hat{s}'$. The RT equation, as shown in 1.15, disregards polarization, interference, and fluorescence, and assumes a time independent state.

1.2.2 Diffusion approximation

Solving the RT can be complicated given the degrees of freedom (three variables for the position r, and two for azimuthal and polar direction $\hat{s}$ - time independance being assumed-) [Wang and Wu, 2007], thus it is commonly approximated to a particular analytical solution. For the diffusion approximation tissue is modelled as a homogeneous medium and the distance between light sources and boundaries is considered to be large. Here, the main assumption is that tissue is an isotropic medium in which scattering dominates absorption.

The RT equation can be written in terms of spherical harmonics from which only specific terms of the expansion can be considered to approximate the light

behaviour into tissue [Patterson et al., 1991]. Particularly, the use of the first linear terms yields to the isotropic approximation. From this approximation, the diffusion equation for a steady state can be written as:

$$D\nabla^2\phi(r) = \mu_a\phi(r) - S(r) \tag{1.16}$$

where

- $D = [3(\mu_a + \mu'_s)]^{-1}$, is the diffusion coefficient.

- $\phi(r) = \int\limits_{4\pi} L(r, \hat{s})d\hat{\Omega}$, is the scattered fluence rate.

- $S(r)$, represents a source of photons.

Where μ'_s is the aforementioned reduced scattering coefficient . The reciprocal of μ'_s is the transport mean free path, and represents the depth over which a collimated beam becomes isotropic. Equation 1.16 is then a simplified expression from the RT that does not depend on the direction $\hat{s}$, and depends on a combined parameter μ'_s.

In the diffusion theory the effective attenuation coefficient μ_{eff} is also defined, and is given by:

$$\mu_{eff} = \sqrt{3\mu_a(\mu_a) + \mu_s} \tag{1.17}$$

and its inverse $\delta = \frac{1}{\mu_{eff}}$ is called the penetration depth and is equivalent to the distance at which light has decay by $1/e$ of the initial intensity.

1.2.3 Monte Carlo simulations

The Monte Carlo (MC) method has been widely used to simulate the propagation of individual packets of energy in tissue. MC refers to a type of computational methods that make use of random sampling of the parameters involved in a problem in order to converge to a solution. MC methods are based on repeated runs of the random sampling, and the statistical error decreases with this N number of repetitions by $1/\sqrt[2]{N}$. For the simulation of light transport in tissue, each photon packet moves in steps in accordance with the probability of photon-tissue interaction (Fig. 1.9), and the phase function that describes the scattering. The photon continues its propagation until it is detected in a specified region of the tissue, or it is completely absorbed by the tissue structure.
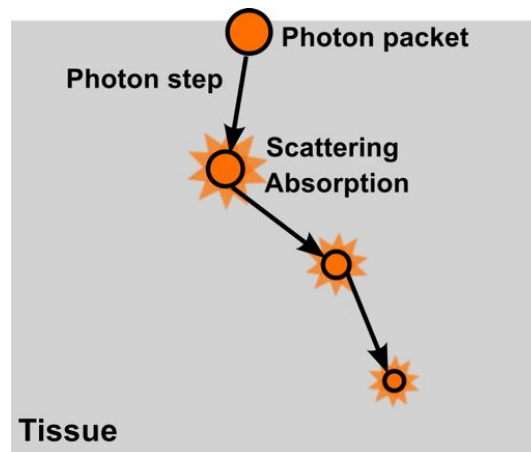
Figure 1.9: Photon packet propagation is simulated by undertaken "steps", at which it experiences absorption and scattering.

With the help of MC simulations it is possible to record the transmission and reflection from the tissue. Advantages of Monte Carlo simulation are that the geometry of the medium can be easily simulated without restrictions, and it is possible to add multiple layers of tissue with different properties as well as multiple sources.

The present work will often make use of Monte Carlo simulations to give an insight of the photons' behaviour and penetration reached withinin tissue for the probes being developed. A MC algorithm was implemented for this purpose, and will be explained in more detail in section 1.4.

1.3 Detecting light-tissue interactions

In an ideal scenario where only absorption takes place in a sample, the absorbance or optical density A can be obtained from the transmitted light using Beer's Law (Eq. 1.2) by:

$$A = -\log_{10}\frac{I_0}{I} = \epsilon c L \tag{1.18}$$

In this case for example, the absorbance obtained from a simple transmission test can be used to estimate the concentration c of the interrogated chromophore from a known traveled distance L. From Eq. 1.3 if the interrogated sample is an aggregation of various specimens presenting only absorption, a single linear analysis suffices to

obtain the specimen constituents (in this case the chromophores). In tissue samples however, this situation does not hold and the scattering properties from cells need to be taken into account even if the interrogated specimen (i.e. haemoglobin) does not scatter light. The former situation applies in the case of haemoglobin content in blood. Haemoglobin is the principal chromophore in the body, and is assumed not to be a scatterer on its own. If the haemoglobin concentration is to be known in-vivo with an optical technique, the scattering induced by the cells constituents would increase the optical pathlength due to the multiple scattering events, and would also introduce losses due to light being scattered and falling into directions other than the detector. Therefore, when applying optical methodologies in clinical settings, the technique is mostly concerned with the analysis of the absorption and scattering properties of the tissues.

Spectroscopic techniques, particularly can potentially retrieve information of different components of tissue given their individual set of optical properties, which vary along the electromagnetic spectrum as seen in Figs. 1.2 and 1.6. Among various spectroscopic techniques available for clinical settings, reflectance spectroscopy has been widely used due to its simple basis and its proved performance for certain applications in which the tissues of interest are close to the light source and detector. In cases where is necessary to interrogate tissues at larger distances, photoacoustic-based probes, can offer good resolution at higher depths.

1.3.1   Reflectance Spectroscopy

Reflectance spectroscopy is a technique that infers an object's properties from its spectral signature, which is described mainly by the scattering and absorption of light, as emanated from a known luminous source throughout the tissue. Various methods can be used to infer tissue's optical properties (i.e. μ_a, μ'_s) from reflected light, these include methods in time domain, frequency domain, and steady state [Utzinger and Richards-Kortum, 2003].

In the time domain analysis an ultrashort (picoseconds) pulse of light is delivered to the tissue and the intensity corresponding to the time spread function is detected (Fig.1.10 A). The mean time distribution of the impulse response signal t is then normally used to deduce the absorption coefficient and the reduced scattering coefficient. A multiwavelength approach can be performed in the time domain. This approach needs a system capable of fast tuning and detection, but can as well make use of multiple sources to avoid changes (over time) in the tissue under inspection

[Delpy and Cope, 1997].

Alternatively in the frequency domain analysis, a radio-frequency modulated light source is used. Light from this source is characterised mainly by an AC, and a DC component. Detection often involves a cross correlation step to down-convert the reflected signal in order to be processed using a Fourier transform [Tuchin, 2002]. The phase and intensity of the detected signal is then compared to the phase and modulation of the source (Fig.1.10 B).
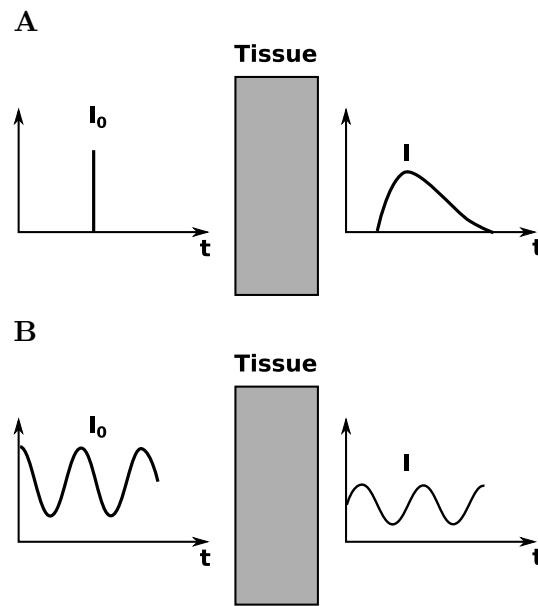
Figure 1.10: **A** Time domain. **B** Frequency domain.

Time and frequency domain are related by the fact that the output signal from a frequency modulated input can be obtained from the convolution of this input signal with the temporal point spread function of the system. These two tehcniques are usually used to obtain what is known as the differential pathlength factor (DPF). As previously mentioned, Eq. 1.18 can not be used in scattering media so it has to be modified as follows [Delpy et al., 1988].

$$A = \epsilon c L \, DPF + G \tag{1.19}$$

where G is a factor dependant on the geometry, and DPF is a pathlength scaling factor dependant on the absorption and scattering of tissue. The combined factor $d = L \, DPF$ accounts to the total pathlength of the light after multiple scattering

in the tissue, and can be obtained by $d = \frac{c\tau}{n}$, where c is the light speed in vacuum, τ is the transit time of light within the tissue, and n is the refractive index of the medium.

In the steady state spatially resolved approach light is continuously irradiated into tissue, and the distance between the light source and the detection of the re-mitted light will dictate the depth reached within the tissue for specific optical properties (see Fig. 1.11). As mentioned before, equation 1.2 cannot be used due to tissue scattering, therefore analytical expressions derived from the diffusion approx-imation are commonly used in conjunction with inverse Monte Carlo algorithms [4] to infer absorption and scattering from the tissue using this technique.

The steady state technique offers the great advantage of relatively easy to adjust equipment: a time-independent light source for excitation of the tissue, and a CCD array or photodiodes for detection [Palumbo and Prates, 2004]. Henceforth in this thesis, the reflectance analysis will refer only to the steady state method.
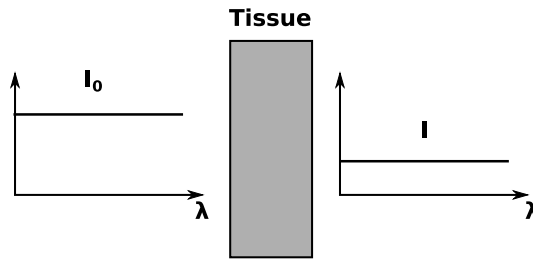
Figure 1.11: Steady state (continuous wave).

.

The basic probes for reflectance spectroscopy comprise one optical fibre for light delivery and one fibre for its collection after being scattered within the tissue; these fibres are usually positioned in the same plane, and separated by a distance d (Fig. 1.12). The detected light is then transmitted to a spectrometer. It is possible to use the same fibre for light delivery and detection, which has the advantages of small size, simplicity, and the availability to create small illumination points. However, the high backscattered light (coming back to the direction of emission) from the source coupled to the detector is difficult to avoid, a problem that can be mitigated by using multi fibre systems [Utzinger and Richards-Kortum, 2003]. Multiple detection sites at different distances to the light source can yield more information about the

---

[4]In inverse Monte Carlo methods a MC simulation is repeated iteratively until convergence to a set of optical properties.

tissue characteristics at various depths. The interdependence of reached depths and fibre geometries in reflectance spectroscopy have been further exploited to separate the optical characteristics of different tissue layers [Arifler et al., 2005].
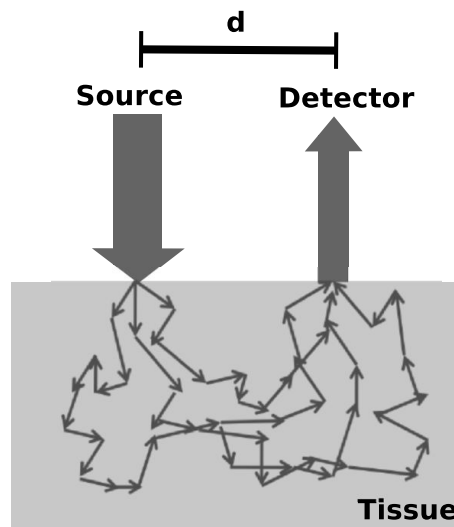
Figure 1.12: Detection of the scattered photons by tissue.

Many probes have been developed to evaluate anomalous tissue in feasible tumour masses. The evaluation of malignant masses is approached by two characteristics in cancerous tissue: 1) cancer cells distort tissue structures such as its nucleus which may produce a change in the scattering properties [Arifler et al., 2006]; 2) the oxygenation changes that a tumour experience throughout its different stages [Brown et al., 2009].

Other studies have applied reflectance spectroscopy probes for oxygenation measurements in tissue. For instance, to evaluate anastomosis [5] leaks [Gareau et al., 2010], and to describe haemodynamics parameters involved in neuro-functional process [Sharma et al., 2011]. Pulmonary artery catheters as well as central venous catheters have also been used to acquire oxygen saturation measurements by means of optical fibres [Kapany and Silbertrust, 1964; Waller et al., 1982; Baele et al., 1982].

Fibre optic probes have also been used when the probe needs to be fitted into other medical instruments while doing a procedure. For example, Wang et al [Wang et al., 2009] coupled a 1.63 mm outer diameter probe into a colonoscope to differen-

---

[5]The term anastomosis refers to the surgical procedure during which two structures, usually two sections of the intestine, are connected.

tiate haemoglobin concentration changes during carcinogenesis, while Gareau et al [Gareau et al., 2010] inserted a 8 mm diameter probe into a trocar to monitor tissue oxygenation to detect anastomotic complications during esophagectomies.

1.3.2   Photoacoustic Imaging

As mentioned previously, the energy that is not re-radiated as light, can be transformed into thermal energy. The photoacoustic effect is based on the formation of pressure waves following thermoelastic expansion due to heat [Wang and Wu, 2007]. After light is absorbed and converted to heat, tissue undergoes a thermal expansion that leads to a sudden pressure rise resulting in the transmission of an ultrasound pulse.

Photoacoustic methods offer superior spatial localisation than reflectance spectroscopy because it detects the light absorption via ultrasound detection. This feature gives good optical contrast to chromophores in combination with the good ultrasound spatial resolution.

A pulsed laser source is usually used in photoacoustic techniques, and the duration of the pulse can yield to stress and thermal confinement. Thermal confinement occurs when the laser pulse is shorter than the thermal relaxation time, and the heat conduction is not significant. Stress confinement, on the other hand occurs when the laser pulse is shorter than the stress relaxation time, in which case stress propagation is not significant.

Under stress and thermal confinement, the initial pressure rise p_0, can be described in terms of the optical fluence ϕ, the absorption coefficient μ_a, the fraction of light being converted to heat η_{th}, and the Grüneisen parameter $\Gamma = \frac{\beta v_s^2}{C_p}$ as shown in Eq. 1.20; where β is the thermal coefficient of volume expansion, v_s is the speed of the sound, and C_p is the specific heat capacity at constant pressure. The Grüneisen parameter reflects the fraction of thermal energy being converted to pressure.

$$p_0 = \Gamma \eta_{th} \mu_a \phi \tag{1.20}$$

The temporal response can be then detected with an ultrasound transducer, and represents the initial pressure distribution [Laufer et al., 2005]. This signal can be then processed to characterize tissue, or be spatially resolved to reconstruct an image of the absorption in tissue.

Advantages of using photoacoustics in tissue imaging include high contrast, good imaging depth, high resolution and lack of speckle artefacts [Wang and Wu, 2007]. High contrast is provided by the optical absorption by tissue chromophores. Light penetrating tissue deeper than 1 mm becomes isotropic and starts decaying exponentially making it difficult to detect with optical methods since fewer light can reach the detection fibre. In these cases however, the acoustic signal can be still detected given the lower ultrasonic scattering coefficient (2-3 fold lower than the optical scattering coefficient) providing higher spatial resolution [Wang, 2009]. A possible limitation of the photoacoustic technique is that, at depths larger than the penetration depth δ absorption signals became weak making the ultrasound detection more difficult, yet improved technology has been able to interrogate depths in the order of centimetres [Beard, 2011]. On the other hand, high spatial resolution is achieved by the high frequency of the generated acoustic signal, thus the factors limiting spatial resolution are the acoustic attenuation in tissue and the detector geometry and bandwidth [Beard, 2011]. Finally, the lack of speckle artefacts in photoacoustic images is due to the constructive interference at the boundaries of the tissue. This constructive interference is possible given the always positive initial pressure rise [Guo et al., 2009].

Examples of current research using photoacoustic techniques include the identification of lipid plaques in arteries, which exploit lipid absorption peaks (most commonly the one at 1210 nm); here, measurements have reached up to 2.5 mm into tissue when carried out from within the artery [Wang et al., 2010, 2012], and about 3 mm when performed non invasively [Allen et al., 2012]. Other uses of photoacoustic techniques include the monitoring of tumour evolution through the interrogation of vascularity changes during cancer development [Manohar et al., 2007].

In terms of blood detection, photoacoustics has been used for the measurement of oxygenation in whole blood [Laufer et al., 2004, 2007; Friedrich et al., 2011]. Despite the difficulties found in these works with respect to absolute quantification of oxygen saturation, promising results of relative differentiation point out to further research focused on data analysis.

In this thesis, photoacoustic imaging will be used to explore the penetration advantages offered by the technique. It will be investigated the distances from the medical probe at which a blood vessel could be detected, as well as the wavelength dependence of the signal.

1.4   Monte Carlo method

A Monte Carlo algorithm was implemented for the simulation of reflectance spectra of tissue with emphasis in whole blood. The implementation has been coded in a combination of C modules (in .mex files) and Matlab scripts (Matlab v7.11.0), that follows the algorithm developed by Prahl et. al. [Prahl et al., 1989], for a homogeneous medium. The path of each photon packet is simulated one by one; the flowchart of this implementation is shown in Fig. 1.13.

In Chapter 2 and 3 one homogenous medium will be modelled in a MC simulation. In this case the hypothesis is that the tip of optical fibre is immersed in the tissue, parallel to the walls containing the tissues of interest, and that the distance from the fibre to the walls is large and will not interfere with the path of the collected photon. For these simulations one of the objectives will be to estimate the penetration of light into a specific tissue.

On the other hand, in Chapter 4 two homogeneous media will be modelled. This approach will seek to understand the effect of the absorption and scattering at the first medium into the light absorbed in the second medium. Here, the tissue structure (composed by the second medium) will be assumed to be immersed into a different tissue. The structure is also supposed to be large enough to be "seen" by the fibre as a semi-infinite medium.

The code saves information about the final position of the detected photons, their weight, maximum depth reached within the medium, pathlength, and number of undergone interactions. Additionally, it saves a tissue array with the information of the photons absorbed in the medium.

1.4.1   Monte Carlo algorithm

Each photon packet in the Monte Carlo (MC) code is defined by its status, step size (distance traveled between interactions), total pathlength, weight, and maximum depth reached during the propagation. The status is binary, that is set to one while the photon is alive and propagating, and to 0 when the photon is terminated. The simulation of each photon runs until the status equals 0. The initialization of the photon is set with the following values, where RND is a random number generated by the function ranmar [Roe]:
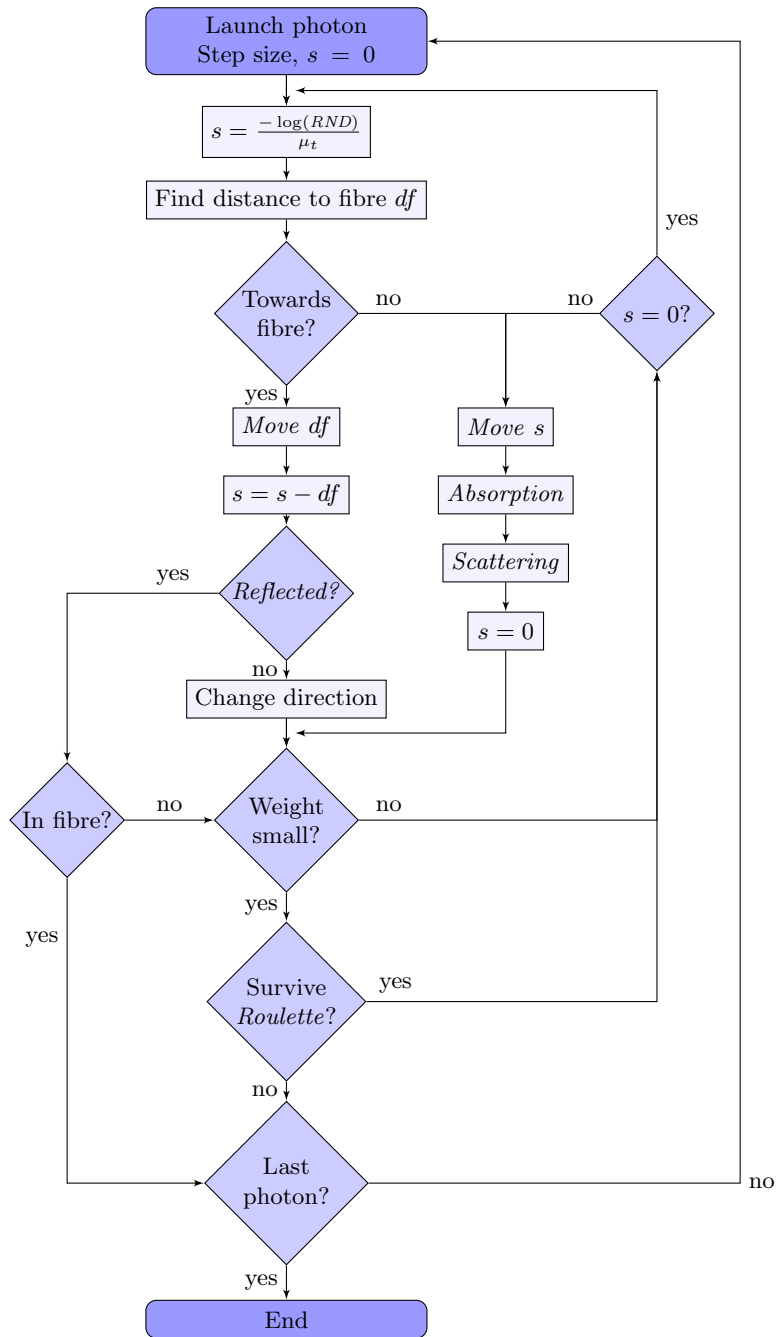
Figure 1.13: Flowchart of the Monte Carlo algorithm. The algorithm is called in Matlab while the main code is written in C.

- status = 1

- step size: $s = \frac{-\log(RND)}{\mu_t}$ (mm)

- pathlength = 0 (mm)

- weight, $w = 1$

- maximum depth = 0 (mm)

A Cartesian coordinate system XYZ is used to track the movement of the photons in the simulation. The origin of this system is set at the point of the photons detection as shown in Fig. 1.14. The final position of the detected photons, and of the lost weight are saved in cylindrical coordinates (r,z).
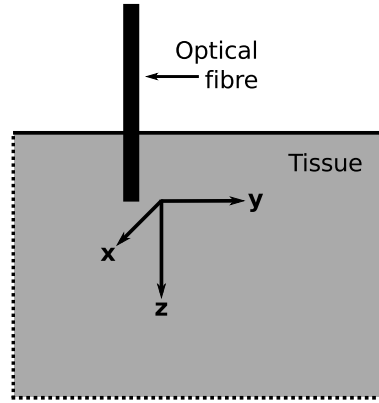
Figure 1.14: Cartesian coordinate of use for the movement of photons within the simulated medium. The origin of the coordinates is positioned at the centre of the fibre used for detection.

Photons are launched from a circular fibre of radius r_1 immersed in the tissue at Z=0; the distance to the detection area is defined. The initial position of the photon is sampled from a uniformly distributed position at the surface of the light source with a random direction delimited by the numerical aperture of the simulated fibre (NA_{core}), and the refractive index of the tissue (n_{tissue}):

$$r_0 = r_1 * \sqrt{RND}$$

$$\phi_0 = 2 * \pi * RND$$

$$\theta_0 = \arccos(1 - RND * (1 - \cos(\theta_{max}))) \tag{1.21}$$

where $\theta_{max} = \frac{NA_{core}}{n_{tissue}}$

Photon movement

Previous to movement, and if the photon is propagating towards the fibre, the distance df from its current position to the plane at the fibre surface is calculated. The photon then is moved by $d = df$ if the distance to the fibre is smaller than the step size of the photon. Otherwise the photon is moved the complete step ($d = s$) followed by absorption and scattering.

Additionally, the function to move the photon increases the pathlength of the photon by d, and the number of iterations. It also updates its radial position and its maximum reached depth.

If the photon is moved to $Z = 0$, the current and previous radial position are evaluated to decide whether the photon reached the detection surface, and if so, whether it fell within the acceptance cone of the fibre. If the photon packet does not meet these conditions, i.e. it is not in the fibre, the step size is decreased by df and continues its propagation.

If the photon reaches the fibre surface, it is randomly either reflected to the tissue or transmitted to the fibre and terminated. Assuming $n_{tissue} < n_{fibre}$, the photon is reflected if $RND \leq R_i$, where R_i is the internal reflectance for a non polarized medium ($R_i = \frac{1}{2}[|r_\parallel|^2 + |r_\perp|^2]$). By using equations 1.14, and 1.12, R_i can be determined by:

$$R_i = \left[\frac{\sin^2(\theta_i - \theta_t)}{\sin^2(\theta_i + \theta_t)} + \frac{\tan^2(\theta_i - \theta_t)}{\tan^2(\theta_i + \theta_t)} \right] \tag{1.22}$$

where n_{tissue} and n_{fibre} are the refractive indices of the tissue and of the detection fibre respectively ($n_{tissue} \approx 1.33$; $n_{fibre} \approx 1.4 - 1.5$), θ_i is the angle of incidence from the tissue, and θ_t is the angle of transmission into the fibre (from Snell law). If the photon is reflected its direction in the z-axis is changed, while if it is transmitted its final weight and position are saved.

Absorption

The absorption suffered by the photon is given by the scattering and absorption coefficient of the medium. When a photon undergoes absorption, its weight is decreased by $dw = \frac{\mu_a}{\mu_t} w$. This function also increases the (r,z) element of the tissue

array by the lost weight, dw.

Scattering

As mentioned in section 1.1.2, the HG phase function has shown to be more appropriate for the modelling of the scattering of whole blood. Consequently the HG function 1.10 will be used throughout the present work.

The HG phase function was used for randomly sampling the value of the cosine of the polar angle, μ,:

$$\int_{-1}^{\mu} p(\mu)d(\mu) = RND \qquad (1.23)$$

Leading to $\mu = 2RND - 1$, for $g = 0$; while for $g \neq 0$:

$$\mu = \frac{1}{2g}\left[1 + g^2 - \left(\frac{1 - g^2}{1 - g + 2gRND}\right)^2\right] \qquad (1.24)$$

On the other hand, azimuthal symmetry was assumed, so that the azimuthal angle is chosen randomly by $\psi = 2\pi RND$, and the new direction of the photon is calculated as in Cashwell and Everett [Cashwell and Everett, 1957].

Photon termination

Photons are terminated when its status change to 0. This can happen if the photon reaches the detection fibre, or if it is finished by a roulette function, which allows to terminate the photon packet in a non-arbitrary manner. The photon goes to the roulette when its weight falls to a value $w \leq 0.0001$. The roulette function generates a random number and terminates the photon when $RND \geq 0.1$; if the photon remains alive its weight is updated to $0.1w$.

1.4.2   Implementation check

Since the code was custom-made a validation step that compared its simulation results with a theoretical model was made. The MC results of this first set of analysis were compared against diffusion theory approximations developed by Farrell et. al. [Farrell et al., 1992]. Additionally, in order to have an easy way to visualise the

scattering and absorption of photons within a medium, the code was able to store an image of the scattering events that took place in it. This image was helpful to qualitatively check the behaviour of the code with different parameters. The parameters use for validation will be chosen to facilitate comparison, first with the diffusion theory and then with the expected shapes of absorption within the tissue. The analysis of the specific fibre geometries, and optical properties of the tissues of interest for this thesis will be later presented when discussing the individual probes.

Comparison with diffusion model

Farrell developed a diffusion model of the reflectance for matched and mismatched boundaries, and two different methods: a single scatter source, and an extended scatter source. Here, reflectance obtained by the MC was compared to the reflectance obtained with Farrell's model from a single scatter source in the case of matched boundaries, denoted by:

$$R = \frac{1}{4\pi} \frac{\mu_s'}{\mu_a + \mu_s'} \left[\frac{1}{\mu_t'} \left(\mu_{eff} + \frac{1}{r_1} \right) \frac{e^{-\mu_{eff} r_1}}{r_1^2} + \left(\frac{1}{\mu_t'} + 4D \right) \left(\mu_{eff} + \frac{1}{r_2} \right) \frac{e^{-\mu_{eff} r_2}}{r_2^2} \right] \tag{1.25}$$

where D is the diffusion coefficient and μ_{eff} the effective attenuation coefficient introduced in 1.16 and 1.17. The total interaction coefficient μ_t', as well as the parameters r_1 and r_2 for a photon source at $z = 0$, are defined by:

- $\mu_t' = \mu_a + \mu_s'$
- $r_1 = \sqrt{z^2 + r^2}$
- $r_2 = \sqrt{(z + 4D)^2 + r^2}$

A comparison with this diffusion model and the MC algorithm implemented here, was carried out in the same fashion as in Farrell's work: reflectance values were obtained with both methods for a light source at the centre of coordinates, and the reflected values were obtained at different distances from this point. The light source in the MC is modelled as pencil beam at (0,0,0) and direction parallel to the Z axis. Photons were detected by discrete areas of concentric rings in a distance from 0 to 15 mm (Fig. 1.15).
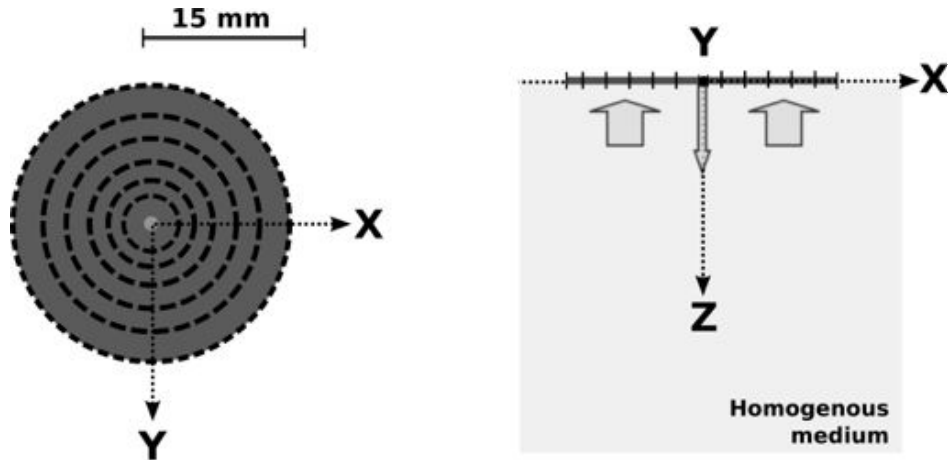
Figure 1.15: Geometry of the MC simulation. Light is emitted by a pencil beam centered in the XY plane and collected within a region of 15 mm radius.

The MC simulation was run for 1×10^5 photons. Reflectance results for an absorption coefficient of $0.1\,mm^{-1}$ and $0.01\,mm^{-1}$ are shown in Fig. 1.16. In both cases, the implemented MC and the Farrell model, the value of the scattering coefficient and the anisotropy were set to and $10\,mm^{-1}$ and 0.9 respectively. Figure 1.16 shows good agreement between the theoretical curves (smooth curves) and the curves from this MC implementation (noisy curves), except for shorter distances where the diffusion approximation doesn't hold.
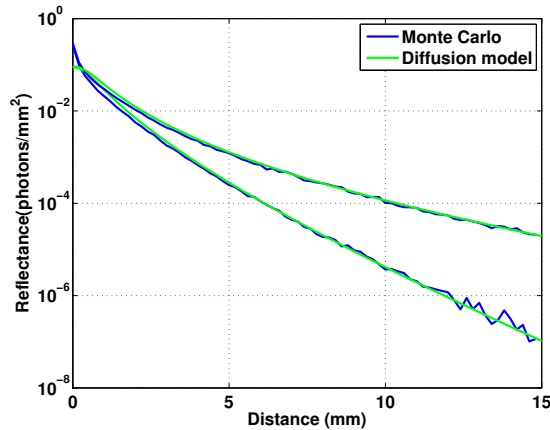
Figure 1.16: Reflectance curves for μ_a of $0.01\,mm^{-1}$ (upper curves) and $0.1\,mm^{-1}$ (lower curves). In each case, the smooth curve corresponds to the diffusion model by Farrell et. al. [Farrell et al., 1992] and the noisy curve corresponds to the MC algorithm implemented here.

Visualization

Radial position and depth information corresponding to absorption events were stored in a tissue array to visualise the effect of the optical properties. This would help to verify whether the code is performing as expected for different absorption and reduced scattering coefficients. With this objective four configurations shown in Table 1.2 were investigated using the geometry shown in Fig. 1.17. A pencil beam is sent to the medium at 2.5 mm from the origin, and light is detected within a radius of 75 μm from the centre of coordinates.

Table 1.2: Set of optical parameters used to obtain Fig. 1.18

	g	μ_s (mm^{-1})	μ'_s (mm^{-1})	μ_a (mm^{-1})
A	0.9	10	1	0.1
B	0.9	10	1	0.5
C	0.97	70	2.1	0.1
D	0.97	70	2.1	0.5
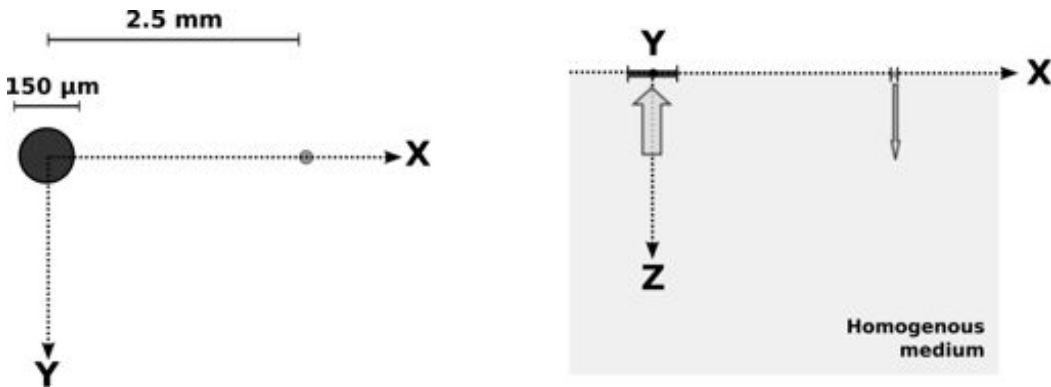
Figure 1.17: Geometry of the MC simulation. Light is emitted by a pencil beam at (2.5,0,0), and collected within a region of 75 μm radius.

This type of image helps to get a better understanding of the fraction of the absorption taking place in the tissue that is actually being sensed by the detector (optical fibre). Since the MC algorithm makes the photon package to undergo absorption at all scattering events, it also records the pathway undergone by the photons. Therefore, showing the map of absorbed events helps to get an idea of the penetration and expansion of the light in an specific tissue. With this in mind, a selection of images of the undertaken absorption will be presented for the specific

probes in this thesis.
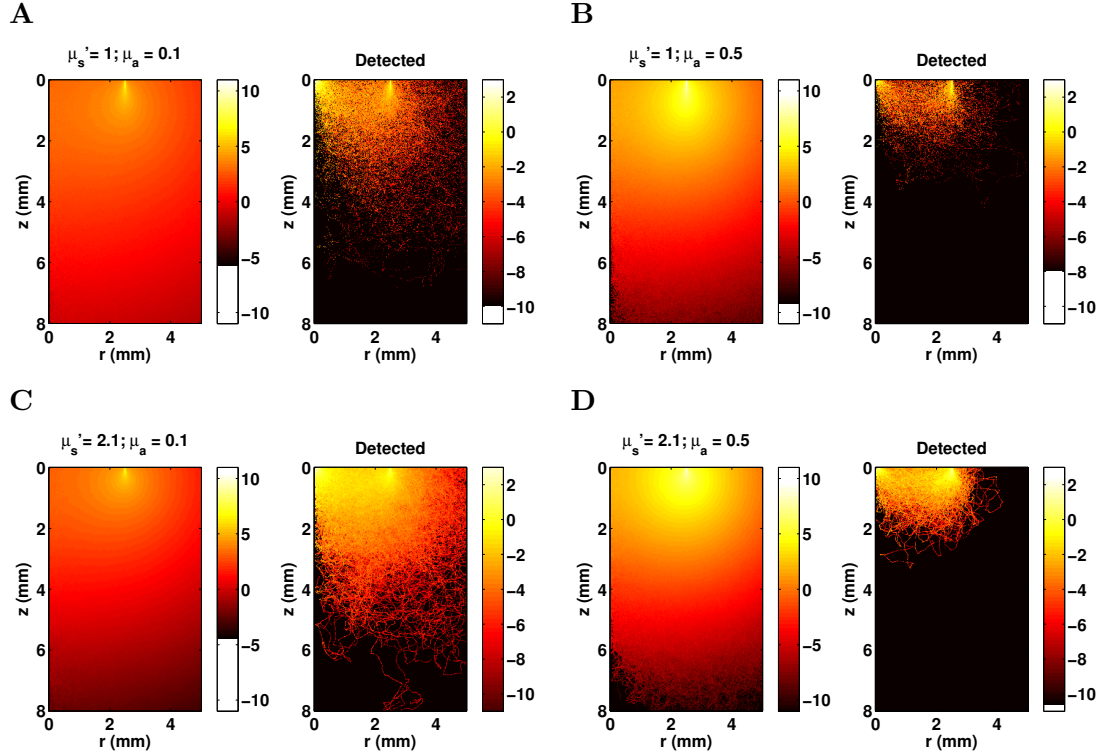
Figure 1.18: Tissue array for the case of a detector and source fibres separated by 2.5 mm, at z=0. The left heat map shows all the absorption that took place in the medium. Right hand heat maps show the undergone absorption by the detected photons. Four sets of properties are presented for comparison: **A** $\mu'_s = 1 \ mm^{-1}$ and $\mu_a = 0.1 \ mm^{-1}$; **B** $\mu'_s = 1 \ mm^{-1}$ and $\mu_a = 0.5 \ mm^{-1}$; **C** $\mu'_s = 2.1 \ mm^{-1}$ and $\mu_a = 0.1 \ mm^{-1}$; **D** $\mu'_s = 2.1 \ mm^{-1}$ and $\mu_a = 0.5 \ mm^{-1}$

Configuration B and D display high absorption, while C and D display high scattering. The resulting images from the logarithm of the normalised weight (with respect to the total number of launched photons) stored at a specific position for runs of 500000 photons, are shown in Fig. 1.18. It can be noticed that for higher absorption the detected photons reached shallower depths than those for lower absorption coefficient. In the case of higher scattering, more photons are absorbed given the increase of scattering events undergone by the photons as it was expected.

The MC algorithm described here can be adjusted for different source -detector geometries. All the results shown in this thesis are done with the source and detector located at Z=0, but this can be modified by changing hard-coded values in the C code. An improvement to this implementation would allow to pass the geometrical

parameters to the C code in order to make it more flexible.

Chapter 2

Venous-Arterial blood differentiation with a Double Clad Fibre

The differentiation between arterial and venous blood [1] is an important task in medical procedures. For instance, during a transseptal puncture the right atrium of the heart is accessed by crossing the inter-atrial septum from the left atrium (see Fig. 2.1). This technique is used during the treatment of atrial fibrillation, atrial septal defects, and mitral valves problems, among others [Babaliaros et al., 2008].

The basic equipment required for this procedure comprises a plastic sheath (63 cm standard), a dilator (67 cm standard), and a needle (71 cm standard)[Earley, 2009]. Using a guidewire, the sheath and dilator are advanced through a femoral vein to the superior vena cava (SVC). Once there, the guidewire is replaced by the transseptal needle. From the SVC the whole assembly is placed into the right atrium, and then the fossa ovalis of the interatrial septum is located. With the assembly against the fossa ovalis, the needle punctures the septum to gain access to the left atrium. The correct placement of the needle is commonly verified with a pressure sensor.

---

[1]All mention to arterial and venous blood in this thesis make reference to blood in the systemic circulation, i.e. veins carry deoxygenated blood while arteries carry oxygenated blood.
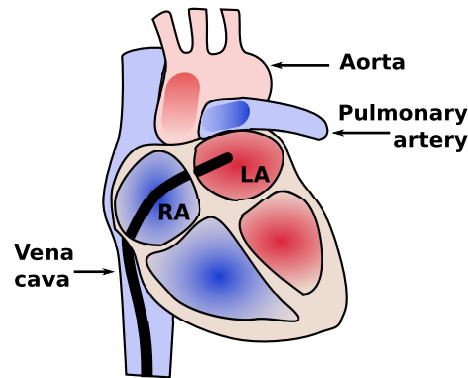
Figure 2.1: Illustration of the transseptal needle cross from the right atrium to the left atrium of the heart.

Moreover, an undetected arterial puncture can lead to life threatening complications during procedures such as central venous catheterisation (CVC) during which a catheter is inserted through the jugular, subclavian or femoral vein to obtain access to the venous circulation. In a typical CVC procedure a needle (finder) is first inserted and a follow-up blood aspiration verifies that an artery was not punctured (see Fig. 2.2). After this verification, the needle is substituted by a dilator and a catheter can be inserted through a guidewire.
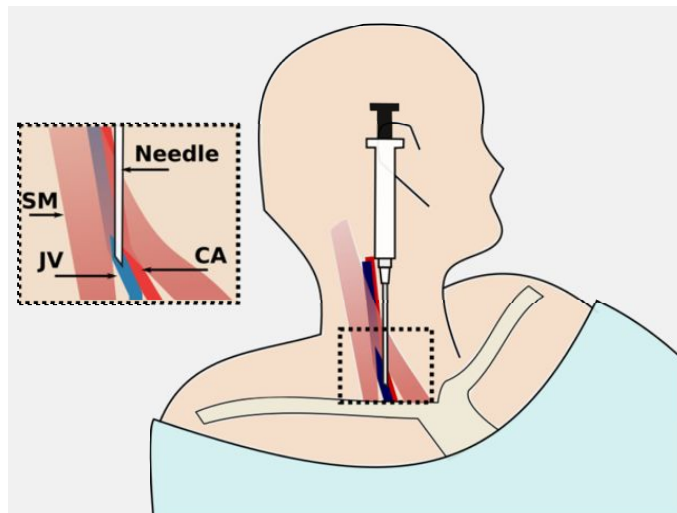
Figure 2.2: Internal jugular approach [UC Irvine School of Medicine] of a central vein catheterisation. The intervention site has been enlarged in the box. JV: jugular vein; CA: carotid artery; SM: sternocleidomastoid muscle.

The rate of artery injury occurrence has been shown to be 5.9% [Reuber et al., 2002] during internal jugular venous cannulation. If an arterial puncture is detected,

the needle is withdrawn and pressure is applied for several minutes to prevent bleeding. However, if the arterial puncture goes unnoticed there is a risk of the placement of a larger cannula into the artery where major complications such as haematoma, haemothorax, pseudoaneurysm, fistula or stroke, may occur [Guilbert et al., 2008; Shah et al., 2004]. Ultrasound has been used to assess the vein location and distinguish it from arteries. However, this tool is not always used and in some cases can fail to provide clear identification because of the collapse of a vein due to pressure from the US probe [Reuber et al., 2002; Guilbert et al., 2008].

2.1 Oxygen Saturation measurements

Alongside with haemodynamic differences between veins and arteries that can be probed with Doppler ultrasound, a key feature that distinguishes them is their oxygen saturation. The oxygen saturation is a measure of the oxygen being carried by haemoglobin in blood, and can be defined as the ratio of the concentration of haemoglobin in its oxygenated state to that of the total haemoglobin content as shown in Eq.2.1, where c_{HbO_2} is the oxy-haemoglobin concentration in blood and c_{Hb} is the deoxy-haemoglobin concentration in blood.

$$SO_2 = \frac{c_{HbO_2}}{c_{HbO_2} + c_{Hb}} \tag{2.1}$$

Normal values for venous oxygen saturation range from 60% to 80% while arterial oxygen saturation can reach values over 95%. Variation of these values may occur in case of disease. Venous oxygen saturation (SvO_2) is a measure of the rate between oxygen delivery and consumption, and factors such as anaesthesia, abnormal thermal conditions or admixture of arterial blood, among others, could impair this balance. On the other hand, low arterial oxygen saturation (SaO_2) may be a consequence of oxygen supply or ventilation deficiency.

Estimation of SO_2 can potentially provide valuable information in order to verify the placement of the device into the desired vessel. Optical fibres can be used for this purpose by providing information about oxygenation without adding much complexity to the clinical setup.

A commonly well known tool for patient monitoring that works based on light absorption is pulse oximetry. The basic principle of a pulse oximeter is the analysis of transmitted light through tissue generally at 660 nm and 940 nm. From Fig. 1.3

we can see that, at these wavelengths absorption due to oxy and deoxy-haemoglobin show notable differences, both at the range of lowest Hb absorption. Non-pulsating absorbance in this instrument is disregarded as coming from average tissue, and venous blood. Then the ratio of pulsatile absorbance at these wavelengths leads to the measure of arterial oxygen saturation by empirically calibrating the instrument with data from healthy individuals [Schnapp and Cohen, 1990].

The use of optical methods to measure oxygen saturation dates back to the 1940's when Millikan started using transmittance techniques to estimate SO_2 from optical measurements [Millikan, 1942]. Later on, Polanyi introduced the idea of using light reflected from optical fibres [Polanyi and Hehir, 1960]. Many instruments have been developed thereafter with the principle of obtaining tissue oxygenation from their absorbance at two different wavelengths.

In this manner, [Polanyi and Hehir, 1962] set the grounds of oximetry measurements [Takatani and Ling, 1994] showing the validity of the empirical expression for oxygen saturation from reflectance measurements at two wavelengths ($S(\lambda_1)$ and $S(\lambda_2)$):

$$SO_2 = a + b\frac{S(\lambda_2)}{S(\lambda_1)} \tag{2.2}$$

where a and b depend on the geometry of the probe and the parameters of the blood sample. This expression provides a simple linear relation for oxygen saturation and the reflectance spectrum where the use of two wavelengths reduces the influence of haematocrit variation.

As mentioned, pulse oximetry is a non invasive method which relies in light transmission, but there is also the need of oxygenation monitoring during invasive procedures. For this reason, current commercial oximeters can also be commonly found in catheters which rely on reflectance measurements for SO_2 estimations [Lifesciences, 2011]. When compared to the gold standard (gas analysis) of commercial oximeters, fibre optic sensors within catheters show comparable accuracy in oxygen saturation monitoring [Waller et al., 1982; Baele et al., 1982; Trubiano et al., 1996]. These oximeters commonly work at two wavelengths: 660 nm and 810 nm, although three wavelength oximeter catheter can be found with an extra-wavelength at 740 nm to further reduce haematocrit effects [Bongard et al., 1995].

There is also ongoing research focus on fitting these optical probes into different invasive devices, for instance to monitor patients and to evaluate tissue abnormal-

ities. As an example, studies by Brown et al. and Wang et al.[Brown et al., 2009; Wang et al., 2009] use reflectance spectroscopy to measure tumour oxygenation for cancer state diagnosis. In the work of Brown et al., a biopsy needle-based probe is inserted in the patient to interrogate oxygenation variation between benign and malignant cancer. They used two probes able to be embedded in cannulas for breast biopsies with outer diameter of 3.4 and 2.1 mm. The probes consisted in a set of source-fibres surrounded by another set of detector-fibres. The sensing depth of their probe range from 0.6 to 2 mm in breast tissue for a 400-600 nm illumination. The fibre arrangement had been previously used to obtained the absorption and scattering coefficient with an error up to 8.42 ± 11.3 percentage in tissue phantoms [Bender et al., 2009].

Wang et. al. on the other hand used a flat arrangement of detection fibres packed in a probe of 1.6 mm which could be fitted in an colonoscope channel [2], and reach a sensing depth of 0.6 to 1.2 mm in the wavelength range of 600-800 nm. With this arrangement of fibres they fitted a model of the oxygen dissociation in haemoglobin finding an error in the measure SO_2 of less than 5% for pressures greater than 15 mmHg and oxygen saturation of 29%.

These examples illustrate how optical fibres can play an important role when decreasing the probe size is crucial, such in the case of minimally invasive procedures. However, there is still the need of smaller probes that can be fitted into lower diameter devices.

2.2   Double clad fibre

As mentioned above, fibre optics threaded through catheters and needles has proven to be a valuable technique that can directly and immediately measure localised tissue properties such as blood oxygenation in real-time. Applications of such a device include patient monitoring in critical care and tissue assessment for potential diagnosis of a multitude of conditions, including evaluation of tumour masses and vessel identification.

Here a double clad fibre (DCF) device is proposed for detecting oxygen saturation using reflectance spectroscopy. This fibre is composed of a monomodal core, an inner multimodal cladding. It has been used for the pumping system of some lasers by

---

[2]Colonoscope working channels range from 3.2-3.8 mm, although smaller diameters can be found in pediatric devices [Fujifilm; Barth et al., 2012]

sending the signal and pump light through the core and inner cladding respectively. The special geometry of the DCF provides opportunity to design a low complexity probe with the allowance for further integration with other sensing methods (such as OCT, Doppler and photoacoustic spectroscopy) via the single mode core.

The performance of double clad fibres (DCF) has been tested for fluorescence spectroscopy [Wang et al., 2007; Ryu et al., 2008, 2009; Thomas et al., 2008; Chang et al., 2008] and optical coherence tomography measurements [Ryu et al., 2008, 2009]. Ryu et al. fabricated their own DCF with enhanced cladding coupling efficiency. In their work they performed OCT and fluorescence spectroscopy measurements simultaneously, sending both excitation signals through the core of the fibre. Light was collected back by the fibre's core for the OCT readings, and by the inner cladding for the excited fluorescence. Chang et al. used commercial fibres for their work in fluorescence spectroscopy, observing high sensitivity but significant back-reflection.

For the aforementioned applications, the sensitivity of the fibre over SO_2 variations will need to allow the differentiation of at least venous to arterial blood which for the mentioned normal values have a lowest difference of about 15% (from venous blood at 80% oxygenation to arterial blood at 95%). The use of a DCF is expected to achieve low light penetration due to the fibre dimensions, however this will not represent an issue as long as the detected photons carry enough information to differentiate the spectra from venous and arterial blood, since the verification of the device position would be in relation to its immediate surroundings.

In this work, a DCF system (Gooch & Housego) with diameters with diameters of 9 µm, 125 µm, and 245 µm core/cladding/outer-cladding (see box in Fig. 2.3) was purchased for a first experimental setting. To carry out reflectance spectroscopy, light was delivered to the tissue through the core of the fibre and the scattered light was detected by the inner cladding. Such a setup offered the advantages of simplifying instrument design, and giving more accurate spectral readings because of the expected low degree of back-reflected light.

A readily available broadband source (Superlum BLM-S-820) was used in these preliminary experiments to interrogate blood-like solutions. This light source, commonly used for OCT, works in the wavelength range of 780 to 880 nm. It was hypothesized that oxygenation changes would be easily detected using the whole reflected spectrum at these wavelengths given the change in absorption trend from HbO_2 and Hb in the surroundings of the isosbestic point at 800 nm where the absorption coefficient varies approx. $0.1mm^{-1}$. However, this hypothesis was falsified

when the spectra showed no significant differences for measurements taken from 70% to 90 % blood oxygenation[3]. At this point the MC algorithm that was being prepared simultaneously showed no significant spectral changes in the investigated range.
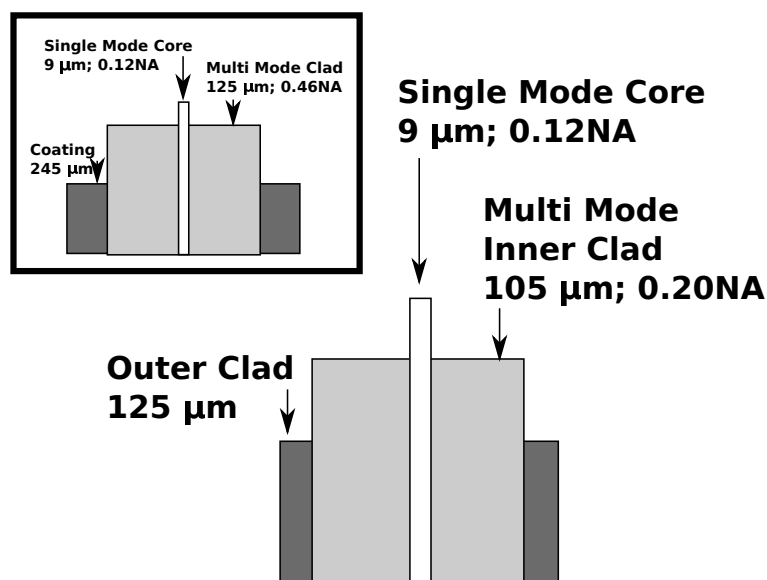
Figure 2.3: Double Clad Fibre geometry and numerical apertures of the core and inner cladding. The box shows another option for the fibre geometry that was discarded for its larger diameter

In a second stage of experimental design three factors were taken into account:

- Fibre diameter. In order to have an adaptable probe able to couple into diverse cannulas, a smaller fibre diameter was chosen [4]. The diameters of the new DCF are 9 µm, 105 µm and 125 µm for the core, inner-cladding, and outer-cladding respectively (Fig. 2.3).

- Oxygen depletion. In the first attempts to deoxygenated blood using sodium hydrosulfite, it was not possible to reduce blood oxygenation by amounts larger than 20% as measured with a commercial co-oximeter. Then, yeast was proposed to be used in this second stage.

- The need of an additional source that increase detection sensitivity.

The following section will explain the choice of the light source to acquire the

---

[3]The results from this preliminary experiments are shown in the Appendix A.

[4]For instance, guidewires use in coronary micro catheters can be smaller than 0.36 mm [Terumo]

reflectance spectra. The decision was taken based on computer simulations applying the Monte Carlo (MC) algorithm mentioned in the previous section. Penetration depth and estimated response of the fibre will be also simulated to show the feasibility of spectroscopic analysis with the DCF.

2.2.1 Monte Carlo analysis for the DCF geometry

The simulations were carried out with the custom MC software, where each photon packet was launched from an initial position sampled from a probability distribution derived from the geometry of the double clad fibre (diameters of 125, 105 and 9 microns for the outer cladding, inner cladding, and core respectively), and its numerical aperture (core, 0.12; clad, 0.20). Figure 2.4 shows the geometry of the simulation. The first part of the figure illustrates the surface of the fibre from the top of the tissue. Light is delivered from the core of the fibre, and detected by the cladding which forms a concentric ring.
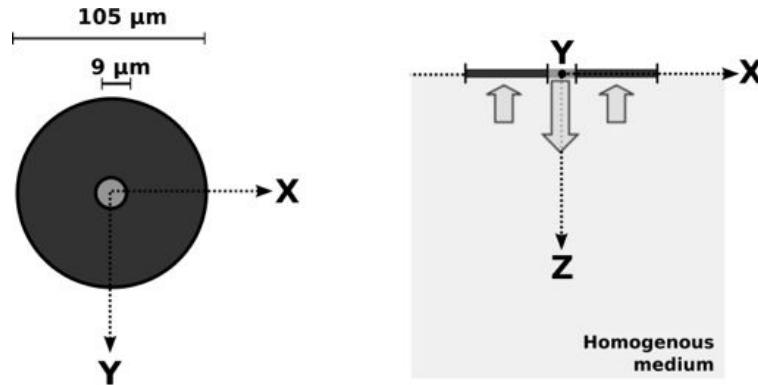
Figure 2.4: Geometry of the MC simulation. The DCF is centered in the XY plane. Light is emitted by the core and detected by the inner cladding.

Wavelength selection

As mentioned above preliminary experiments were performed to test the sensitivity of the fibre within the wavelengths from 790 to 860 nm (see Appendix A). These tests suggested that the measurements were not sensitive enough to differentiate spectra from blood oxygen saturation in that wavelength range for the small source-detector separation of the fibre. For this reason instead of processing the whole spectrum, one wavelength from the broadband light source was chosen to be compared with a second light source (Eq. 2.3) as previously seen from [Polanyi and Hehir, 1962].

In this manner, the isosbestic point at $\lambda_2 = 797$ nm was to be used in combination of a wavelength λ_1 at which oxy and deoxy-haemoglobin have significant absorption differences.

$$Response(SO_2) = \frac{S(\lambda_1)}{S(\lambda_2)} \tag{2.3}$$

Two commercially available sources at 635 and 675 nm respectively were considered. Large absorption differences between oxy and deoxy-haemoglobin are present in the range covered by these two wavelengths (see Fig. 2.5, and Fig. 1.3), while keeping a low value of the overall absorption coefficient (hence, allowing photons to undergo more interaction events).

Although the difference of absorption coefficient from deoxy and oxyhemoglobin for instance, is about 10 fold at 635 nm to that at 675 nm for a haemoglobin concentration of 150 g/L , the reflectance spectrum will also depend on the scattering properties of the tissue. For this reason a series of MC simulations were performed to evaluate the choice. Once the light source was chosen, the simulated response of the fibre to SO_2 changes was obtained as well as the penetration of the photons in whole blood.
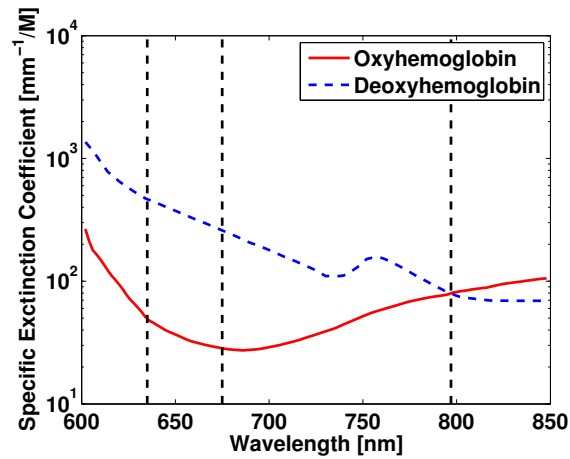
Figure 2.5: Specific extinction coefficient of haemoglobin. Vertical dotted lines correspond to the proposed wavelengths to be used.

Simulations were run for 5×10^5 photons for a whole-blood-like medium, three times for each set of the scattering parameters shown in Table 2.1. These values were estimated from references [Yaroslavsky et al., 1996; Roggan et al., 1999; Friebel et al., 2006, 2009] for the 635, 675, and 797 nm wavelengths. Two oxygen saturation

values were interrogated: 70%, and 100% corresponding to normal values of venous and arterial oxygen saturation respectively. The absorption coefficients of blood in mm^{-1} were estimated using the specific extinction coefficients ϵ tabulated in [Prahl] (converted to $\frac{mm^{-1}}{(moles/L)}$) in the expression:

$$\mu_a(\lambda) = \frac{2.303}{W_{Hb}}[c_{HbO_2}\,\epsilon_{HbO_2}(\lambda) + c_{Hb}\,\epsilon_{Hb}(\lambda)] \tag{2.4}$$

for the haemoglobin's molecular weight $W_{Hb} = 64500$ (g/mole), and the concentrations c given in (g/L).

Table 2.1: Approximate scattering coefficient μ_s, the anisotropy value g, and reduced scattering coefficient μ'_s of whole blood, from selected references at 635, 675, and 797 nm. Data from [Yaroslavsky et al., 1996; Roggan et al., 1999; Friebel et al., 2006, 2009]

Wavelength	Parameter	Yaroslavsky	Roggan	Friebel (2006)	Friebel (2009)
635 nm	$\mu_s\ (mm^{-1})$	64.5	85	90	85
	g	0.98	0.98	0.97	0.977
	$\mu'_s\ (mm^{-1})$	1.29	1.70	2.70	1.96
675 nm	$\mu_s\ (mm^{-1})$	65.36	82.9	88.77	83.27
	g	0.9825	0.98	0.97	0.9753
	$\mu'_s\ (mm^{-1})$	1.14	1.66	2.66	2.06
797 nm	$\mu_s\ (mm^{-1})$	68	76.50	85	78
	g	0.99	0.98	0.97	0.97
	$\mu'_s\ (mm^{-1})$	0.68	1.53	2.55	2.34

Reflectance at 635, 675 and 797 nm ($S(\lambda = 635nm)$, $S(\lambda = 675nm)$,and $S(\lambda = 797nm)$ respectively) from simulations are shown in Fig. 2.6, where values are referred to the reflectance at the isosbestic point at 797 nm to allow comparison. Despite the lack of agreement between the reflectances estimated for each set of optical properties, all exhibit the largest reflectance difference at a wavelength of 635 nm.
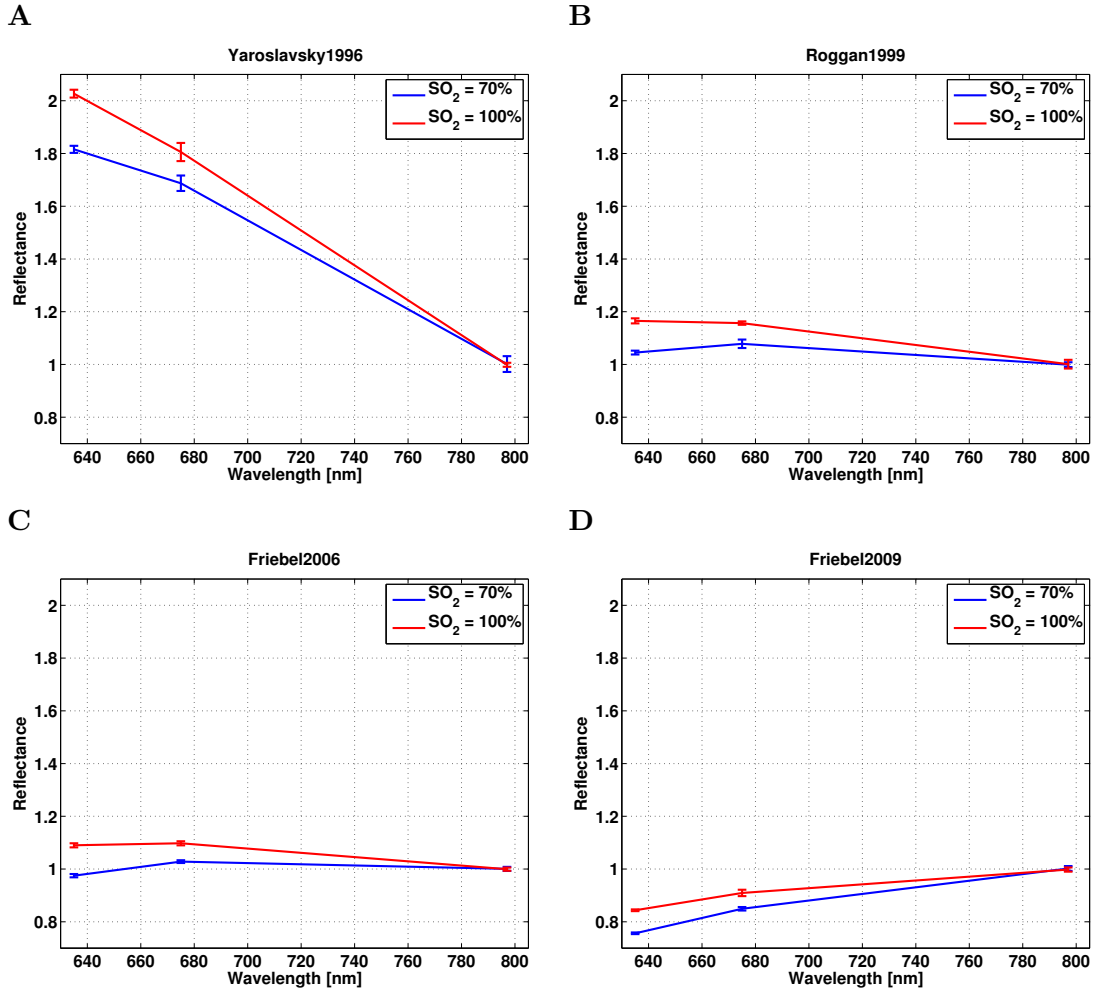
Figure 2.6: Normalised reflectance plotted against wavelength obtained with computer simulations for the optical properties in Table 2.1. Values are referred to the reflectance at 797 nm. The two curves in each plot correspond to oxygen saturation of 70% and a 100% corresponding to common values for venous, and arterial blood. Commercially available light sources at 635 and 675 nm were compared to select the most sensitive to the difference in oxygen saturation.

Table 2.2 shows the expected variation of the reflectance from 70% to 100% SO_2 for the two sources under evaluation. The highest variations were found for the 635 nm source, and therefore this light source was selected for the system, and used for the acquisition of the experiments here presented.

The set of optical properties which exhibited the smallest changes in reflectivity was that of Friebel et al (2009), denoting a variation with respect to the reflectance at 797 nm, of 8.7% by using the source at 635 nm, and 6.0% by using the source at 675

nm, while the largest change was obtained using Yaroslavsky's properties. It can be observed from Table 2.1 that the overall scattering in Yaroslavsky's data decreases more dramatically than the other references for these specific wavelengths. Further, for Friebel (2009) the scattering increases for these wavelengths, thus enhancing the interactions at 675 nm; although not enough to overtake overall absorption in tissue at 635 nm, this effect restates the importance of taking into account the wavelength dependence of the scattering properties for the design of the experiment.

Table 2.2: Simulated difference of the reflectance from whole-blood with 70% and 100% SO_2, with respect to the reflectance at the isosbestic point at 797 nm

Reference	$S(\lambda = 635nm)$ %	$S(\lambda = 675)$ %
Yaroslavsky 1996	21.1	11.8
Roggan 1999	12.0	7.8
Friebel 2006	11.5	7.0
Friebel 2009	8.7	6.0

Simulated response curves

As seen in Eq. 2.2, the oximeter sensitivity depends on the relation of the spectrum intensity at the two chosen wavelengths where the direct mapping to a SO_2 value is adjusted due to the fibre geometry. Given the small size of the DCF, the purpose of this work was sought to know whether the detected light would retrieve information of blood in its surroundings. For this reason the ratio of the simulated reflectance spectrum at $\lambda_1 = 635$ nm to that detected at $\lambda_2 = 797$ nm was used to characterise the spectral data (Eq. 2.3). The comparison against the 797 nm haemoglobin isosbestic point yields values which would nearly vary linearly with oxygen saturation. Results of the simulated response of the fibre under this criterion are shown in Fig. 2.7 for two normal haemoglobin concentrations values: 120 and 150 g Hb /L; and for a low concentration of 90 g Hb/L that might indicate an abnormality.

The response of the fibre was simulated for three different haemoglobin concentration, and the average depth reached by the detected photons was determined. A total of 1×10^6 photons were launched three times for each set of possible optical properties of blood in Table 2.1. The slope of each curve is presented in Table 2.3. It can be noticed that the slope increases with haemoglobin concentration in blood. Here, only a change in haemoglobin is modelled by increasing absorption at the tissue. However, in a real case the decrease in haemoglobin is mostly due to a

decrease in the haematocrit level leading to lower scattering. Since the simulations are using the same scattering properties at all haemoglobin concentrations, experimental results at lower haematocrit would likely present less sensitivity (smaller slopes) relative to results at higher haematocrit.

Table 2.3: Value of the slopes within 95% confidence bounds from Fig. 2.7.

Reference	Hb 90 g/L	Hb 120 g/L	Hb 150 g/L
Yaroslavsky 1996	0.57 ± 0.17	0.58 ± 0.22	0.62 ± 0.34
Roggan 1999	0.27 ± 0.02	0.28 ± 0.09	0.38 ± 0.16
Friebel 2006	0.25 ± 0.08	0.30 ± 0.14	0.36 ± 0.10
Friebel 2009	0.21 ± 0.08	0.22 ± 0.05	0.27 ± 0.05

As seen in Fig. 2.7 and Table 2.3, the slope of the response to SO_2 is higher for the lower scattering found in reference [Yaroslavsky et al., 1996]. From table 2.1, the set of properties in this reference presents large scattering differences at the two wavelengths with μ'_s of 1.29 and 0.68 (mm^{-1}) at 635 nm and 797 nm respectively, where μ_s and g increase with wavelength. In contrast for reference [Friebel et al., 2009], where the lowest slope was obtained, μ'_s values are 1.96 and 2.34 (mm^{-1}) at 635 nm and 797 nm, with both, μ_s and g decreasing with wavelength. Comparing these two references as the extreme cases, μ_s is higher for Friebel (2009), while g is higher for Yaroslavsky. A higher anisotropy values entail fewer photons being backscattered to the fibre. On the other hand, more scattering provides the tissue with the opportunity to absorb more photons. Therefore, the fewer photons reaching the fibre in Fig. 2.7 A, have at the same time undertaken less scattering-absorption events; while for Fig. 2.7 D, more photons are detected with a larger pathlength. Given the dependence of the scattering and absorption coefficient with wavelength, Fig. 2.7 D would likely be compensating to some extent the large difference in absorption at both wavelengths, hence lowering sensibility. From these results large sensitivity of the probe can be expected if the value of g and μ_s are large. Furthermore, if the scattering is approximately constant it could lead to the response curve to cross the unity value following the trend of the absorption coefficient which is lower for oxyhaemoglobin at 635 nm than that at 797 nm, and the opposite for deoxy-haemoglobin.
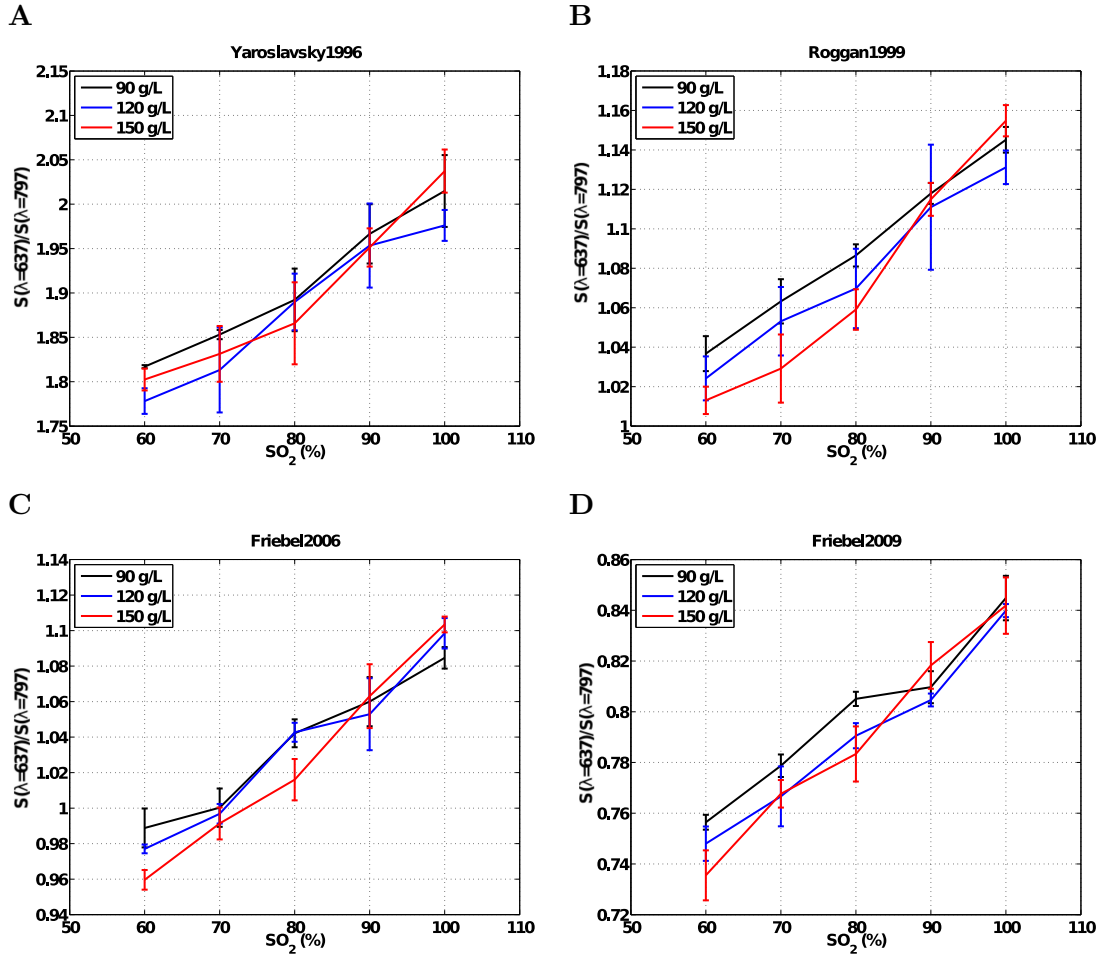
Figure 2.7: Monte Carlo simulations of the sensitivity of the reflectance ratio (Eq. 2.3 to changes in SO_2). The plots show the ratio of the reflectance spectrum at 635 nm to that at 797 nm against the oxygen saturation. Blood was simulated at three haemoglobin concentrations: 90, 120 and 150 g/L. The slopes of each curve are shown in Table 2.3

Using this DCF, the pathlength is fundamentally limited by the short source-detector separation which was a value of 28,5 µm as measured from the DCF's centre to the middle point of the inner cladding ring (having a total radius if 52.5 µm from the centre to the limit if the inner cladding). To illustrate light penetration in tissue the mean depth reached in the medium by the detected photons for an haemoglobin concentration of 120 g/L is plotted in Fig. 2.8 for the reflectance values at 635 nm and 797 nm. The MC code saves the maximum depth reached by each photon falling into the detector, the average depth plotted was then obtained as the mean value of this parameter for all the back-reflected photons. The shallowest depth achieved in

these simulations is 85 µm. Assuming normal haematocrit level of 40%, and RBC volume of 86 fL [Shinton, 2007], the volume contained in a semi sphere of 85 µm radius would hold about 6000 RBCs to be interrogated.
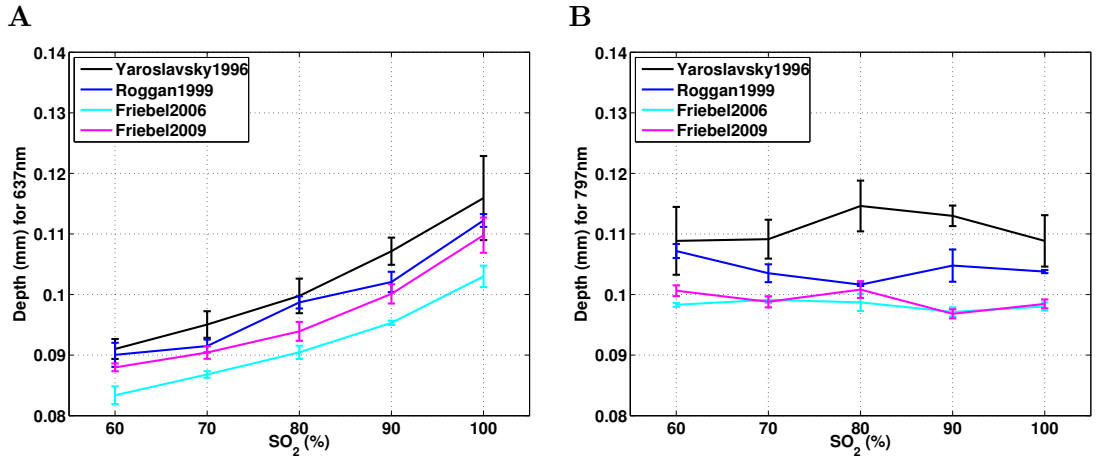
Figure 2.8: Mean detected photon depth plotted against wavelength obtained with computer simulations for the optical properties in Table 2.1 at 635 nm and 797 nm. The lowest penetration depth of 85 μm is estimated for the data in [Friebel et al., 2006] at 635 nm and 60% oxygen saturation. This depth is presumably enough for the detection of haemoglobin properties at the tip of the fibre given the RBC diameter (7 μm).

The low penetration of light will limit the sensitivity of the probe since the photons cannot undergo many interactions before being detected. Further investigation on the capabilities of the DCF to detect SO_2 in blood was carried out experimentally. This is shown in next section, where the fibre was tested in red blood cells (RBC's) solutions with different oxygenation.

As an example of the absorption taking place in the tissue, Fig. 2.9 shows the results from the tissue array in the MC simulation at the two wavelengths being used with a 70% (upper row), and 100% (lower row) SO_2. These images are then obtained for an haemoglobin concentration of 120 g/L, and with the data from Friebel (2006) at which the overall scattering remains approximately the same (μ'_s of 2.7 and 2.6 mm^{-1} at 635 nm and 797 nm respectively). Absorption at 797 nm is qualitatively the same at both oxygenation values, whereas is lower for 70% oxygenation, and larger for 100% at 635 nm.

A

SO$_2$= 70; wavelength = 635

B

SO$_2$ = 70; wavelength = 797

C

SO$_2$= 100; wavelength = 635

D

SO$_2$ = 100; wavelength = 797
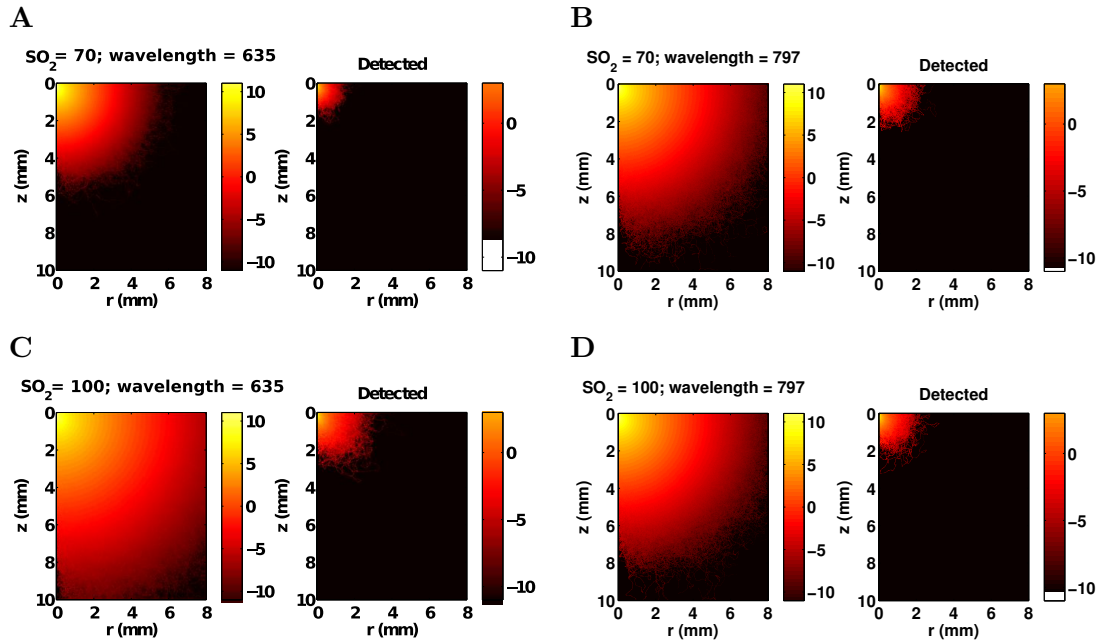
Figure 2.9: Tissue array for the case a concentric detector and source fibres. The left heat map shows all the absorption that took place in the medium. Right hand heat maps show the undergone absorption by the detected photons. Four cases are presented for comparison, all for Hb=150 g/dL and the scattering properties in [Friebel et al., 2006]: **A** $SO_2 = 70\%$ at 635 nm; **B** $SO_2 = 70\%$ at 797 nm; **C** $SO_2 = 100\%$ at 635 nm; **D** $SO_2 = 100\%$ at 797 nm.

2.3 Oxygen Saturation changes in the physiological range
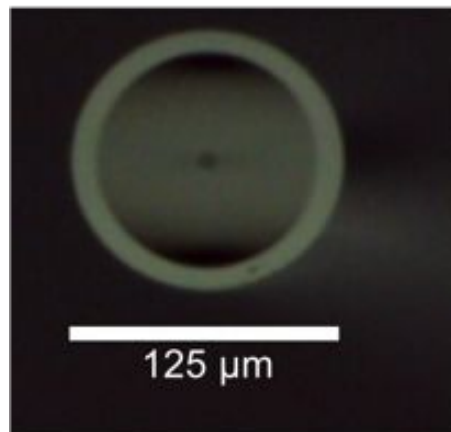
Figure 2.10: Cleaved tip of the double clad fibre used in this thesis. The fibre's outer diameter is 125 µm with a thickness of 10 µm, and a 9µm core.

The performance of the DCF to detect oxygenation changes was empirically analysed in RBC solutions with the physiological range of 60% to 100% oxygen saturation. A broadband light from a supercontinuum source from 780 to 880 nm (Superlum BLM-S-820) attenuated by introducing a gap of 7cm between two collimators, was combined with a 635 nm laser source (Thorlabs), and directed via a monomodal fibre to the core of a the DCF by means of a coupler. The tip of the DCF was immersed into the blood sample whose oxygenation was to be determined. Light scattered by the sample was detected by the inner core of the DCF and coupled to a multimodal fibre that delivers the light to a spectrometer (MayaPro, Ocean Optics, Inc). Acquired spectra were then analysed. The DCF was attached to a translation stage that allow the introduction of the fibre into the sample.The setup is shown in Fig. 2.11.
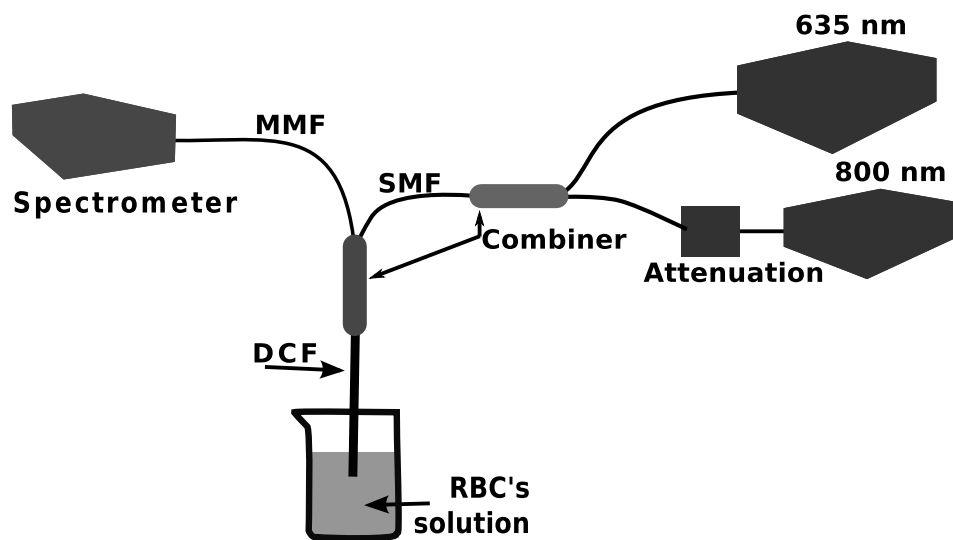
Figure 2.11: Experimental setup. Two light sources deliver light to the DCF single-mode core. The detected light at the inner cladding is sent to a spectrometer and the data are acquired with LabVIEW.

De-oxygenated blood samples were prepared in a test tube as described in section 2.3.2 and placed in a 10 mL beaker for spectra acquisition. Prior to the blood spectra acquisition a set of back-reflection measurements in water were recorded using the same integration time used for the blood samples. The fibre was rinsed in deionised water after each acquisition. Re-oxygenation was achieved by agitating the RBC solution with air in the syringe and leaving to rest for a couple of minutes prior to the spectra acquisition.

The reference values for oxygen saturation were obtained by drawing 2 mL of the

sample and measuring it with a IL682 CO-oximeter (Instrumentation Laboratory, Massachusetts, USA). The IL682 CO-oximeter is a laboratory desktop instrument based on the optical interrogation of a thin layer of the sample at 6 wavelengths: 535, 585, 594, 626, 638, and 667 nm. The accuracy and precision of the IL682 for oxygen saturation measurements, as specified by the manufacturer, is of $1 \pm 0.5\%$.

2.3.1 Calibration and back-reflection measurements

A calibration spectrum to eliminate the effect of uneven illumination from the source was obtained by placing the tip of the fibre close to a white reference surface (spectralon). To estimate the systematic variation of the spectrum due to effects other than those induced by the light source in the sample, a back-reflection spectrum was also collected; this signal was subtracted from all the blood measurements. All measurements were performed with the light of the room turned off. Spectra from blood samples were calibrated by dividing the spectrometer output by the calibration spectrum previously corrected with the back-reflection subtraction as follows.
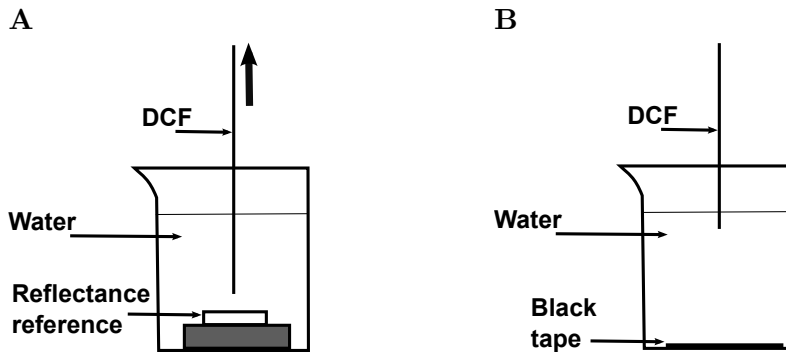
Figure 2.12: **A** Calibration for source spectrum. The DCF was immersed in water at a distance less than 1mm from the reflectance standard surface. **B** Correction from the light reaching the cladding without entering the external medium. This back-reflection measurement was performed with the DCF immersed in water and an approx. distance of 3cm from a black tape placed at the bottom of the beaker

Calibration, $S_{ref}(\lambda)$, and back-reflection spectra, $S_{brRef}(\lambda)$ were acquired after having cleaved the fibre. Additional back-reflection measurements $(S_{brSample}(\lambda))$ were acquired using the same integration time used for the acquisition of each sample spectrum, $S_{sample}(\lambda)$. The calibration was done by placing the tip of the fibre at close proximity (less than 1 mm) to a reflectance standard surface (Spectralon, Labsphere, North Sutton, USA), which was immersed in deionised water (Fig. 2.12

A). Back-reflection measurements were acquired with the fibre immersed in water at 3 cm from a black tape placed at the bottom of a beaker (Fig. 2.12 B). Fifty spectra were acquired each for a 10 ms integration time. From this reference spectrum it was noticed that the peak from the laser source was located at 637 nm instead of 635 nm [5].

Correction from the light source spectrum and back-reflection correction were performed for each sample over the whole wavelength range according to Eq. 2.5:

$$S(\lambda) = \frac{S_{sample}(\lambda) - S_{brSample}(\lambda)}{S_{ref}(\lambda) - S_{brRef}(\lambda)} \tag{2.5}$$

Figure 2.13 shows the spectra for the calibration and back-reflection measurements of the DCF. It can be noticed that back-reflection, although small in intensity, is still present despite the two separated channels used for illumination and detection. This is likely due to an imperfect cleave resulting in a surface cut with a very small angle that reflects the light back to the cladding.
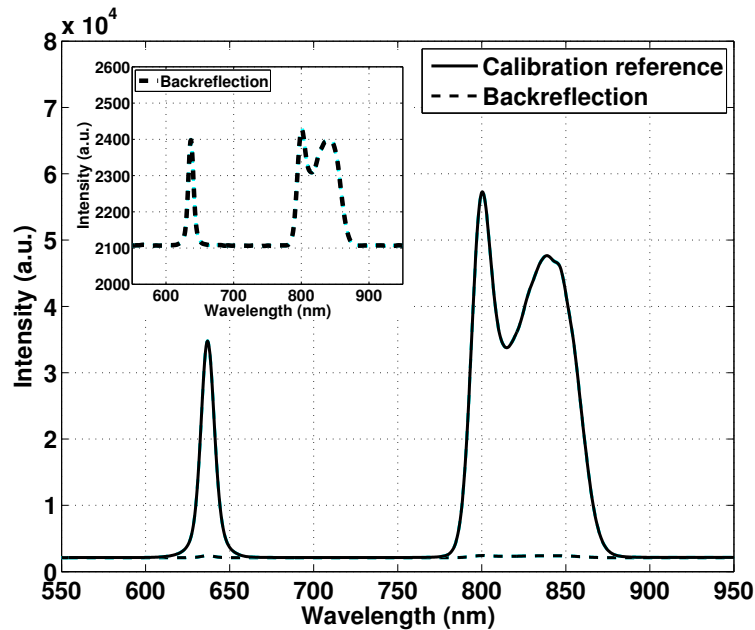
Figure 2.13: Calibration and back-reflection spectra for the DCF immersed in water. The back-reflection spectrum, enlarged in the box, is almost negligible compared to the spectrum from the reflectance reference.

---

[5]Misalignments in the detector were unlikely since the spectrometer had gone through calibration in the previous months (by Ocean Optics, order 1410795) with a regression fit of 0.999999703

In order to determine whether the calibration measurements were reproducible, the dependence of the fibre-reference distance on the ratio of the reflectance at 637nm to the reflectance at 797 nm was analysed. The DCF was placed at the closest distance from the spectralon surface (0.5 mm approx.) and then moved farther for each acquisition.

Figure 2.14 A displays the distance dependence of the calibration measurements while Fig. 2.14 B shows the exponential decay of both signals with distance. As consequence of the increase of the ratio $\frac{(S\lambda=635nm)}{S(\lambda=797nm)}$ in the calibration measurements at larger distances, the sensitivity to oxygen saturation changes would decrease (from Eq. 2.5). A preventive measure to avoid this to happen, was to ensure the closest possible distance from the fibre to the spectralon.

A   **B**
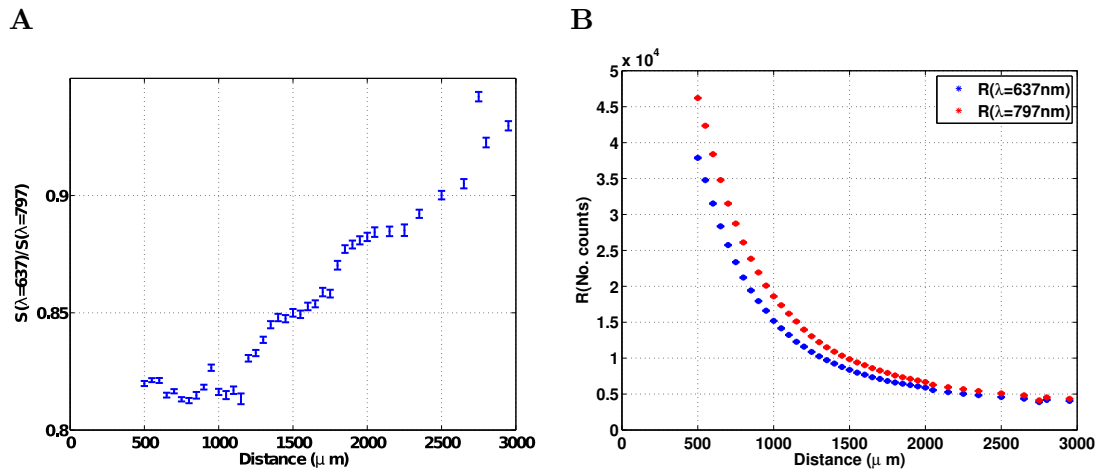
Figure 2.14: **A** Calibration dependence to the fibre-reference distance. After a millimetre distance from the reflectance surface the ratio starts increasing **B** Intensity from the spectrometer for each wavelength showing an exponential decay with distance.

2.3.2   RBC solutions

RBC solutions were prepared from expired donated red blood cells (RBCs) obtained from the UCL Hospital Blood Transfusion Laboratory. The RBCs were directly diluted with phosphate buffered saline (PBS) solution 0.01 M, taking into account the 100 mL of additive solution in each donation bag, to achieve a haematocrit about 40%, although for some samples this initial concentration was diluted.

The chosen method for de-oxygenating the RBC solution was the use of yeast.

Yeast are fungi that consume oxygen by diffusion when in an oxygenated medium. The yeast strain used in this work is Saccharomyces cerevisiae (baker's yeast) which, as can be seen from the microscope images shown in Fig. 2.15, are comparable in size to red blood cells (approx. 7 microns).

A

B
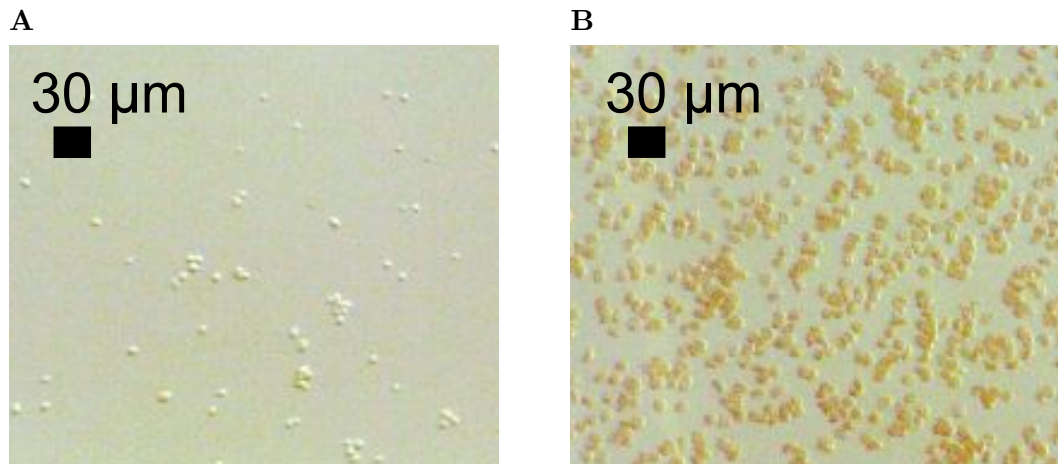
Figure 2.15: Microscope images of:**A** Yeast in PBS, and **B** RBCs in PBS showing that the sizes of both types of cells are comparable. Colour and contrast correction was done in GIMP image editor.

Yeast has been used in several NIR studies of haemoglobin de-oxygenation [Wang et al., 2009; Sharma et al., 2011; Liu and Vo-Dinh, 2009; Sevick et al., 1991]. Liu et al.[Liu and Vo-Dinh, 2009] added 1 mg/mL yeast to their phantoms containing haemoglobin. In this work they found that yeast could make a small impact on the optical properties, so these properties could vary while the yeast is being dissolved.

An investigation of yeast optical properties [Beauvoit et al., 1993] found an absorption coefficient μ_a lower than $0.0002mm^{-1}$, and a reduced scattering coefficient μ_s' lower than $0.16mm^{-1}$ for concentrations lower than 10 mg dry weight/mL of Saccharomyces cerevisiae. Given the low amounts of yeast used in these experiments (under 5 mg/mL), and the high μ_s' for whole blood found in the literature [Yaroslavsky et al., 1996; Roggan et al., 1999; Friebel et al., 2006, 2009] $(1.9 \pm 0.6mm^{-1})$ together with the uncertainty between the provided values, the contribution of yeast's optical properties to the results was not considered.

2.3.3 Results

Back-reflected light

As seen in Fig. 2.13, the DCF still receives back-reflected signal. Given the small source-detector separation provided by the DCF, and the high optical absorption from whole blood, it was necessary to verify that the spectrum collected from the RBC solutions carried enough information from the sample to be analysed. Figure 2.16 compares the amount of signal from the blood sample to the back-reflected signal from the source acquired at the same integration time (200 ms). In this figure, it can be noticed that the signal from the sample is about five-fold larger than the back reflected signal from the source leaving enough information to be processed and analysed.
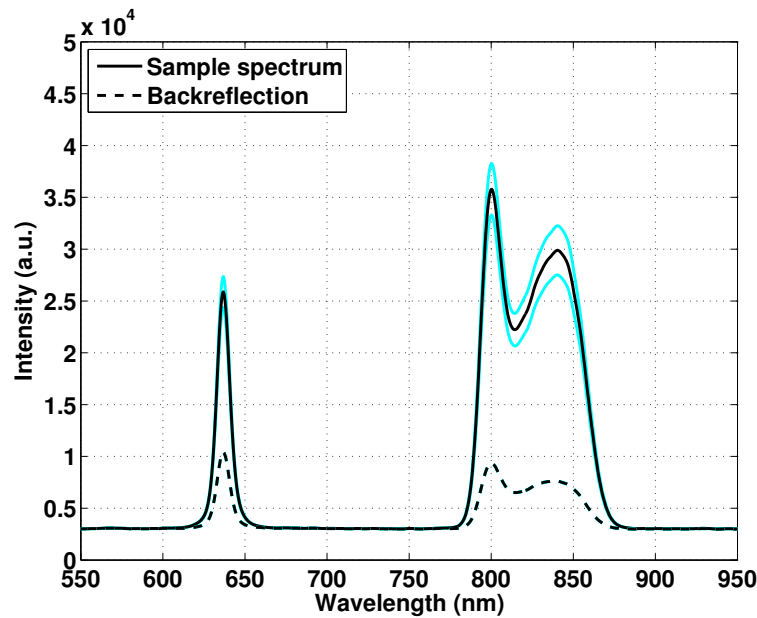
Figure 2.16: RBC solution and back-reflection spectra for the DCF immersed in water. The back-reflection spectrum in this case is higher given the integration time needed for the sample spectrum acquisition.

Response to SO_2

Results of experiments on 3 samples are shown in Fig. 2.17. The 50 spectra acquired at each SO_2 value was corrected using Eq. 2.5. After this step, each point in the plot was obtained as the mean ratio and standard deviation of the spectrum at $\lambda_1 = 635$

nm to that at $\lambda_2 = 797$ (Eq. 2.3). The integration time was 300 ms for A, and 200 ms for B and C. The haemoglobin content and yeast concentration varied among the samples (Table 2.4). Sample A had the highest concentration of haemoglobin, while samples B and C were diluted solutions.

Table 2.4: Haemoglobin and yeast concentration for each of the samples tested.

Sample	Hg (g/dL)	Yeast (mg/mL)
A	11.7	1
B	8.7	3.5
C	9.8	3
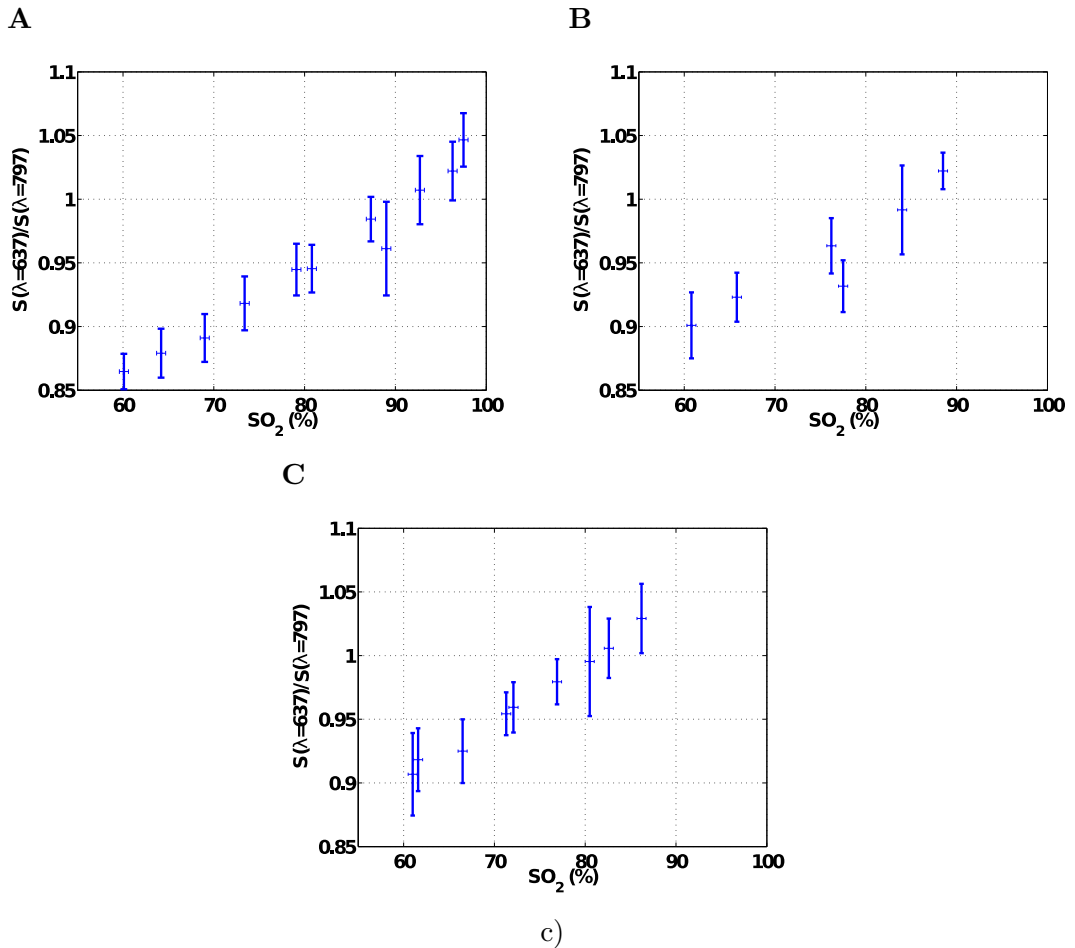
Figure 2.17: Experimental response of the fibre to changes in SO_2. The plots show the mean ratio of the reflectance spectrum at 637 nm to that at 797 nm (from 50 spectra at each point). The oxygen saturation for each sample was measured with the IL682 CO-oximeter.

The slope and intercept of each plot was calculated in order to compare the sensitivity of the measurements to changes in oxygen saturation (see Table 2.5). These set of results show good repeatability with values of the slope between 0.4 and 0.5, with the sample B exhibiting more variation. Compared with simulated curves in Fig. 2.7, these results suggests that the scattering of the RBC solutions might not be highly wavelength dependant since the curve crosses the unity as in the case for reference [Friebel et al., 2006]. The higher slope found in the experimental results may indicate an overall larger scattering causing an increase of interaction events. There was no significant difference in the slope of the curves with respect to the haemoglobin concentration for the interrogated samples nor was there any noticeable correlation with the amount of yeast added for the this set of samples, which may suggest a degree of insensitivity to scattering variation.

Table 2.5: Value of the experimental slopes and intercepts obtained with the Matlab built-in function fit, shown with their corresponding standard deviation.

Sample	Slope	Intercept
A	0.45 ± 0.02	0.59 ± 0.02
B	0.43 ± 0.07	0.64 ± 0.06
C	0.48 ± 0.02	0.61 ± 0.02

Sources of error

Although the sensitivities given by the slopes of the curves in Fig. 2.17 are encouraging for SO_2 detection, the high uncertainties must be also pointed out. For instance, data in Fig 2.17 A presents the highest interrogated SO_2 range. Here, the 0.025 and 0.02 standard deviation in the slope and intercept values respectively means that a given value of $Response(SO_2)$ as given by 2.3, can correspond to any value of SO_2 in a range of 18%.

The high standard deviation for each sample is possibly due to the Brownian motion of the RBCs directly beneath the fibre. Variation in signal amplitude, however, may be caused by other factors such as accumulation of cells on the fibre surface, bubble formation, and rapid settling of RBCs under gravity in the solution after mixing. The cell accumulation at the tip of the fibre can be seen in Fig. 2.18. The fibre was used for one measurement, and then, rinsed with water afterwards, a procedure followed for all measurements.

Another factor that might influence the outcome of the experiments is the after-

math of the sample mixing which causes bubbles to be created and the cell alignment to the flow. To analyse this, the spectrum from a RBC solution was acquired in two stages: first, 50 spectra were obtained from the sample immediately after mixing every 5 minutes; second, the sample was left to rest and 50 spectra was obtained every 5 minutes without any mixing. The results are shown in Fig. 2.19, which exhibits a large variation in the mean ratio of the spectrum as a consequence of mixing, while a lower variation is present for the unmixed solution. The standard deviations, however, remain at the same level. This would impact the fibre sensitivity in terms of outliers pulling the slope away from the empirical response curve. Using again Fig. 2.17 A as an example, if the value at 89%, which exhibits higher variability among the plotted samples, is removed assuming to represent an error in the acquisition (due to either dirt in the fibre or turbulence in the sample), the resulting slope 0.45 ± 0.021 would reflect that the $Response(SO_2)$ could agree with any value of SO_2 in a range of 14% (instead of the previously mentioned 18%).
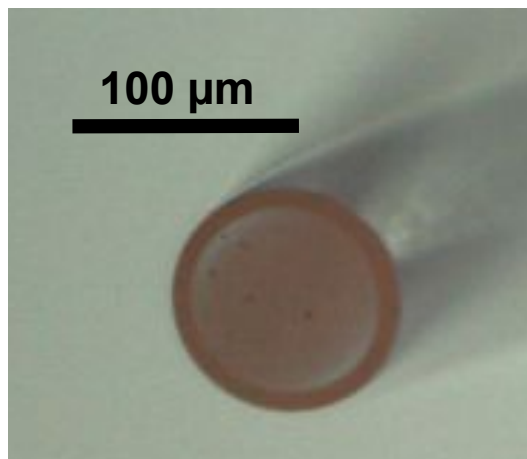
Figure 2.18: DCF tip after being used in a blood experiment and rinsed with water afterwards
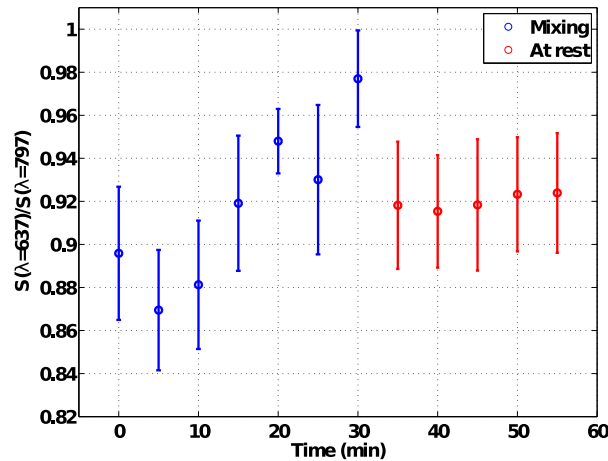
Figure 2.19: Effect of the mixing in the sample for measurements taken every 5 minutes. Symbols in blue correspond to measurements of the sample immediately after mixing with a magnetic stirrer. Symbols in red correspond to the same sample after being left to rest.

Assuming negligible formation of bubbles these results suggest fibre movement in relation to the cells as a possible source of error. To further explore the effect of the fibre's tip movement with respect to a surface, two reference spectra were compared in an effort to have control over the distance from which light is being reflected. For one measurement the fibre was inserted into a 25 gauge spinal needle restricting the movement of the fibre due to vibration or air currents. Fibre and needle were then placed at a distance of 0.5mm from the reflectance standard and the spectra were acquired. A second measurement was performed in exactly the same way, but with the loose fibre (without the needle). A total of 3000 spectra was acquired for each configuration and the mean value and standard deviation at $\lambda_1 = 637$ nm and $\lambda_2 = 797$ nm were obtained in terms of the counts provided by the spectrometer (note that the ratio $\frac{\lambda_1}{\lambda_2}$ is not being used to avoid carrying errors). These values are shown in Table 2.6 together with the calculated signal to noise ratio [6] (SNR).

The SNR of the spectra at 637 nm with the restricted fibre was 3-fold larger than that of the fibre without needle. In the case of the spectra at 797 nm, the difference was 7-fold higher for the fibre in the needle. Since all the parameters remained the same, it can be assumed that the fibre is very sensitive to movement. This feature would not affect a sample with randomly organised cells in which the distance from the fibre tip to the surface of the cells is, in average, the same even if

---

[6]$SNR = \frac{\mu}{\sigma}$ where μ and σ are the mean value and standard deviation respectively of the spectra at the specific wavelength.

the fibre position is changing.

Table 2.6: SNR from spectral measurements taken with the fibre with and without a supporting needle while acquiring spectra from a reference surface. Values of mean and std are given in counts as provided by the spectrometer.

Needle	S($\lambda = 637$nm)			S($\lambda = 797$nm)		
	mean	std	SNR	mean	std	SNR
No	36023	133	271	46516	194	240
Yes	37881	44	854	46206	27	1683

As seen here, the DCF can potentially detect oxygenation differences between venous ($SO_2 = 70$ %) and arterial blood ($SO_2 = 100$ %). The next section analyses the change in the signal from the DCF system under a dynamic change of the fibre environment simulating a needle crossing from a vein into an artery.

2.4 Crossing a barrier between two solutions

The setup was modified to interrogate the DCF under a dynamic scenario, in which the fibre crosses a boundary between two RBC solutions with different or identical oxygenation. The modifications were made on the target arrangement.

The new setup is shown in Fig. 2.20. A plastic tube is sealed at one end using a piece of nitrile as shown in the figure box. The tube is then attached to a beaker using a thermometer holder. The tube and the beaker are then both filled with a RBC solution (see Fig. 2.21). Three combinations of SO_2 solutions were investigated as summarized in Table 2.7. The DCF was placed in a 25 gauge spinal needle and positioned inside the tube.
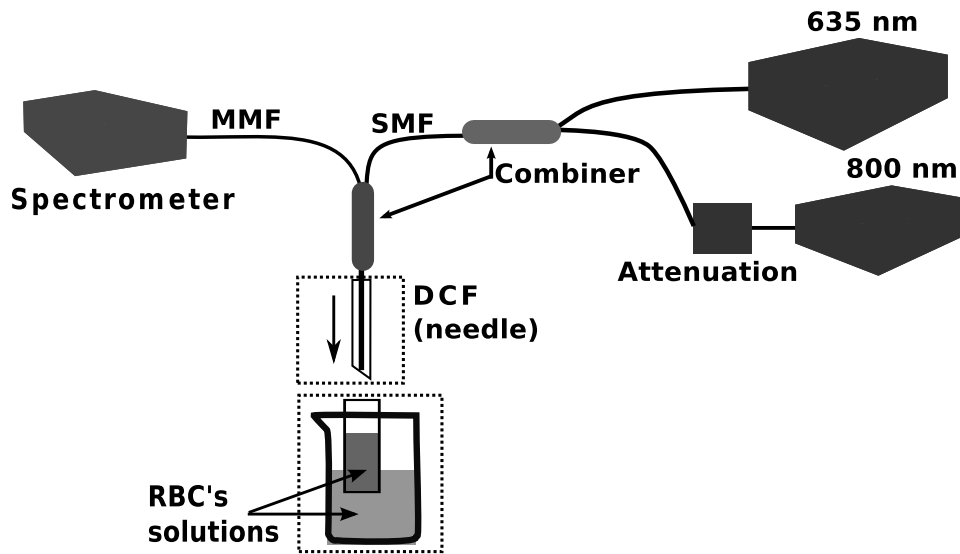
Figure 2.20: The experimental arrangement was changed from its configuration in 2.11 to allow for the presence of two contiguous blood samples. A tube of 5 cm length and 8 mm diameter was held from the beaker using a thermometer holder. The lower end of the tube was closed with a small piece of nitrile. The DCF was introduced into a 25 gauge spinal needle to provide the stiffness needed to cross the barrier at the end of the tubing.
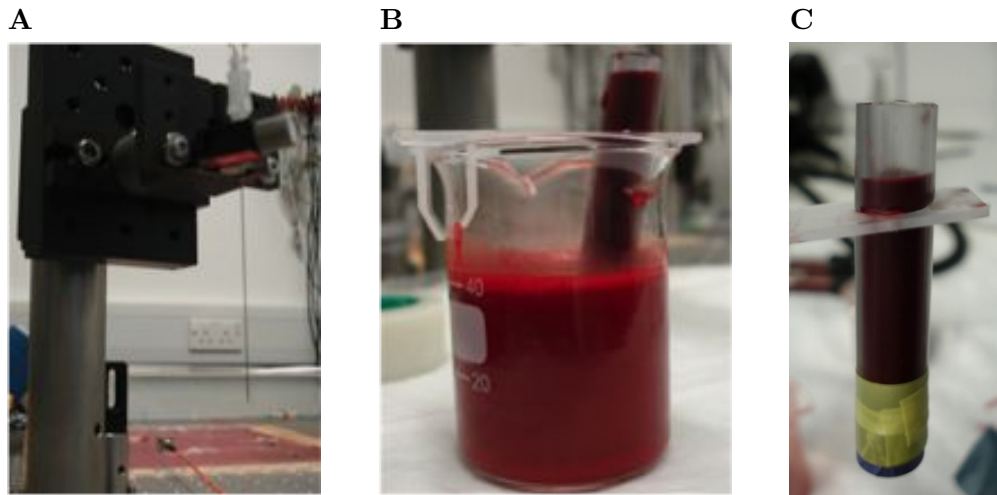
Figure 2.21: **A** Picture of the needle containing the fibre, which corresponds to the upper box of the setup illustrated in Fig. 2.20. **B** Whole sample assembled. In this picture the tubing contains the de-oxygenated RBCs solution and the beaker contains the oxygenated RBCs solution. **C** Tubing containing the first medium reached by the fibre. The bottom of the tubing is sealed with nitrile, which can be easily pierced by the needle.

Table 2.7: Values of SO_2 for the three combinations presented.

	SO_2	
	beaker	tube
A	98%	98%
B	74%	74%
C	98%	74%

The DCF tip was cleaved at the beginning of each acquisition and calibration data were recorded by acquiring 50 spectra from the reference surface, and back-reflection with 10 ms integration time. The measurements on RBC solutions were performed with an integration time of 200 ms. The LabVIEW code used in the previous section was modified to continuously acquire spectra, while plotting the ratio $\frac{S(\lambda=635nm)}{S(\lambda=797nm)}$ on a graph. After leaving the fibre in the tube for some seconds, the needle was advanced until it crossed the nitrile barrier into the second solution. The spectrum acquisition was performed approximately in 4 minutes, corresponding to 2.5 minute of the fibre in the first medium, and less than 2 minutes in the second medium. Measurements of RBC solutions with yeast prepared in the same manner exhibited a variation of about 2% of SO_2 after an hour, therefore no significant variation is expected here in the oxygenation values of the samples used during the period of each individual measurement.

2.4.1 Results

Figure 2.22 shows the results obtained for these sets of experiments. The SO_2 for the oxygenated sample was 98% in all cases, and the SO_2 for the de-oxygenated sample was 74% for B and C. Total haemoglobin content was 12.4 g/dL and 12.3 g/dL for the oxygenated and the de-oxygenated sample respectively. The needle containing the fibre was advanced two minutes after starting the acquisition, and penetrated the barrier about half a minute later.
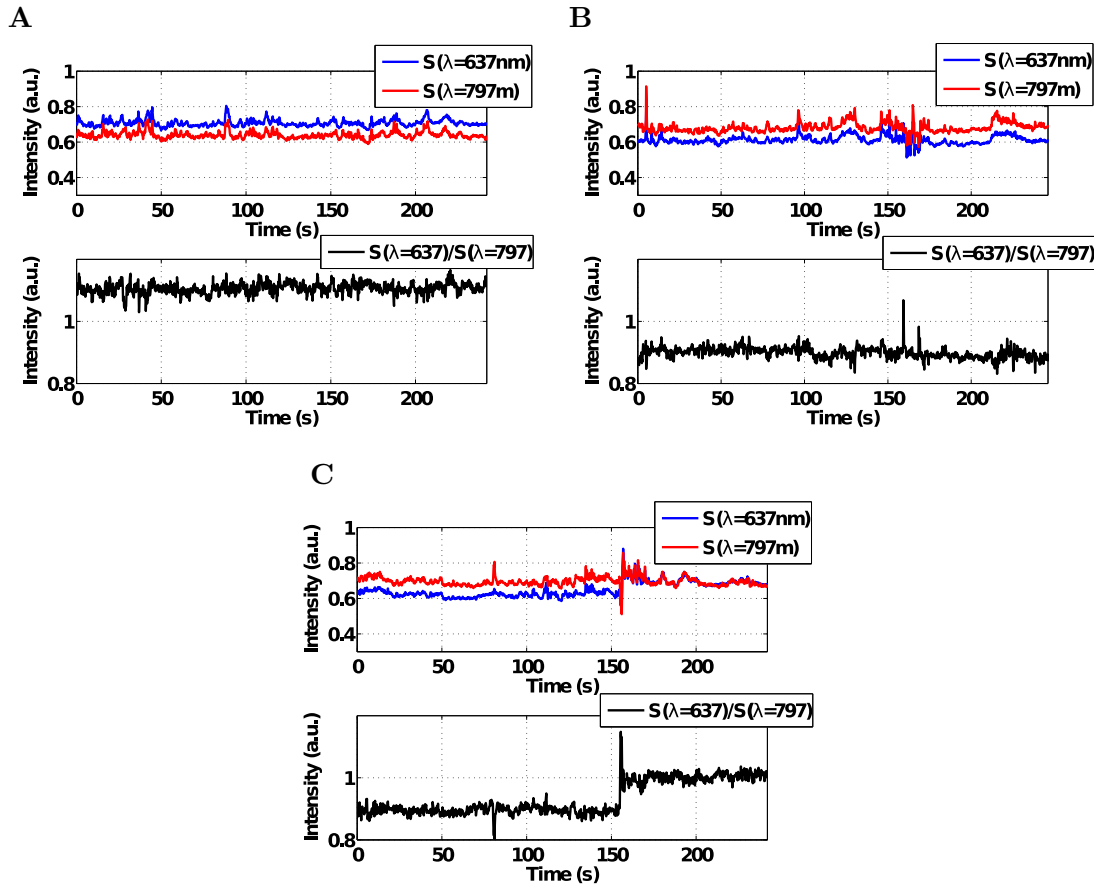
Figure 2.22: Ratio of the reflectance at 637nm to that at 797 at each acquisition. The fibre is crossing from the the blood in the tube to the blood in the beaker. **A** 98-98 % tubing-beaker SO_2 ; **B** 74-74 % tubing-beaker SO_2 ; **C** 74-98 % tubing-beaker SO_2

When the oxygenation was the same on either side of the barrier, no significant change was observed except of a perturbation at the moment the fibre crossed the barrier in Fig. 2.22 B. For the case when the oxygenation was different, the first 200 spectra and the last 200 spectra were averaged and the change in the ratio was found to be 0.11 for a 24% change in SO_2.

2.5   Discussion

The need for verification of the correct placement of a needle or catheter into a vein before the advancement of large bore cannulas is of the utmost importance to

prevent severe complications, injuries, and death.

An optical assessment of the probe's placement has been investigated using a small 125 µm double clad fibre to perform reflectance spectroscopy. The particular dimensions of this fibre allow it to be coupled to a variety of the tools used during different stages of a central venous cannulation, ranging from 22 gauge (0.718/0.413 mm OD/ID), and 18 gauge (1.27/0.838 mm OD/ID) needles to larger catheters, and smaller guide wires. Since the purpose of the probe would be to assess the device's placement, the fibre can be housed into a small tubing[7] which can itself be drawn into a needle or used as a guide wire. This would allow the physician to carry out with the procedure in a traditional way and remove the optical probe after placement confirmation.

Reflectance spectroscopy offers a simple method using safe power levels without the need of exogenous contrast agents. However, given the small separation between the light source fibre and light collection region, combined with the high absorption of blood, the use of this fibre is limited to the assessment of the tissues immediately surrounding the end of the DCF.

Two wavelengths, 635 nm and 797 nm were selected to identify SO_2 in blood samples. Monte Carlo simulations were performed to explore the viability of the DCF for detecting different SO_2 values using these wavelengths and the optical parameters of blood. These computer simulations predicted that the greatest mean depth that the photons could reach in whole blood was just 115 µm below the fibre.

Experimental measurements of the sensitivity of the probe in RBC solutions showed that the DCF was only able to discern changes in oxygenation for increments greater than 18% (and possibly up to 14%) due to the error in the signal inherent to the small diameter and further processing steps. It is also possible that bubbles produced by mixing of the sample contribute to the noise in the signal. Although optical properties from yeast were not taken into account for the results, they might slightly increase the scattering.

In spite of the low sensitivity for small SO_2 variation, the double clad fibre was able to differentiate between blood samples mimicking SaO_2 and SvO_2. A 11% increase of signal is observed when the fibre was translocated from 74% oxygenated blood to 98% oxygenated blood. This change is equivalent to a slope of 0.46 ± 0.07, which is consistent to those obtained for the response curves found in section 2.3.3 (the value of the slope ranging from 0.43 to 0.48).

---

[7]For example: [MicroGroup]

The ability of the DCF to distinguish between oxygenated and deoxygenated blood may be of use during the aforementioned venous cannulation. An example of another possible application would be a transseptal puncture in which a needle is inserted into the vena cava and from there is advanced to the heart in order to gain access to the right atrium. In this case, the DCF coupled into the transseptal needle would be able to feedback when the device goes from the deoxygenated blood filling the right atrium to the oxygenated blood in the left atrium.

Overall the DCF integrated into an interventional device may be useful for needle placement confirmation during those procedures requiring recognition of needle passage from a vein to an artery or vice versa. For this application, the performance of the fibre would require to be interrogated under the condition of blood flux.

Chapter 3

Optical Epidural Catheter for Spectroscopic Tissue Characterisation

Epidural anaesthesia is a medical technique used in pain treatment procedures, post-surgical treatment and during open surgery. In these procedures the applied drug (e.g. lidocaine) can be delivered in a single injection or gradually through a catheter. Depending on the purpose, the anaesthesia target can be the lumbar, the caudal, the thoracic or the cervical epidural space. Caudal epidural is less favoured than lumbar epidural because of lower anaesthetic spread and the possible absence of the sacral hiatus (the sacral hiatus is the zone where the last sacral vertebrae failed to fused, and thus is the place from where the needle is introduced); however, the caudal approach is still commonly used with infants where the puncture site can be easily determined.

Figure 3.1 shows the anatomical boundaries of the epidural space. The epidural space encloses the dural sac within which are located the dura mater, the arachnoid membrane, the spinal nerves and the spinal cord. Nerves roots crossing by the epidural space to the intervertebral foramen are enclosed within the spinal nerve root cuffs, which are surrounded by a lymphatic network. Nerve root cuffs are thought to play an important role in the selective nerve root blockade during epidural anaesthesia [Reina et al., 2008].

The epidural space is not continuous, and is reduced to a "virtual space" regularly at vertebral levels, meaning that the structures normally enclosing the epidural space

are in contact. The anterior part of the epidural space (towards the front of the body) is narrower than the posterior part, and the thickness varies from 1 to 6 mm - being widest at the lumbar level [Bridenbaugh and Cousins, 1998; Cheng, 1963].

FRONT   **BACK**

Periosteum of the foramen magnum

Dural sac

Posterior longitudinal ligament

Ligamentum flavum

Pedicles; outer aspects of the intervertebral foramina

Dural sac

Sacrococcygeal membrane
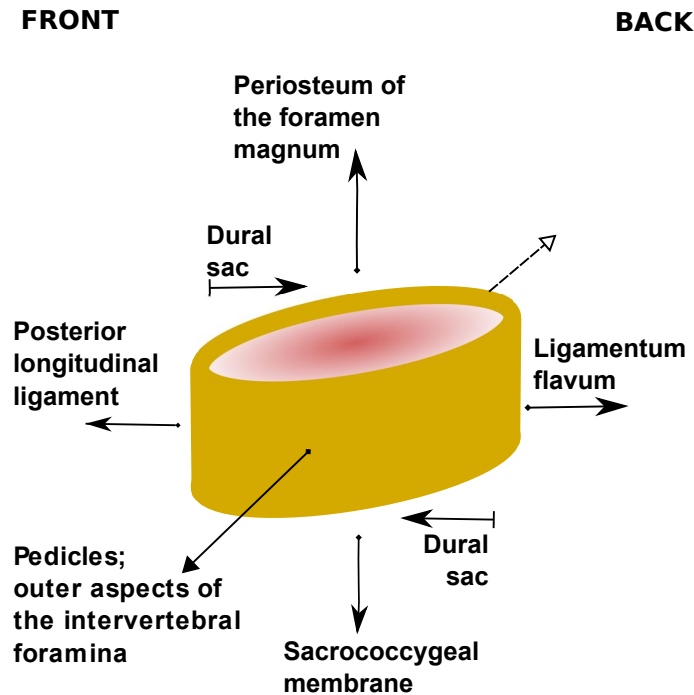
Figure 3.1: Boundaries of the epidural space. To the left is the front of the human body and to the right, the back. The epidural fat encloses the dural sac, and it extension goes from the foramen magnum at the base of the skull to the spine's lower end.

The epidural space, when filled, contains nerves, plexus of veins, fibrous tissue and, in the most part, epidural fat. Arteries in the epidural space are located mainly laterally, while the valve-less epidural veins are located mainly in the anterior and lateral parts of the epidural space, reducing the risk of a misplaced puncture.

It has been determined that the epidural fat works as buffer for the dural sac protecting neural structures of the spine [Reina et al., 2006]. Epidural fat has affinity to drugs with high lipid solubility, which remain in the fat for long periods gradually spreading to the dural sac and the nerve root cuffs. The injected drug can then reach the nerves by diffusion processes through the dural sac and the nerve root cuffs.

In an uneventful well-placed needle insertion, a catheter is typically inserted into the epidural space through a Tuohy needle (usually 18 gauge with 1.27/0.838 mm OD/ID), which is a specially designed curved needle to allow the inserted catheter

to exit the lumen at 45 degrees. With the Tuohy needle in place, the catheter is inserted through the cannula beyond its tip, the needle is withdrawn, and the catheter is left in place (see Fig. 3.2).
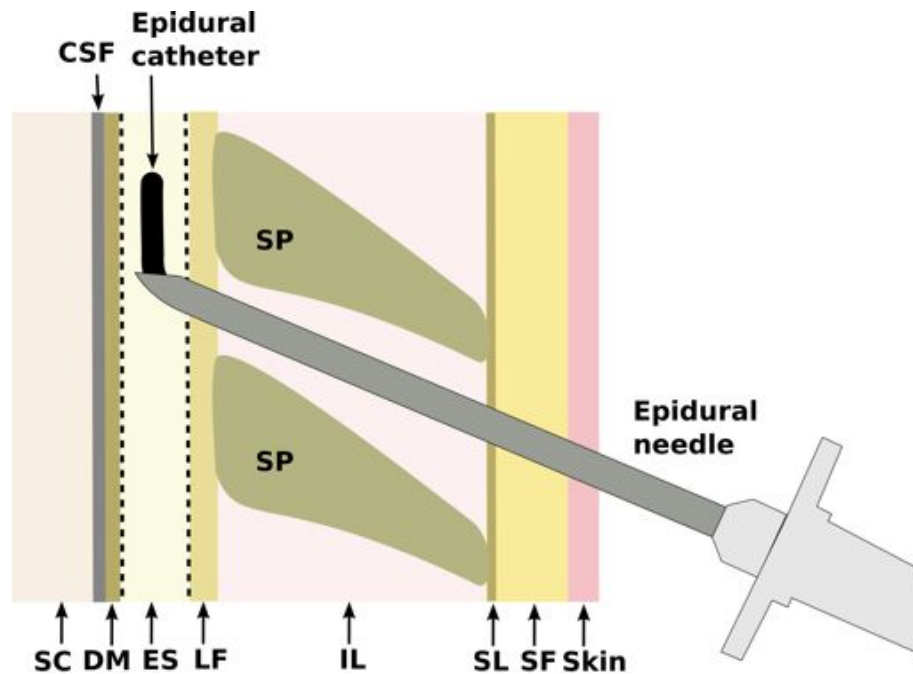
Figure 3.2: Simplified schematic of tissue structures in the vicinity of a needle-catheter insertion into the epidural space. SF: subcutaneous fat; SL: supraspinous ligament; IL: interspinous ligament; SP: spinous process; LF: ligamentum flavum; ES: epidural space; DM: dura mater CSF: cerebrospinal fluid; SC: spinal cord. Typical thickness of the dura mater, the epidural fat, and the ligamentum flavum are 0.3 mm, 6-13 mm, and 1.4-4.7 mm, respectively [Reina et al., 1999, 2006; Abbas et al., 2010]

In many clinical contexts, needle and catheter insertions into the epidural space are performed without image guidance, and therefore there is a significant risk that they are inserted into vascular structures. Intravascular injections can cause toxicity to the nervous and cardiovascular systems that can, if undetected, result in complications such as convulsions, hypo-ventilation, arrhythmias, hypotension, tachycardia, and cardiac arrest. Current methods for detecting intravascular injections, which include aspirations [1] and test doses [2] are not completely effective . Moreover, even if epidural catheters are correctly positioned, their tips can migrate into blood vessels due to patient motion [Fivez et al., 2010; Burns et al., 2001]. In women, there is an

---

[1]An aspiration takes place to confirm that neither blood nor cerebrospinal fluid is found

[2]During a test dose, the patient reaction after a small dose of epinephrine is injected, indicates whether it was a successful or failed placement

increase in the size of the venous plexus during pregnancy, which may elevate the risk of intravascular catheter tip misplacement.

Recently, several studies [Ting et al., 2010; Rathmell et al., 2010; Desjardins et al., 2011; Lin et al., 2012] have investigated the use of optical reflectance spectroscopy to guide the placement of needles into the epidural space. With this technique, integrated optical fibres deliver light to tissue at the distal end of the needle and receive a portion of the reflected light. In the visible wavelength range, prominent light absorbers include oxyhaemoglobin and deoxyhaemoglobin; in the near-infrared, they include lipid, and water. The optical spectra of the received light can be processed to highlight differences in the concentrations of these chromophores and differences in the wavelength-dependence of optical scattering. As such, they can be used to perform tissue classification. With in vivo porcine and human studies, the potential to directly detect incorrect placement of needles into vascular structures was also demonstrated [Brynolf et al., 2011; Balthasar et al., 2012a]. However, in spite of the research on the Tuohy needle insertion, little has been done on the improvement of the placement monitoring of epidural catheters.

3.1   Optical catheter system

As demonstrated in the previous chapter, reflectance spectroscopy can be employed to safely interrogate tissue with optical fibres. When a double clad fibre is used, the short source-detector distance allowed the interrogation of the surrounding tissue at the very tip of the device. During epidural anaesthesia, this feature is not useful since the catheter can migrate while delivering the drug, and the detection of blood once in the vessel would hence be too late. In this scenario, it is necessary to detect vascularities in advance in order to avoid accidental vascular puncture. To address this necessity, it was proposed to use an optical epidural catheter with embedded optical fibres for constant monitoring of the device's tip using reflectance spectroscopy, ensuring that the source-detector separation is large enough for prompt haemoglobin detection.

Specifications of this new catheter need to comply with the dimensions of a commercial epidural catheter (the dimensions of a commonly used 20 gauge epidural catheter are 0.85, 0.45, and 1000 mm for the outer diameter, inner diameter and length respectively [B.Braun]), and be able to contain optical guides within its wall. The material needs to be of medical grade, and flexible enough to be curved into

the epidural space.

A custom catheter was developed with an outer diameter of 842 µm, an inner diameter of 447 µm, and a length of 1 m. These dimensions were consistent with those of commercial epidural catheters. Four light guides were integrated into the catheter wall. Each light guide had an outer diameter of 125 µm and a core diameter of 109 µm. The light guides were arranged symmetrically (Fig. 3.3).
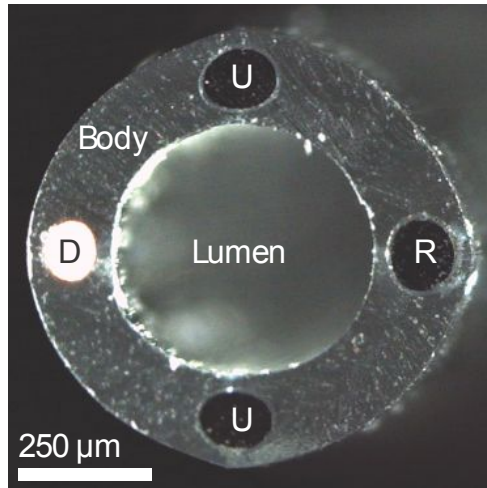
Figure 3.3: Distal end of the optical catheter. D: delivery light guide; R: receive light guide; U: unused light guide.

The catheter was developed with a polymer extrusion process (Paradigm Optics, Vancouver, WA) that included polystyrene for the body, PMMA (polymethyl methacrylate) for the light guide core, and THV 500G (a polymer of tetrafluoroethylene, hexafluoropropylene and vinylidene fluoride) for the light guide cladding. While the optical light guides had a transparent visual appearance, prominent absorption in the near-infrared in the vicinity of 730 nm, 900 nm, and 1000 nm were apparent in the transmission spectrum (Fig. 3.4). These absorption peaks are consistent with previous studies [Zubia and Arrue, 2001]. The transmission spectrum was measured using one of the light guides from an optical catheter (1 m length) and a silica/doped-silica core/cladding fibre (AFS105/125, Thorlabs; 1 m length) as a reference.
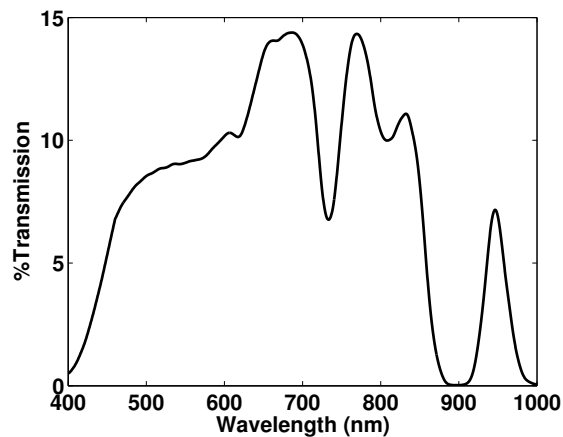
Figure 3.4: Transmission of the polymer guides embedded in the catheter. Prominent absorption peaks can be seen at wavelengths of 730, 900 and 1000 nm.

At the proximal end of the catheter, 15-20 cm of the light guides were exposed by dissolving the polystyrene body with cyclohexane (Fig. 3.6 **A**) by carefully rubbing the fibre with a cotton bud. Two of the light guides on opposite sides of the catheter were connectorised. When exposed, the light guides had diameters slightly larger than 125 µm (which probably occurred due to incomplete dissolution of the surrounding polystyrene), so a diameter of 230 µm was chosen for the inner lumen of the SMA connectors. One of the optical guides was very delicate for what it seemed to be a fabrication issue, and could not be detached completely from polystyrene (see Fig. 3.5); this and the opposite light guide were not used in this study.
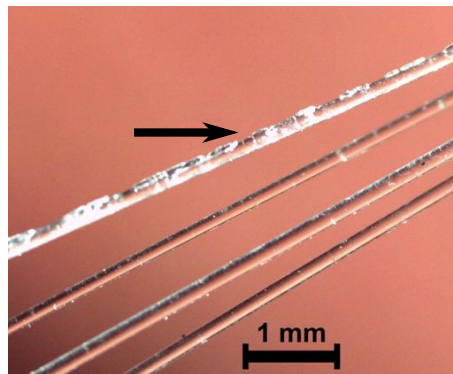
Figure 3.5: The four light guides after exposure. The guide indicated by the arrow was resistant to the cleaning process; the figure shows the best cleaning achieved.

Access to the catheter lumen for fluid injections was provided by coupling the proximal end of the catheter to a commercial catheter. This coupling was performed

with a metal tube that was obtained from a 27-gauge needle (413/210 mm OD/ID) with a length of 15 mm (Fig. 3.6 B). The ends of this metal tube were inserted into the lumen of the optical and commercial catheters to distances of 7 mm and secured with epoxy (F120, Thorlabs).

A   **B**
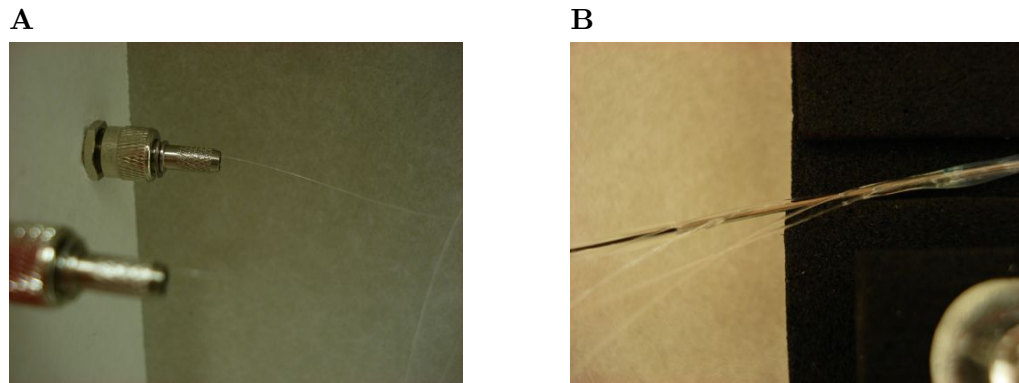
Figure 3.6: **A** Fibres connectorised to the SMA connectors. **B** Part of a 27-gauge needle linking the prototype catheter with a commercially available catheter for flushing of the system.
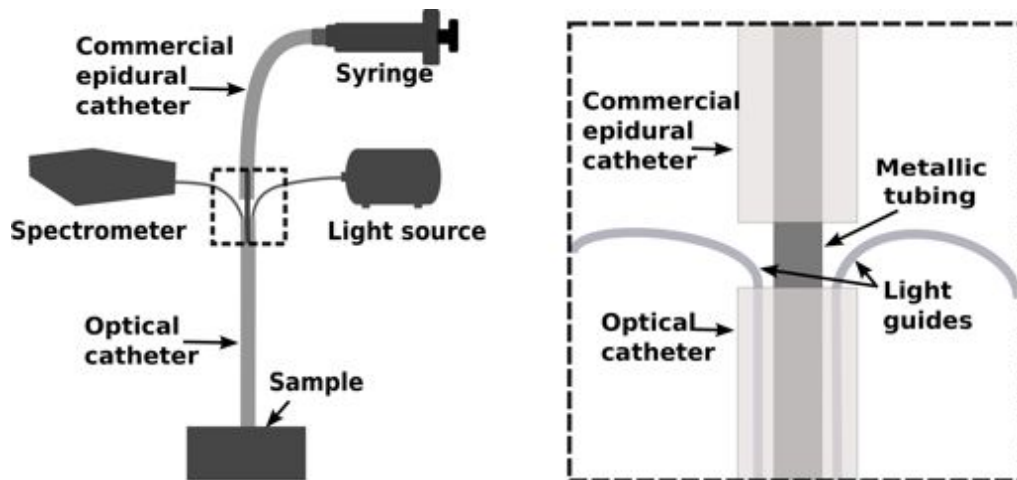
Figure 3.7: System schematic. The two connectorised light guides are connected to the source and detector, respectively. At the proximal end, the optical catheter is coupled to a commercial epidural catheter with metallic tubing to allow for fluid to be injected into the lumen.

For the spectroscopic acquisitions, one connectorised light guide delivered broadband light to tissue from a tungsten-halogen source (HL-2000, Ocean Optics). The other received reflected light from tissue and delivered it to a spectrometer with a

silicon detector array (MayaPro, Ocean Optics). The system schematic is shown in Fig. 3.7.

The spectrometer was interrogated with custom software written in LabVIEW v.10.01 (National Instruments, Austin, TX), which provided a real-time display of the raw and processed spectra. The processing of the spectra acquired from tissue, $S_{tissue}(\lambda)$, included two steps: correction for background and for the light source spectrum. Background correction involved subtraction of a dark current spectrum, $S_{dark}(\lambda)$, which was obtained with the light source turned off. Correction for the light source spectrum involved division by a background-corrected reference spectrum, $S_{ref}(\lambda)$, which was acquired from a diffuse reference standard (SRM-99, Labsphere, North Sutton, NH) with the catheter tip positioned 1 mm above the surface. These processing steps, which generated a calibrated tissue spectrum $S(\lambda)$, are summarized by Eq. 3.1:

$$S(\lambda) = \frac{S_{tissue}(\lambda) - S_{dark}(\lambda)}{S_{ref}(\lambda) - S_{dark}(\lambda)} \qquad (3.1)$$

To facilitate interpretation of the calibrated spectra, two parameters were calculated. The first parameter, H, was calculated from the values of the calibrated spectrum at two isosbestic points of the haemoglobin absorption spectrum, $\lambda_1 = $ 797 nm and $\lambda_2 = $ 545 nm, as shown in Eq. 3.2:

$$H = \frac{S(\lambda_1) - S(\lambda_2)}{S(\lambda_1)} \qquad (3.2)$$

The haemoglobin parameter, H, was previously defined in a study that investigated the detection of intravascular penetration events during needle insertions performed for nerve blocks in human patients [Balthasar et al., 2012a]. This parameter involves two wavelengths at isosbestic points of the haemoglobin spectrum for which absorption at one wavelength (λ_2) is much larger than at the other wavelength (λ_1), and so making H sensitive to total haemoglobin content ($HbO_2 + Hb$). The sensitivity of H to the haemoglobin concentration may be more clearly understood in terms of the absorbance. As seen in Eq. 1.19 (section 1.3.1), absorbance for a total haemoglobin concentration c_{Hb} at wavelengths λ_1 and λ_2 is given by:

$$A(\lambda_1) = \epsilon(\lambda_1)\, c_{Hb} L\ DPF + G$$
$$A(\lambda_2) = \epsilon(\lambda_2)\, c_{Hb} L\ DPF + G \qquad (3.3)$$

and the difference of absorbance:

$$A(\lambda_1) - A(\lambda_2) = c_{Hb}(\epsilon(\lambda_1) - \epsilon(\lambda_2)) \, L \, DPF \qquad (3.4)$$

In eq. 3.4 the term $(\epsilon(\lambda_1) - \epsilon(\lambda_2))$ is an optical property of the haemoglobin and remains constant, and L is a fixed geometrical distance. Therefore, provided that the optical scattering is constant at the two different wavelengths (and subsequently is the pathlenght scaling factor, DPF), a change in the absorbance difference will correlate with a change in haemoglobin concentration.

Given that $S(\lambda)$ is measuring the transmitted light T coming back from the tissue, and that $A = -log_{10}T$, the H parameter can be rewritten as:

$$H = 1 - 10^{[A(\lambda_1) - A(\lambda_2)]} \qquad (3.5)$$

where $A(\lambda_2) > A(\lambda_1)$.

Accordingly, an increase in the haemoglobin parameter is consistent with an increase in the haemoglobin content of tissue from which the spectrum is derived assuming that haemoglobin is the principal absorber of tissue at those wavelengths. The normalizing term $S(\lambda_1)$ in eq. 3.2 is used to compensate for any changes in overall intensity.

The second parameter was the intensity I, which was calculated as the average value of a calibrated spectrum over the whole wavelength range of 450 nm to 850 nm. Variation of the average intensity in the spectrum (the average of total transmitted light T) may also depend on the presence of other chromophores and scatterers in tissue and not only on the total haemoglobin content. Additionally, the total reflected intensity might also be affected by the difference in light propagation within aligned structured tissues such as muscles or ligaments. However, the abundance or lack of haemoglobin is hypothesized to be followed by noticeable changes of overall intensity.

Note that the parameter H does not give a quantification of haemoglobin concentration in the tissue, but rather both, H and I are meant to provide a quick estimation of the interrogated tissue.

3.1.1   Monte Carlo analysis for penetration depth estimation.

Monte Carlo simulations were performed with the custom software described in Chapter 2. Figure 3.8 shows the geometry use for the simulations, where the source-detector separation (as measured from the centre of the delivery light guide to the centre of the retrieving light guide) was 644 µm to match the geometry of the optical catheter (Fig. 3.3). The position from which photons entered tissue was sampled from a probability distribution derived from the spatial dimensions of the light guide core and the numerical aperture (NA) of the light guide. With the refractive indices of THV and PMMA taken to be 1.35 and 1.49, respectively, the NA of the light guide was 0.63.
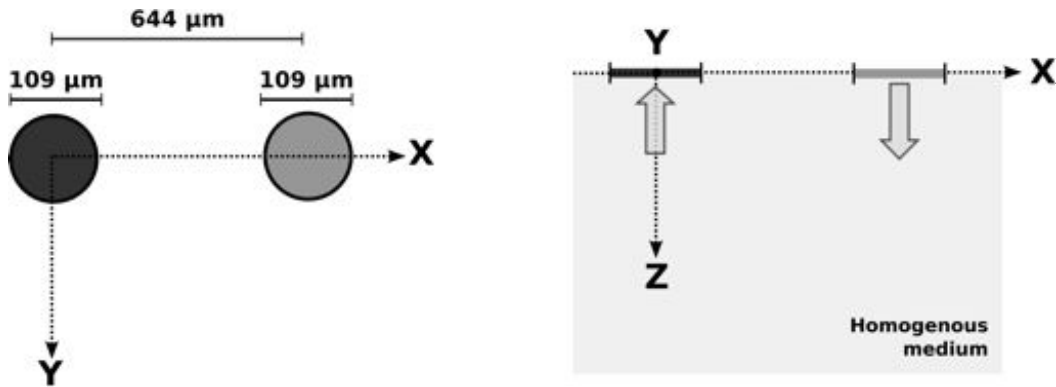
Figure 3.8: Geometry of the MC simulation. The detection fibre is centered in the XY plane. Light is emitted by a fibre 644 µm away from the delivery fibre.

The optical properties for two tissue types were used in the simulation of photon propagation: blood with 80% oxygenation (tissue to be detected), and adipose tissue (main constituent of the epidural space). For each tissue type, simulations were performed for 6 wavelengths that spanned the wavelength range of 450 nm to 850 nm. At each wavelength, 6 simulations were performed, with 1.5×10^6 photons used in the simulation. The scattering properties of blood and adipose tissue were obtained from Friebel et al. [Friebel et al., 2006] and Bashkatov et al. [Bashkatov et al., 2005], respectively. The absorption coefficients of these tissues were obtained from tabulated data [Prahl; Arifler et al., 2006].

Figure 3.9 shows the results from the tissue array in the MC simulation at three wavelengths, 545, 797, and 850 nm, with data from fat (left column), and blood (right column) tissues. In the case of fat, higher absorption and scattering events

can be noticed at 545 nm for this set of wavelengths. Blood absorption at the same wavelength, is so high that light is completely absorbed after just few steps into the tissue, and the back-reflected light is almost null. It is evident from these images that the difference in absorption by blood at 545 and 797 nm (the two wavelengths used to determine the H parameter) would produce drastic differences in the reflected light when compared to fat interrogation.
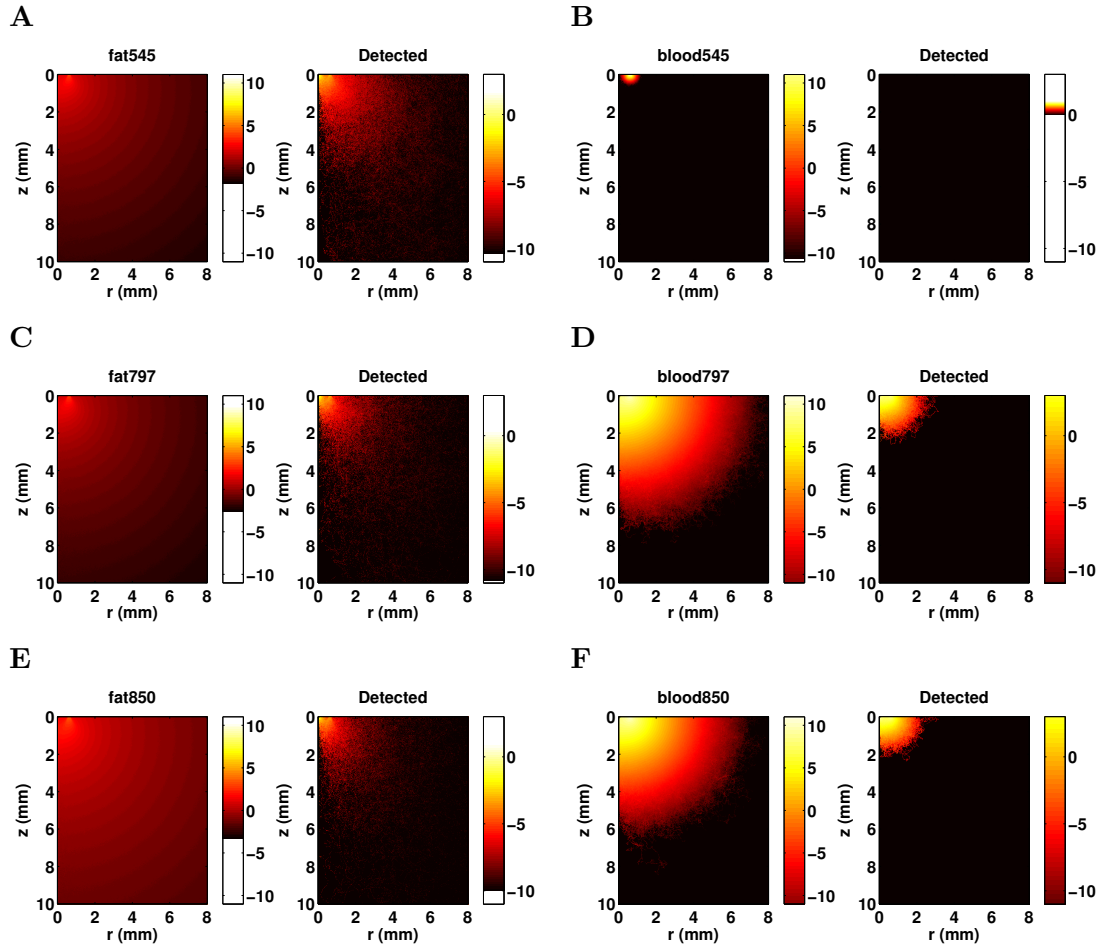
Figure 3.9: Tissue array for the case of a detector and source fibres separated by 644 μm, at z=0. The left heat map shows all the absorption that took place in the medium. Right hand heat maps show the undergone absorption by the detected photons. Six cases are presented for comparison: **A** fat at 545 nm; **B** blood ($SO_2 = 80\%$) at 545 nm; **C** fat at 797 nm; **D** blood ($SO_2 = 80\%$) at 797 nm; **E** fat at 850 nm; **F** blood ($SO_2 = 80\%$) at 750 nm.

According to the Monte Carlo simulations, the relative intensities of light obtained at two isosbestic points of the haemoglobin absorption spectrum, 545 nm and

797 nm, varied between adipose tissue and blood. As described in the introduction, these tissues are clinically significant: the target location for epidural catheters is the adipose tissue within the epidural space, and complications can arise when epidural catheters enter veins and anaesthesia or opioids are inadvertently introduced into the bloodstream. The average depth reached by the detected photons was greater overall for adipose tissue than for blood (Table 3.1). For adipose tissue, it varied from 0.90 mm to 1.03 mm for the wavelengths used in the simulations. For blood, it varied from 0.06 mm at 545 nm (where haemoglobin absorption is prominent), to 0.51 mm at 797 nm (where it is less prominent). Table 3.1 also shows the reflectance values calculated by normalizing the number of detected photons at a given wavelength to those at 797 nm.

The range of this probe (0.5-1 mm) may be useful for the earlier detection of a vessel after a slow catheter displacement. An abrupt catheter movement could be sensed afterwards, which still could be useful in the clinic to detect and correct catheter placement errors.

Table 3.1: Tissue Reflectivity and Average Maximum Depth for Adipose Tissue and Venous Blood Calculated with Monte Carlo Simulations.

		Simulated Parameters				Calculated values	
	WL	μ_a	μ_s	g	μ'_s	Avg. max.	Relative
	(nm)	(mm^{-1})	(mm^{-1})		(mm^{-1})	depth (mm)	reflectance (a.u.)
Fat	450	0.0064	16.5	0.9	1.65	0.90 ± 0.66	1.3442 ± 0.0016
	545	0.0008	14.5	0.9	1.45	0.94 ± 0.68	1.2580 ± 0.0011
	650	0.0005	12.8	0.9	1.28	0.98 ± 0.70	1.1365 ± 0.0012
	750	0.0010	11.7	0.9	1.17	1.01 ± 0.71	1.0320 ± 0.0013
	797	0.0004	11.2	0.9	1.12	1.02 ± 0.72	1.0000 ± 0.0021
	850	0.0006	10.7	0.9	1.07	1.03 ± 0.73	0.9550 ± 0.0012
Blood	450	35.4	65	0.95	3.25	0.04 ± 0.01	0.0250 ± 0.0002
	545	25.3	65	0.95	3.25	0.06 ± 0.02	0.0357 ± 0.0003
	650	0.52	75	0.97	2.25	0.49 ± 0.20	0.7868 ± 0.0011
	750	0.35	75	0.97	2.25	0.52 ± 0.23	0.9291 ± 0.0013
	797	0.4	75	0.97	2.25	0.51 ± 0.22	0.8829 ± 0.0007
	850	0.5	75	0.97	2.25	0.49 ± 0.21	0.8053 ± 0.0008

With adipose tissue, the intensity of light at 545 nm was 1.25 fold of the intensity of light at 797 nm; with venous blood, the later was 25 fold of the former. The haemoglobin values calculated from these relative intensities are shown in Table 3.2:

Table 3.2: Haemoglobin parameter for the MC simulations of blood and fatty tissue as obtained by Eq. 3.2.

	H value	Std
Fat	-0.2580	0.0029
Blood	0.9596	0.0003

3.2 Ex-vivo tissue differentiation during the laminectomy of a swine

A laminectomy[3] at a lumbar level of a spine was performed that ultimately exposed the spinal cord. This laminectomy was performed at Northwick Park Institute for Medical Research (NPIMR) by Dr. Simeon West; Anaesthesiologist. The intact adult swine (Large White; female; 50 kg) was received approximately 15 minutes after sacrifice, and the laminectomy was conducted within a time period of 2 hours. The swine had been used in the context of an in vivo experiment by another research group that involved a superficial skin experiment. Therefore, as verified by the NPIMR, additional ethics approval was not required for the experiments conducted in this study. The previous experiment did not affect the lumbar region of the spine and did not involve the use of optical contrast agents.

The laminectomy was performed in stages. At each stage, a new tissue layer was revealed, and the catheter was manually positioned with its distal tip perpendicular to the tissue surface (Fig. 3.10). Care was taken not to exert pressure on the tissue with the catheter. Spectra were obtained from the surfaces of tissue types commonly encountered by the distal tip of an epidural catheter: ligamentum flavum, epidural fat, and dura mater. Additionally, spectra were obtained from a 5 mL sample of venous blood extracted from the epidural venous plexus that was placed in a test tube (diameter: 1 cm); the catheter was positioned in the centre of the sample. For each tissue type, 20 spectra were acquired with a 1 second integration time per spectrum.

---

[3]Surgical procedure in which a part of the vertebra (the lamina) is removed.
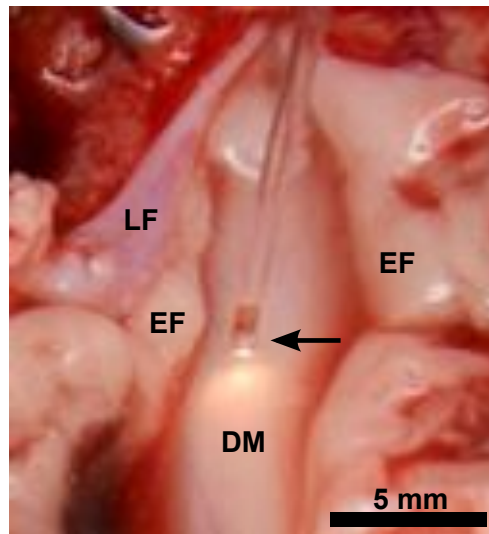
Figure 3.10: The region around the spinal cord showing the tip of the optical catheter (arrow) on the surface of the dura mater (DM). Adjacent to the DM were the epidural fat (EF) and the ligamentum flavum (LF).

3.2.1   Results

The results of the spectra and their corresponding haemoglobin and intensity parameters are shown in Fig. 3.11. The black soft curve shows the mean spectrum of the 20 spectra taken at each location, with the standard deviation plotted as the red noisy curves.

The spectra acquired from tissues during the laminectomy exhibited absorption peaks, which manifested as lower signal intensities within specific wavelength ranges. Absorption peaks at wavelengths in the range of 500 nm to 600 nm were consistent with the presence of haemoglobin [Prahl], which included those at 542 nm and 576 nm (oxy-haemoglobin) and 556 nm (deoxy-haemoglobin). Deoxy-haemoglobin absorption peaks at 757 nm [Prahl] were not visually apparent.

Several artefacts in the spectra were apparent. The absorption peak at 733 nm corresponds to the prominent absorption peak of the light guides shown in Fig. 3.4 and is consistent with imperfect background subtractions or white-balancing. Further, negative regions in the spectra acquired from blood arise from imperfect background subtractions. Finally for low intensities of reflected light, changes in ambient light in the room may have affected the spectra.

Pronounced differences in the intensity and haemoglobin parameters obtained

from the withdrawn blood and from the other three tissue types were observed. In particular, the mean intensity parameter obtained from blood tissue was 45-fold smaller than that obtained from adipose tissue. The relative similarities between the mean intensity parameters obtained from the ligamentum flavum, dura mater, and epidural fat were consistent with the very similar visual appearances of these three tissues (mainly whitish). The mean haemoglobin parameter obtained from adipose tissue was 14-fold smaller than that obtained from blood tissue. The relative similarities of the mean haemoglobin parameters obtained from the other tissues were consistent with their white visual appearances.
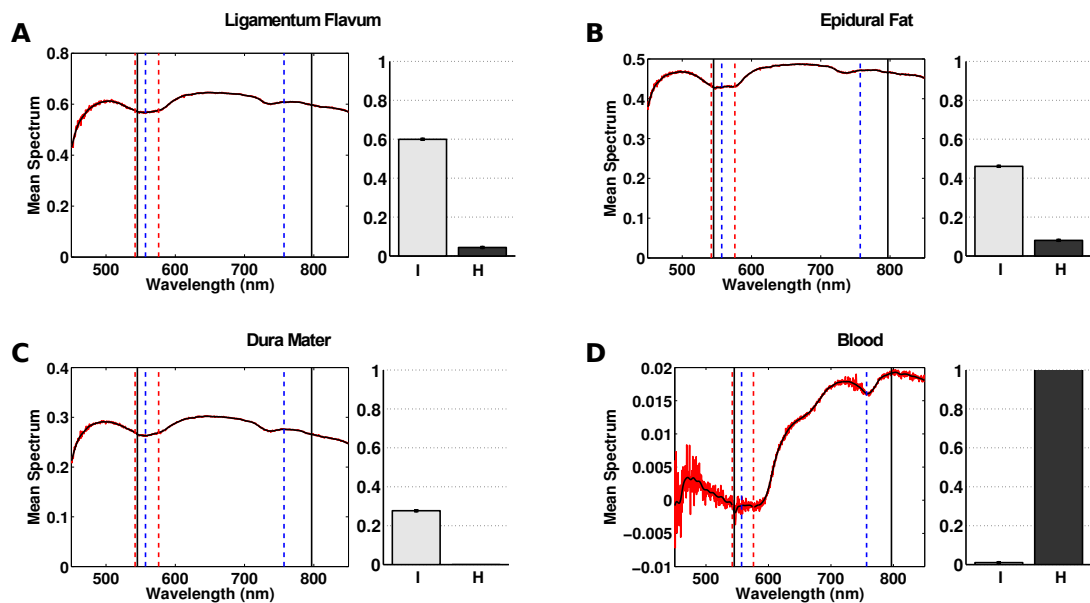
Figure 3.11: Mean spectra acquired during the laminectomy from ligamentum flavum (A); epidural fat (B); dura mater (C); blood (D). Dashed vertical lines correspond to haemoglobin absorption peaks (red: oxy-haemoglobin; blue: deoxy-haemoglobin). Solid vertical lines correspond to the isosbestic points of the haemoglobin absorption spectrum that were used to calculate the haemoglobin parameter. To the right of each spectrum: the corresponding mean intensity (I) and haemoglobin (H) parameters and their standard deviations.

3.3 Automated discrimination between blood and non-blood tissue spectra

With the objective of testing the predictive power of spectra for discriminating between blood-rich versus non-blood tissues, further spectra were acquired with the optical catheter from chicken wings obtained from a meat supplier. Spectra from

blood vessels were expected to exhibit a smaller haemoglobin parameter than that from whole blood, as was the case in the swine experiment mentioned above.

Additionally, it was hypothesized that other features in the spectra can be used to discriminate between tissues with different blood content. To test this hypothesis, an automated statistical learning method was employed for the task of classifying blood-rich versus non-blood tissues. These types of algorithms typically estimate the parameter of a probabilistic model given vectors of data features in a training set in order to predict the class of future samples. The entries of the feature vectors to input into the algorithm was the selected set of 892 wavelengths from 450.317 nm to 849.712 nm as acquired by the spectrometer. Spectra acquired from small vessels surrounded by other tissues were labelled as blood-rich tissues while the remaining spectra were labelled as non-blood tissue.

The spectral acquisition used the same setup as shown in Fig. 3.7. A total of 173 spectra were acquired from 4 chicken wings, with 19 corresponding to skin, 24 to muscle, 45 to fat, 39 to blood vessels, and 46 to fibrous tissue. For each sample the catheter was carefully positioned and 50 spectra were acquired with an integration time of 600 ms. The catheter was flushed and cleaned between acquisitions, and the tip's surface inspected; a new cut and polish of the catheter tip was performed if needed.

3.3.1 Classification

In many scenarios such as the one presented here in which a correctly placed device needs to be left in the body for a prolonged time, an automated discrimination between blood and non-blood tissue in real time would greatly help the physician during the invasive procedure. Using the spectra acquired from chicken tissue as described above, a proof-of-concept test of an automated method for classifying spectra originating from blood-containing and non-blood tissue types was performed. To this end, each spectra was treated as an n-dimensional vector in which each entry was a wavelength readout given by the spectrometer; the distance between wavelengths used are plotted in Fig. 3.12. A principal component analysis (PCA) was performed over the whole set of acquisitions to visualize the spectral space in a two-dimensional plot using the first two principal components.
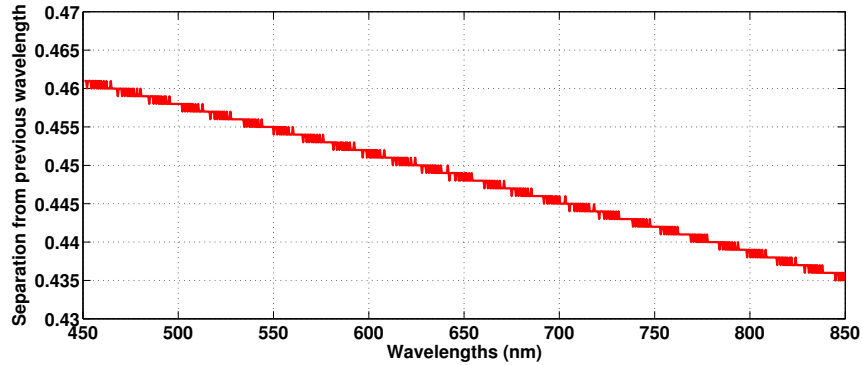
Figure 3.12: The original 892 wavelength set does not comprise wavelengths equally distributed. Values of larger wavelengths were closer to each other than the values of shorter wavelengths.

PCA reduces data dimensionality from n-dimensions (the number of features) to k-dimensions. The PCA analysis finds the k vectors on to which data is projected while minimizing the projection error. The new vectors are found by computing the eigenvectors of the covariance matrix:

$$\Sigma = \frac{1}{m} \sum_{i=1}^{n} (x^{(i)})(x^{(i)})^T \qquad (3.6)$$

where m is the number of samples, and $x^{(i)}$ is the ith sample. In this case the first two principal components ($k = 2$) were chosen so that the discrimination between blood and non blood tissues was visualised.

Figure 3.13 shows the sample set mapped to the first two principal components. It is noticeable that blood and non-blood tissue spectra formed two clusters that were almost completely linearly separable. This analysis suggests that using a simple linear classification method for discriminating blood from non-blood tissue is feasible. Additionally, Fig. 3.14 shows the eigenvector and eigenvalues from the PCA. The large gap from the first to the second eigenvalues, 820.5 to 64.6 respectively, indicates that the most of variance (92%) can be explained with the first component, with an eigenvector for which all wavelengths have a similar magnitude. Furthermore, the second eigenvector embodies the data property that the intensity from larger wavelengths is higher than at shorter wavelengths in most of the spectra.
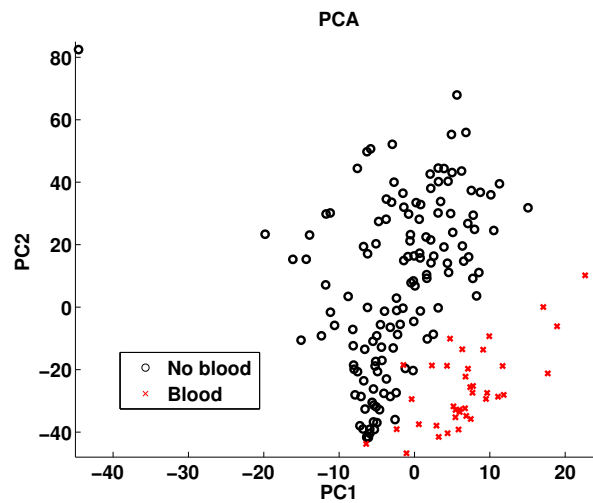
Figure 3.13: Principal components analysis over the 173 instances showing that the spectra, in this case, were able to be linearly separated among the two specified classes: blood and non-blood related tissues.
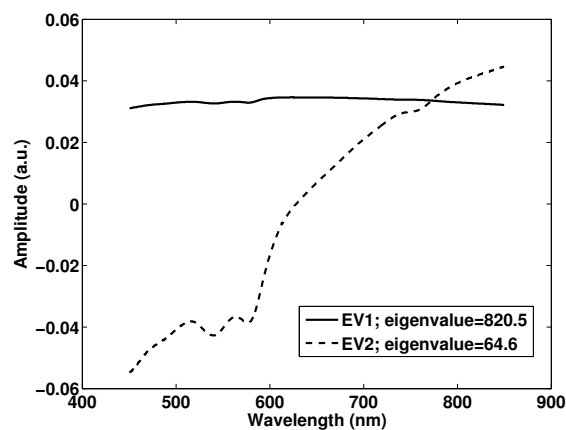
Figure 3.14: Eigenvectors and corresponding eigenvalues of the PCA.

Logistic regression

Encouraged by the visual separation of the two tissue classes in the PCA analysis above, logistic regression was employed to develop a model that would automatically classify blood and non-blood tissue spectra. Logistic regression seeks to calculate the parameters (feature weights) of a linear boundary (a n-1 dimensional hyperplane that separates two regions between the n-dimensional sample space) that best separates the two classes. To achieve this, a probabilistic model is defined using the logistic

function. Let x be a sample and y be its respective class represented by a value in $\{0, 1\}$, then the probability of a sample belonging to class 1 is defined as[4]:

$$P(y = 1|x) = \frac{1}{1 + e^{-\theta^T x}} \tag{3.7}$$

where θ are the feature weights to estimate.

The goal is to fit this model by finding the optimal parameters θ that maximizes the likelihood function $L(\theta)$ of the training data $x^{(1)}, \ldots, x^{(m)}$ with classes $y^{(1)}, \ldots, y^{(m)}$:

$$L(\theta) = \prod_{i=1}^{m} P(y = y^{(i)}|x^{(i)}) \tag{3.8}$$

This optimization is usually performed using a gradient descent on the log-likelihood (logarithm of the likelihood) function $l(\theta)$:

$$l(\theta) = \sum_{i=1}^{m} \log[P(y = y^{(i)}|x^{(i)})] \tag{3.9}$$

Since the number of wavelengths measured for each sample (n=892) was larger than the number of samples (m=173), a straightforward application of logistic regression would be prone to overfitting. To avoid over-fitting, two separate strategies were employed. First, since many of the 892 wavelengths measured in each sample spectrum were assumed to be highly correlated across samples (for example, wavelengths falling within short contiguous intervals, e.g., near an absorption peak, had similar values), only a subset of these wavelengths provided independent information of the sample. Feature selection was used to find the best subset of wavelengths for classification. In a second approach, regularization was used to reduce the effects of large number of features (wavelengths).

For feature selection, an information gain metric was used to score the predictive power of each wavelength for the blood and non-blood classes. The information gain score of wavelength W is given by:

$$InfoGain(class, W) = H(class) - H(class|W) \tag{3.10}$$

where $H(class)$ is the entropy (a measure of the uncertainty in a random variable),

---

[4]Note that $P(y = 0|x) = 1 - P(y = 1|x)$

and $H(class|W)$ the conditional entropy defined as:

$$H(class) = - \sum_{c \in class} P(c) \log P(c) \tag{3.11}$$

$$H(class|W) = - \sum_{c \in class} \sum_{w \in W} P(w, c) \log P(c|w) \tag{3.12}$$

For the second strategy, a regularization of the logistic likelihood function using all wavelengths was used to mitigate over-fitting and reduce model complexity. Regularisation strategies add penalties to the likelihood function that select against complex models. For example, common regularization techniques for linear regression include adding a negative term to the least squares likelihood that depends on the magnitude of the regression coefficients: the larger the coefficients, the larger the penalty and the less likely they will be chosen as a solution. In our logistic classifier, we use a common regularization term adding a penalty to the log-likelihood function:

$$l_{reg}(\theta) = \sum_{i=1}^{m} \log[P(y = y^{(i)}|x^{(i)})] - \lambda \sum_{j=1}^{n} (\theta_j)^2 \tag{3.13}$$

where λ is the regularisation parameter.

Algorithm evaluation

Logistic regression was implemented in the software Weka [Hall et al., 2009] (version 3.6.8) from the University of Waikato. The F-score, accuracy and cross-validation error were used to evaluate the algorithm.

The F-score F and accuracy of the classification are defined as:

$$F = \frac{2T_P}{2T_P + F_N + F_P}; \qquad Accuracy = \frac{T_P + T_N}{T_P + F_P + T_N + F_N} \tag{3.14}$$

where T_P is the number of true positives, F_P is the number of false positives, T_N is the number of true negatives, and F_N is the number of false negatives obtained during the classification.

The cross-validation root mean squared error, is the error over a subset of instances m_{CV} as obtained by:

$$RMSE_{CV} = \sqrt{\frac{\sum_{i=1}^{m_{CV}} (h_\theta(x^{(i)}) - y^{(i)})^2}{m_{CV}}} \qquad (3.15)$$

where $h_\theta(x^{(i)})$ and $y^{(i)}$ are the ith predicted and actual values respectively.

3.3.2 Results

Pictures of some of the samples taken for each of the tissues inspected are shown in Fig. 3.15 to Fig. 3.19, together with their corresponding mean spectrum, intensity and haemoglobin parameters. The black soft curve shows the mean spectrum of the 50 spectra taken at each location, with the standard deviation plotted as the green noisy curves.

Aside from the overall high reflectivity due to low haemoglobin content, spectral features from fat and skin were visually similar in most cases, which may likely be due to the high content of lipids in chicken skin. In the case of both tendons and muscles, the spectra presented evident increasing or decreasing tendencies. A hypothesis of this behaviour is that these organised tissues vary their scattering response depending on the cell's orientation with respect to the catheter surface.

As expected, the value of the haemoglobin parameter was higher when interrogating the blood vessels than in other tissues. Peaks at oxy-haemoglobin absorption wavelengths were present in most of the spectra, even for those of low haemoglobin parameter. For the vessel shown in 3.15 A, a high haemoglobin parameter and low intensity was consistent with the size of a vessel larger than the tip of the catheter, and the peak at 757 nm was highly pronounced indicating the presence of deoxy-haemoglobin.

The artefact at 733 nm was also present during the acquisition; however, this peak was not as pronounced as in the previous experiment. The positioning of the fibre at certain locations such as within the fibrous tissue was imprecise due to the slippery surface; therefore it is possible that the tip of the catheter was not in total contact with the tissue. There were no negative regions in any of the spectra.
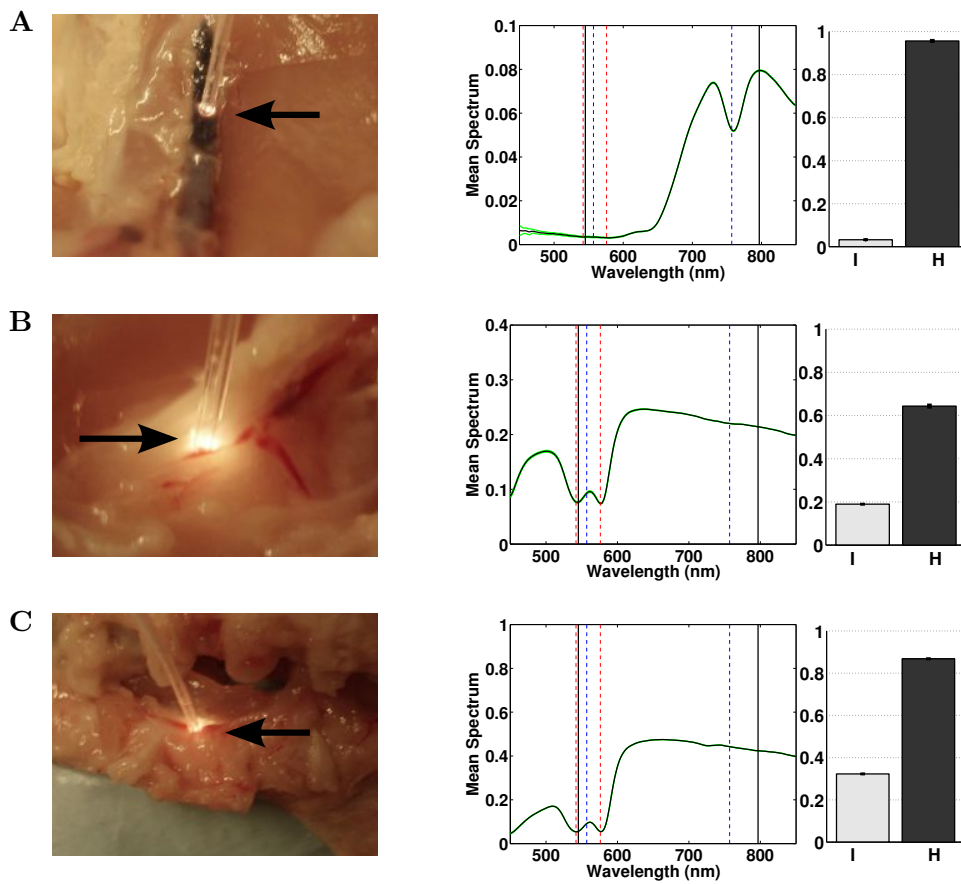
Figure 3.15: Placement of the catheter tip in blood-related tissues. To the right of each figure is the acquired spectrum acquired and its respective intensity and haemoglobin parameter.
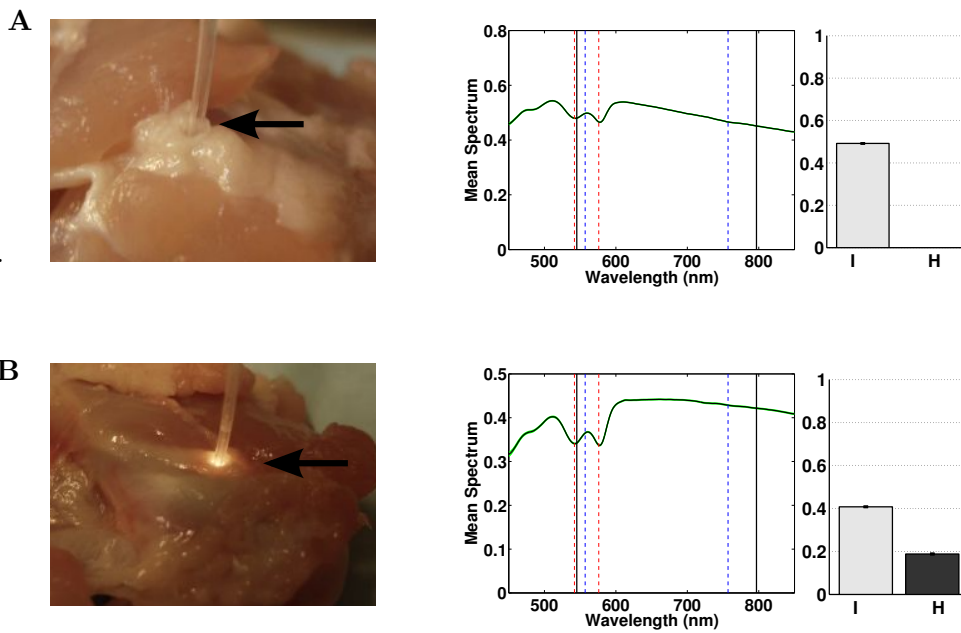
Figure 3.16: Placement of the catheter tip in fat. To the right of each figure is the acquired spectrum acquired and its respective intensity and haemoglobin parameter.
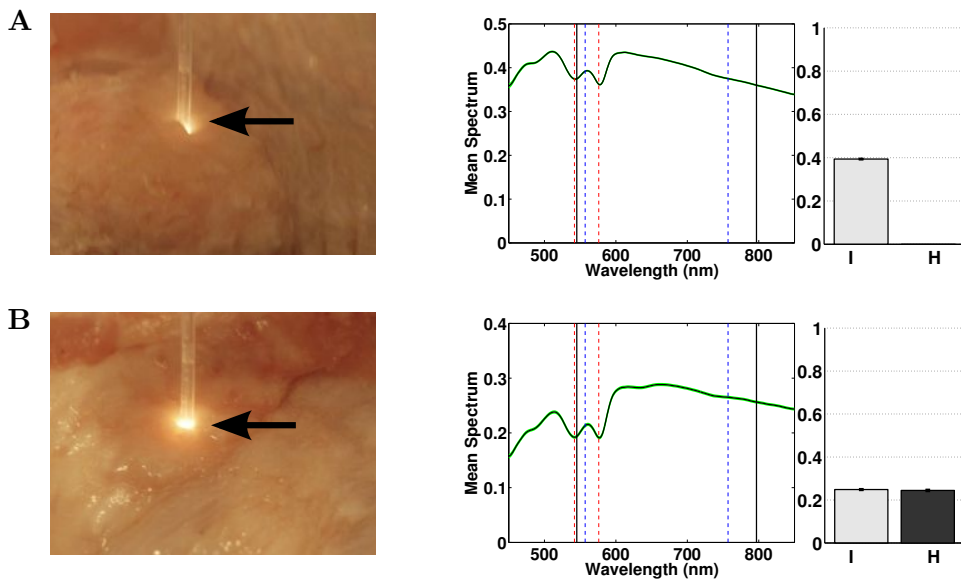
Figure 3.17: Placement of the catheter tip in the chicken skin. To the right of each figure is the acquired spectrum acquired and its respective intensity and haemoglobin parameter.
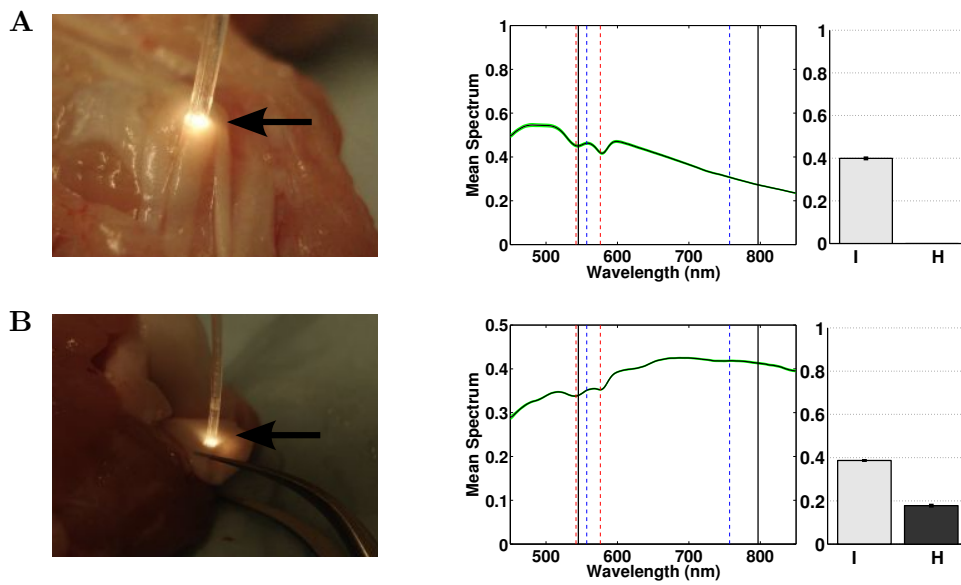
Figure 3.18: Placement of the catheter tip in tendons. To the right of each figure is the acquired spectrum acquired and its respective intensity and haemoglobin parameter.
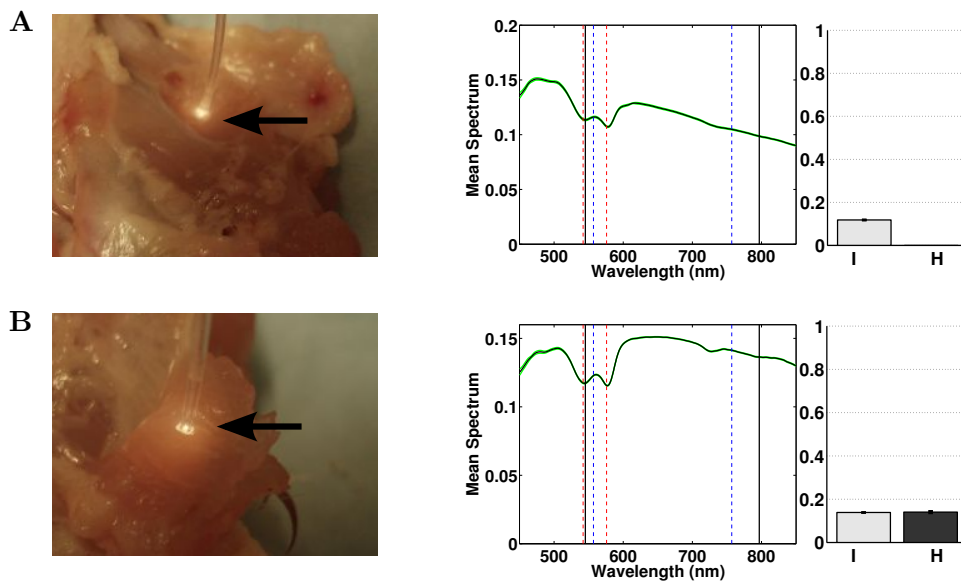
Figure 3.19: Placement of the catheter tip in muscles. To the right of each figure is the acquired spectrum acquired and its respective intensity and haemoglobin parameter

Since this work focuses in blood detection, spectrum values at wavelengths below 850 nm seemed enough to detect haemoglobin absorption. It might also seem tempting to use the transmission peak at 945 nm shown in Fig. 3.4 to obtain information

about the presence of lipids; however, the fat absorption peak at 930 nm falls into a noisy region which might not carry useful information in all the acquired spectra (Fig. 3.20 dotted line at 930 nm). Future prototypes could be constructed with materials which transmit better at wavelengths were lipid absorption is present.
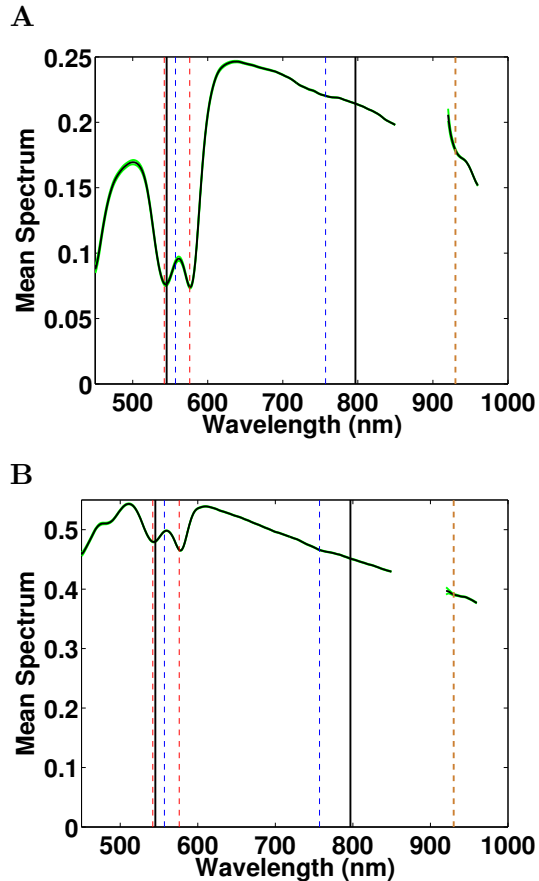
Figure 3.20: Extended spectra showing the wavelengths around the 945 nm transmission peak (Fig. 3.4) for the catheter placed in: **A** (Fig. 3.15) fat and, **B** blood (Fig. 3.16). Noise around transmission windows was excluded. The dotted line at 930 nm corresponds to a lipid absorption peak [Prahl].

The two previously mentioned alternatives to avoid overfitting were explored. The regularization parameter λ and the number of selected features were found in each case using 10 fold cross-validation, and selecting the values that led to the minimum error. Cross validation error plots are shown in Fig. 3.21. For the regularized algorithm (Fig. 3.21 A), the regularization parameter found to balance the results was $\lambda = 0.08$.
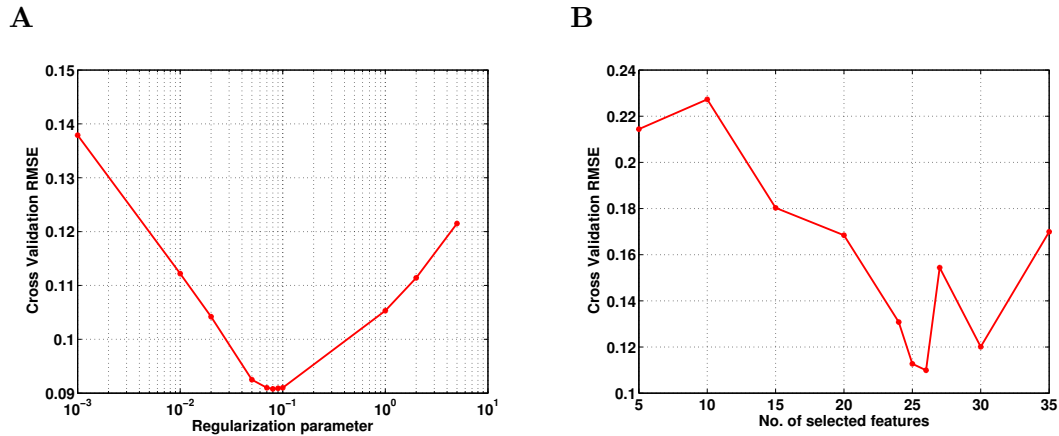
Figure 3.21: Cross validation error for **A**, regularized logistic regression under parameter λ; and for **B** logistic regression applied to a subset of selected wavelengths.

It can be noticed from Fig. 3.21 B, that for $n = 26$ features, a minimum cross validation error is achieved. The selected features in this case were: 451.24, 450.32, 451.7, 576.47, 577.37, 576.92, 543.77, 536.93 576.01, 544.22, 579.64, 546.04, 580.09, 578.28, 577.82, 579.18, 578.73, 541.49, 540.58, 541.03, 542.86, 543.31, 541.95 542.4, 538.3, and 537.39 nm. The selection of these wavelengths may be explained by being within a region for which the absorption by both oxy and deoxy-haemoglobin is strong (different blood oxygenation was not being considered).

The evaluation metrics for the three cases: logistic regression without regularization, regularized logistic regression, and logistic regression over the 26 wavelengths found in the feature selection, are shown in Table 3.3.

Table 3.3: Classification scores for logistic regression

	Accuracy	$RMSE_{CV}$	F-score
All data (no regularization)	98.27 %	0.1285	0.961
Regularization: $\lambda = 0.08$	98.84 %	0.0908	0.974
Feature Selection: $n = 57$	98.84 %	0.1099	0.974

While encouraging, these results are still preliminary. For future work, a larger sample set of spectra from tissues more similar to those found in the epidural space would be needed for the further exploration of the utility of this automated tissue classification framework.

3.4   Discussion

In this chapter, an optical epidural catheter with integrated light guides was proposed to reduce the risk of intravascular injection during epidural anaesthesia. The catheter used in this study had four light guides but only two were used in this pilot study. Reflectance measurements with different source-detector distances could be performed with additional light guides, which would have the potential advantage of performing spectroscopic sensing at different tissue depths [Arifler et al., 2006; Utzinger and Richards-Kortum, 2003]. For the geometry of the light guides, the source-detector separation was 644 µm. The resulting average maximum depth in the fat and blood tissue simulations was consistent with those obtained by Arifler et al. [Arifler et al., 2006].

The haemoglobin and intensity parameters facilitated comparisons between spectra. An important benefit of these parameters is that they can be related in a straightforward manner to visual features in the spectra. A limitation is that they are not directly related to chromophore concentrations or to morphological features of tissue. Indeed, they can be confounded by the presence of additional tissue chromophores such as beta-carotene, and by variations in the wavelength dependence of optical scattering. To estimate the concentrations of oxy- and deoxy-haemoglobin in tissue, it may be important to account for multiple factors such as the aggregation and flow of erythrocytes, and the concentrations of plasma constituents such as bilirubin and platelets [Meinke et al., 2007].

The measurements acquired from the epidural region of the swine with the optical catheter during the laminectomy demonstrated that there were prominent differences in the optical reflectance spectra acquired from blood and from adjacent tissues. This finding is clinically significant, as it highlights the potential of optical reflectance spectroscopy to provide catheter guidance and to detect intravascular catheter tip placement in particular.

With measurements limited to one cadaveric specimen, the observed differences in the acquired spectra and the corresponding haemoglobin and intensity parameters provide only an initial indication of the variability of the spectra. Follow-up studies performed in multiple subjects in vivo are required to determine optimal thresholds for the haemoglobin and intensity parameters and to estimate the sensitivity and specificity with which detection can be performed. In an in vivo context, several factors could influence the optical reflectance spectra, including tissue heterogeneity, variable amounts of beta-carotene in the epidural fat [Reina et al., 2006], and

variations in the pressure imparted by the catheter on tissues. The volume of saline that is injected by the Tuohy needle as part of the loss-of-resistance test used to detect the epidural space, which may affect the delivery and collection of light at the optical catheter tip, is variable. Follow-up studies are required to determine differences between optical reflectance spectra acquired with the catheter tip within an epidural vein and adjacent to the outer surface.

As an alternative to the construction of a deterministic model based on specific chromophores absorption, a statistical approach based on classification algorithms was proposed to be used in larger data sets. A series of acquisitions were performed in ex-vivo chicken tissue to assess the viability of this approach.

Measurements from the catheter in contact with blood vessels of various diameters were possible in this set of experiments. In this case, the results also showed significant differences between the haemoglobin parameter from blood-rich tissues, and non-blood tissues. Spectra from other regions such as skin, muscle and fibrous tissue exhibited a very low haemoglobin parameter.

From the PCA, the data set appeared to be linearly separable for the two classes: blood and non-blood related tissues. Logistic regression showed good performance during the test with F-scores over 0.9. These results are encouraging for the further exploration of this method to detect the proximity of vascularity to the tip of the catheter. Proper assessment and optimization of the techniques would be feasible with data from the epidural space and adjacent regions. The acquisition of a larger set of data would allow for a more robust classification that could also include predictions of oxygenation levels.

On the other hand, the materials used for construction of this catheter prototype had several limitations. As a material to construct the catheter body, polystyrene had the advantage that it could readily be removed with cyclohexane to expose the optical light guides. However, its use resulted in a catheter that was more rigid than those available commercially, and the optical catheter in this study broke for bending radii in the range of 1.5 to 2 cm. These mechanical characteristics are incompatible with clinical practice. Future versions of the catheter could be developed with more flexible materials such as a medical grade polycarbonate such as Zelux GS (David Welker, Paradigm Optics, personal communication). Second, the PMMA light guides had prominent absorption peaks in the visible range and the very low transmission made them impractical for wavelengths greater than 1000 nm. Prominent absorption features at 1210 nm associated with the presence of lipids were

previously shown to be relevant for guiding a spinal needle into the epidural space [Desjardins et al., 2011] and it is likely that they could be advantageous for catheter guidance as well. The limitations of PMMA could potentially be overcome with certain perfluorinated plastic optical fibres that allow for transmission at wavelengths up to 1300 nm [White]. Along the translational path, maintaining low fabrication costs will be an important consideration, as catheters are disposable products in current clinical practice.

Modifications to fibre coupling are required in order to make the optical catheter compatible with current clinical practice. Typically, a Tuohy needle is withdrawn over the entire length of the catheter after the catheter has been inserted. This procedure could not be performed if conventional optical fibre connectors are present at proximal ends of the light guides; the connectors are too bulky to fit within the needle. In future versions of the optical catheter, this problem could be solved by performing light coupling into the light guides without optical fibre connectors, using optical side ports in the body of the catheter.

A possible prototype using this principle is shown in Fig. 3.22 and 3.23 for a configuration with two equidistant optical guides. Figure 3.22 shows the first stages the catheter would undergo for the contactless connection. First, the optical guides need to be exposed, and the exposed surface of the remaining fibre in direction towards the catheter feeding must be covered with an absorber (**a**, in the figure) to avoid undesired reflections.
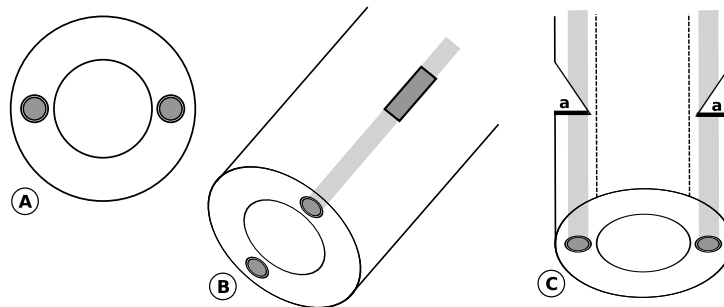
Figure 3.22: Possible connections for a prototype with two optical guides. **A** Tip's surface showing the two guides with the same dimensions as those use in this work. **B** Removal of material from the catheter to expose the optical guide. **C** Cut optical guide with an angle to let the light come from and towards the catheter; cover the other exposed surface of the guide with an absorbent material (a) to avoid any reflection.

After this, the catheter would require to be re-coated at the areas where the

fibre has been exposed (f in Fig. 3.23). Since this path will be use for light to travel out and into the fibre, the coat must use a matched index material (matched with fibre's refractive index) to achieve minimum loss. This design would be able to be withdrawn as any commercial catheter (and effectively look like a commercial catheter). The difficulty in this case would be the construction of catheter holder, and aligning methodology to be able to focus the light into the small window, and collect it in a similar way.
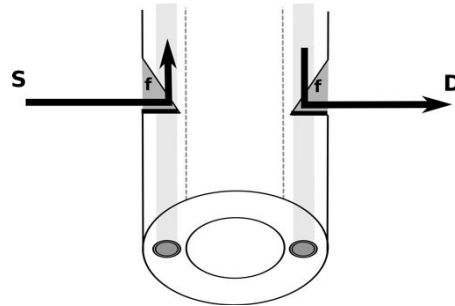
Figure 3.23: The space could then be filled with an index matching material (f). This catheter then could be mounted in an specifically designed structure that could focus the light to the source guide (S), and collect it from the detection guide (D).

Also in future version, the distal end might be modified. In many commercial catheters, fluids are released through multiple holes that extend from the lumen to the side wall, with the distal end face sealed. This feature is not present in all catheters, with some commercial catheters having a central lumen like the one shown here for the optical catheter [Pajunk], however the need of these lateral-eyed catheters need to be addressed. To allow for optical reflectance measurements to be acquired from the distal end, the holes will need to be positioned carefully to avoid intersections with the light guides. The light guides could be modified so that light is directed to the side wall, perpendicular to the long axis of the catheter, to allow for sensing in the specific regions where fluids are released.

Chapter 4

Multispectral photoacoustic imaging of blood

In the previous chapter, reflectance spectroscopy was employed for the continuous monitoring of the immediate environment of an epidural catheter. The same technique was used to differentiate between venous and arterial blood using a double clad fibre. Reflectance spectroscopy offered a simple method incorporated into a small size device for the detection of risky structures. However reflectance spectroscopy can only interrogate tissues near the optical fibres used for illumination and detection. There are medical situations where the detection of risky structures is needed sooner.

For instance, peripheral nerve block is a technique used for anaesthesia, analgesia, and for the treatment of pain [Miller and Pardo Jr., 2011]. During this procedure a drug is deposited in the proximity of a nerve (between the nerve's outermost layer and the tissue surrounding it). Figure 4.1 shows an example of an ultrasound guided femoral nerve block [Brown, 2010]. It is common to perform nerve blocks with ultrasound guidance, however there are cases for which needle visualisation can be misleading due to its relative position to the transducer, so that the insertion angle of the needle causes the acoustic wave to be reflected in a direction out of the scope of the ultrasound detector [Sites et al., 2012]. There are also cases for which the pressure by the ultrasound transducer collapses a vessel making it not visible [Robards et al., 2008]. A study on orthopaedic patients showed a 5% incidence of vascular puncture [Wiegel et al., 2007]. Local anaesthetic systemic toxicity caused by injecting anaesthetic into a blood vessel, is a risk that can carry dangerous con-

sequences such as seizures and cardiac arrest [Mulroy, 2002]. Another complication derived from a vascular puncture during peripheral block nerves is the formation of haematoma that can damage the nerve by the restriction of a blood supply (pressure ischemia) [Wiegel et al., 2007]. Therefore, the detection of a proximal blood vessel well in advance to the needle puncture is desirable.
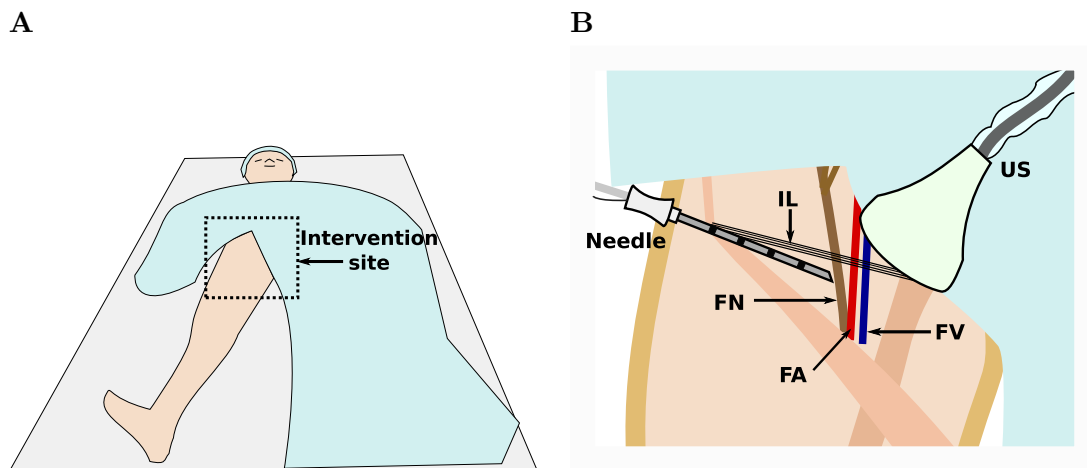
Figure 4.1: Femoral nerve block. **A** Intervention site; **B** Ultrasound guided intervention. FN: femoral nerve; FA: femoral artery; FV: femoral vein; IL: inguinal ligament; US: ultrasound probe.

In this context, photoacoustic techniques have been explored as an alternative complementary tool to ultrasound in order to overcome the loss of visibility due to acoustic reflections and the presence of other artefacts such as bouncing echoes and speckle. As mentioned in Section 1.3.2, another advantage of using PA techniques is that they can also overcome the limited spatial resolution of pure optical methods. Researchers have been able to image structures more than 2 cm into tissue for investigations on needle visualization and target identification [Kim et al., 2010, 2011]. Photoacoustic imaging of the needle is possible due to the high absorption coefficient of its stainless steel constituents [Su et al., 2010].

Photoacoustic imaging, basically requires illumination of the tissue of interest, and then collection of the acoustic response. While in the works of Su et. al. and Kim et. al. [Su et al., 2010, 2011; Kim et al., 2010, 2011] a light source fixed to the ultrasound transducer illuminates the tissue from the surface, Piras and co-workers [Piras et al., 2013] performed photoacoustic imaging with illumination coming from an optical fibre placed within the needle. In this case, the tip of the needle could still generate a photoacoustic signal while illuminating the target tissue.

One advantage of illuminating the tissue from the needle is the simplicity of the illumination system that does not hinder the manipulation of the detection probe. However, this illumination also causes variation in the detected photoacoustic signal while the needle is approaching the target tissue. This variation depends not only on the properties of the target but also on the properties of its surroundings which affects the light distribution reaching the interrogated volume.

In this chapter, empirical investigation of the proximity of the fibre to a blood-vessel-like structure in terms of the detected photoacoustic signal is presented. A multispectral analysis is performed to obtain an insight into the effects of different wavelengths for a given chromophore. Two targets were interrogated. The first was a tubing containing India ink immersed in a low concentrated solution of scatterers. This target was used to get an approximate range of fibre-tubing distances to interrogate. The second target consisted of a tubing containing a RBC solution, in this case the tubing was immersed in a tissue-like scattering medium ($\mu'_s = 1$).

4.1 Multispectral photoacoustic system

Regional anaesthesia equipment vary between procedures. For instance, for US imaging of the axillary and upper extremity regions, US probe frequencies of 10-15 MHz are commonly used, although lower frequencies are preferred in infraclavicular and gluteal regions [Marhofer and Chan, 2007]. On the other hand, the needles used for peripheral block nerves are commonly 20 gauge (908/603 µm, OD/ID) to 22 gauge (718/413 µm, OD/ID), or 17 gauge (1.47/1.07 mm, OD/ID) to 19 gauge (1.07/0.69 mm, OD/ID) if a catheter is to be used [Nima-Shariat et al., 2013]. With this in mind an US/PA array transducer built into a US clinical-style imaging probe was used here as an acoustic detector, this probe would add no further complexity to the already existent maneuvers. The aim of this work then, is to have a procedure in which the familiar US image is presented with more information regarding tissue identification (in this case, the presence of blood).

4.1.1 Setup specifications

Figure 4.2 shows the schematic of the setup used in these experiments. An optical parametric oscillator (VersaScan L-532, GWU-Lasertechnik) was used as the light source for the photoacoustic (PA) signal. The oscillator (OPO) was pumped by a

frequency-doubled Q-switched Nd-YAG laser at 532 nm (Quanta-Ray INDI-40-10, Spectra-Physics), with 10 Hz repetition rate, and 6 ns pulse width.

Two beams are generated at the OPO: the "signal" with wavelengths from 700 to 1000 nm and the "idler" with wavelengths from 1100 to 2200 nm. These beams are separately coupled to silica-silica multimode optical fibres (FG910LEC, Thorlabs) with a core diameter of 910 µm, and a coating diameter of 1035 µm. Experiments for the imaging of haemoglobin here, were performed using only the signal beam. Although this fibre can still be fitted into a 17 gauge needle, further experimentation may try to employ smaller diameters to improve the versatility of the method.

The samples for the experiments were contained in a THV-500 tubing with 2.80 mm inner diameter and 3.15 mm outer diameter (Paradigm Optics, Washington, USA) placed in a tank filled with a solution of intralipid. An acoustic polyurethane absorber (AptFlex F28, Precision Acoustics, Dorchester, UK) was placed at the bottom of the tank to reduce acoustic reflections. The fibre was cleaved, polished, and placed directly within the tank, with an angle of $30\,^{\circ}$ to the surface.
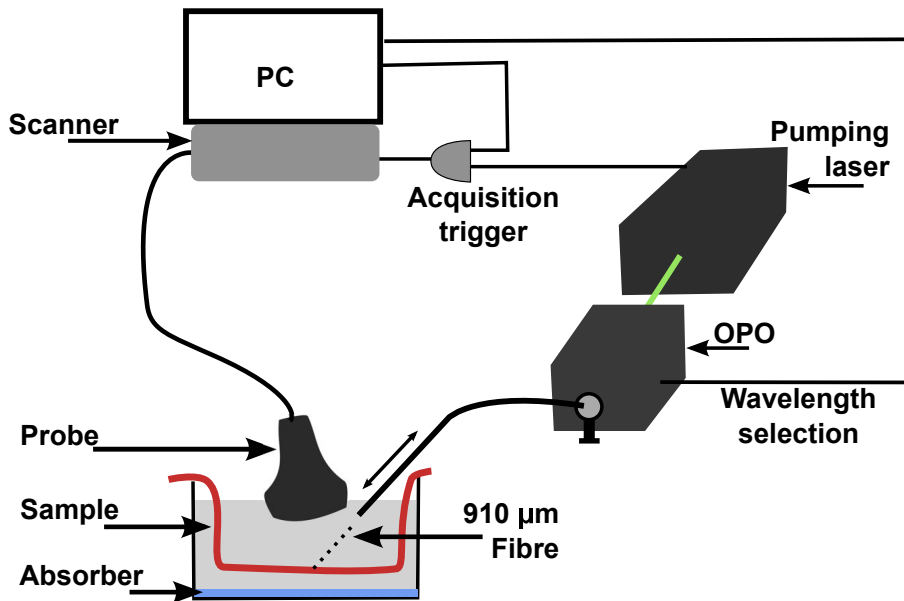
Figure 4.2: Experimental setup. The OPO deliver light to the sample. The acoustic signal is detected with the ultrasound transducer and acquired by synchronization with the laser.

Acquisition and display of the PA signal was performed by a dedicated software and hardware (imaging probe, scan, and PC) for data acquisition, beam-forming and image generation (UltraVision Research Platform, Winprobe, Florida, USA).

The detector consisted of a linear array of 128 ultrasound transducer elements with a nominal bandwidth of 5 to 14 MHz. The PA acquisition at the scanner was triggered by the output of an AND gate whose input was a pulse generated by the PC, and a timing pulse synchronous with the Q-switching of the laser. This trigger had the purpose of waiting for the wavelength change at the OPO, and controlling the acquisition rate. Wavelength change was achieved by the motorised rotation of the OPO crystal. A B-mode ultrasound (US) signal was acquired immediately after the PA signal acquisition.

The ultrasound scanner processed the data generating an US image of the target in real time with an overlay of the PA response. Time gain compensation (TGC) was use to compensate for the different depths at which the sample was being interrogated. The TGC was manually adjusted to amplify the signal at the portion of irradiated tubing while trying to keep low noise levels. Once adjusted, the TGC parameters remained the same for all acquisitions in the experimental session. The envelopes of the radio frequency waves were then saved (see Appendix B) for their posterior analysis. A set of acquisitions was obtained for different wavelengths within the range of 700 nm to 900 nm.

4.1.2 Data analysis

For each experiment presented here, a set of frames acquisitions ($k = 15$ or 30 frames) were obtained from a specific sample setting and given wavelength. An experimental session corresponds to a series of experiments $Frame_k^i(\lambda_j)$ for a varying position i of the fibre (light source), and wavelength λ_j in the range from 700 nm to 900 nm.

A region of interest (ROI_{PA}) for each of the stored PA frames ($Frame_k^i(\lambda_j)$), was defined in the corresponding irradiated area within the tubing. Additionally a second region, ROI_{noise}, with approximately the same area as ROI_{PA} was defined where no PA signal was expected due to the absence of strong chromophores. This ROI_{noise} was used for filtering the data so that "empty" frames for which the mean value at ROI_{PA} ($\mu_k^i(\lambda_j)$,) were below the threshold defined in Eq. 4.1, were discarded.

$$threshold_{k\ noise}^i(\lambda_j) = \mu_{k\ noise}^i(\lambda_j) + \sigma_{k\ noise}^i(\lambda_j) \qquad (4.1)$$

where $\mu_{k\ noise}^i(\lambda_j)$ and $\sigma_{k\ noise}^i(\lambda_j)$ are the mean and standard deviation for values at ROI_{noise} (from frame $Frame_k^i(\lambda_j)$).

An image was obtained from the frame to help define the regions of interest. The

ROI_{noise} region was chosen to be as close as possible to the ROI_{PA}, however it may not reflect the actual noise at ROI_{PA} depth due to differences in signal attenuation. Thus the ROI_{noise} placed above the irradiated region is underestimating the noise values in the deeper ROI_{PA}.

Once the empty frames were filtered, a corrected value $\mu^i_{k\ corr}(\lambda_j)$, from the light source power at different wavelengths (and a specific fibre position) was obtained for the remaining mean values by:

$$\mu^i_{k\ corr}(\lambda_j) = \frac{\mu^i_k(\lambda_j)}{P_{signal}(\lambda_j)} \tag{4.2}$$

where the power P_{signal} was measured with a Vector H410 power meter (Scientech, Boulder, CO) from the distal end of the fibre. $P_{signal}(\lambda_j) = E \times PRR$, is the average power at the output of the fibre at wavelength λ_j for the pulse energy E and repetition rate PRR of the light pulse.

Following, the median of each set (of k frames) of mean values for a specific wavelength and fibre position was evaluated together with the median absolute deviation (MAD). These statistics was chosen due to its robustness given the observed variability of the PA signal among frames. A curve with the values of the median at each wavelength and the corresponding MAD error was plotted for each position of the fibre. Figure 4.3 shows the sequential steps in the processing for a given fibre position [1].

---

[1] Here, the wavelength file is saved by a LabVIEW code that controls the wavelength selection.
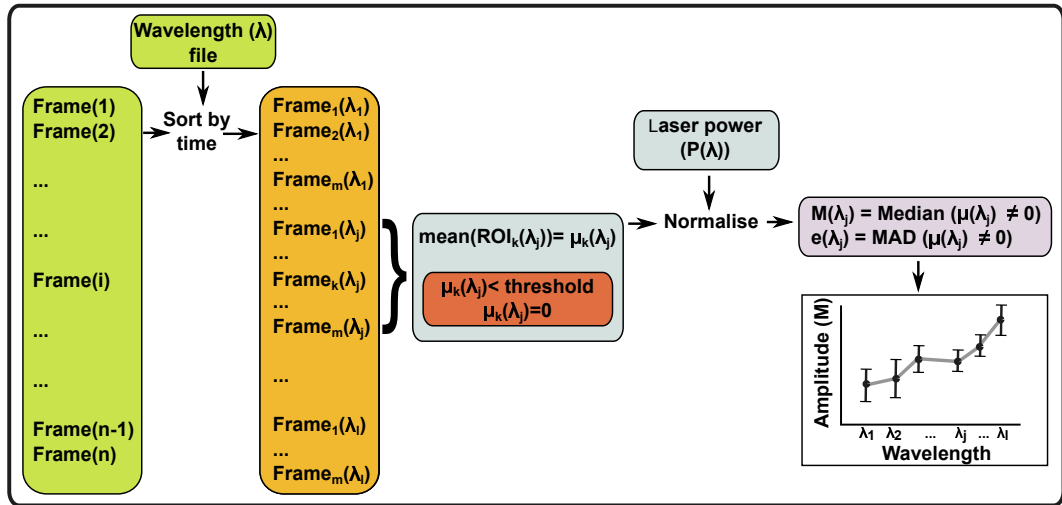
Figure 4.3: Initial frames from the scanner are assigned to a wavelength using a time file. The mean value in a ROI is obtained for each frame. The mean values are then filtered and normalised, after which the median and the median absolute deviation are calculated.

4.2   Monte Carlo simulations

Experiments were performed on two samples: diluted India ink, and RBC solutions. These samples were contained in a THV tubing immersed in an intralipid solution. PA and US images of the tubing were obtained at different distances from the fibre. This section presents a series of MC simulations performed to better understand the combined effect of the intralipid and the sample optical properties, over the absorption taking place at the sample.

4.2.1   Geometry

To speed up the simulation, the geometry used makes a rough approximation: only two layers are defined, and reflections at the boundaries are not being considered. The first layer corresponds to the properties of intralipid, while the second layer is set for the parameters of the sample (either oxygenated blood or diluted India ink). Photons are launched from a 910 µm diameter source with a numerical aperture of 0.22. Photon detection is performed by storing the weight lost by the photon packet in a region of $1 \times 1 \times 1$ mm located at the beginning of the second layer and aligned with the source (see Fig. 4.4).
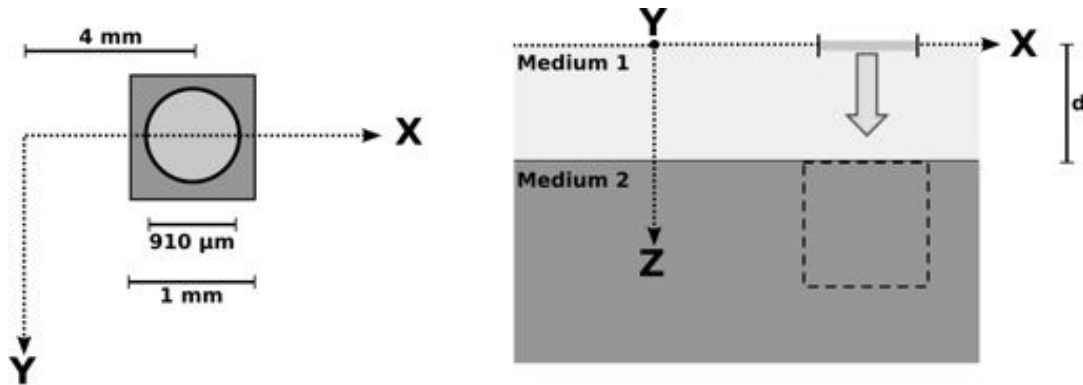
Figure 4.4: Geometry used for the simulation. The detection region is a volume of $1 \times 1 \times 1$ mm.

4.2.2 Optical properties

The absorption coefficient and reduced scattering coefficient of intralipid [Michels et al., 2008] are shown in Fig. 4.5 for a concentration of 1%. It can be noted that intralipid follows the absorption of water at wavelengths between 700 nm and 900 nm. In this case scattering in the medium is 100 fold larger than absorption.
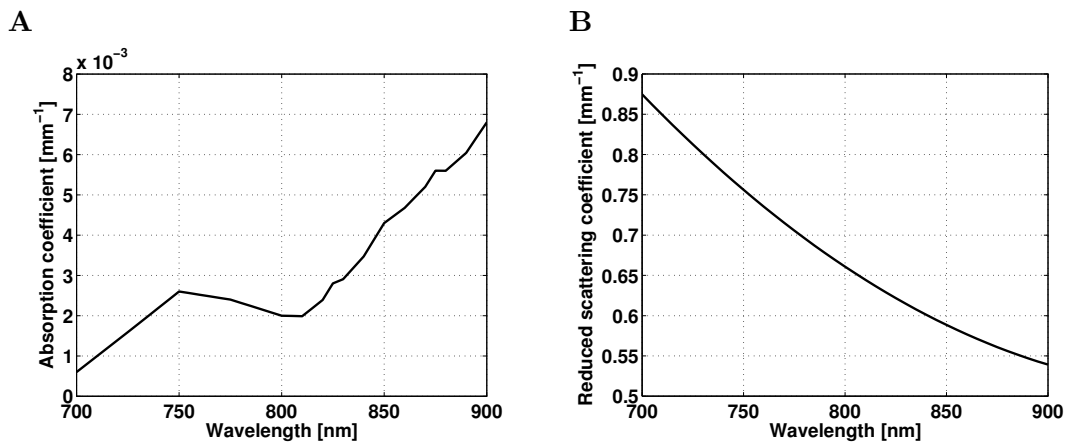
Figure 4.5: Optical properties of intralipid 1%: **A**, absorption coefficient (data from [Prahl] for the absorption of water); and **B**, reduced scattering coefficient (approximated data from [Michels et al., 2008]).

The absorption of India ink (Higgins, Chartpak Inc; Leeds, MA) was measured using a white source (HL-2000-FHSA, Ocean Optics) and a 2 mm glass cuvette for a concentration of 0.01 % V/V. The transmission of deionised water was also measured for reference. The resulting absorption coefficient of ink is shown in Fig. 4.6 A. The

reduced scattering coefficient of ink is shown in Fig. 4.6 with data from [Madsen et al., 1992].

A

B
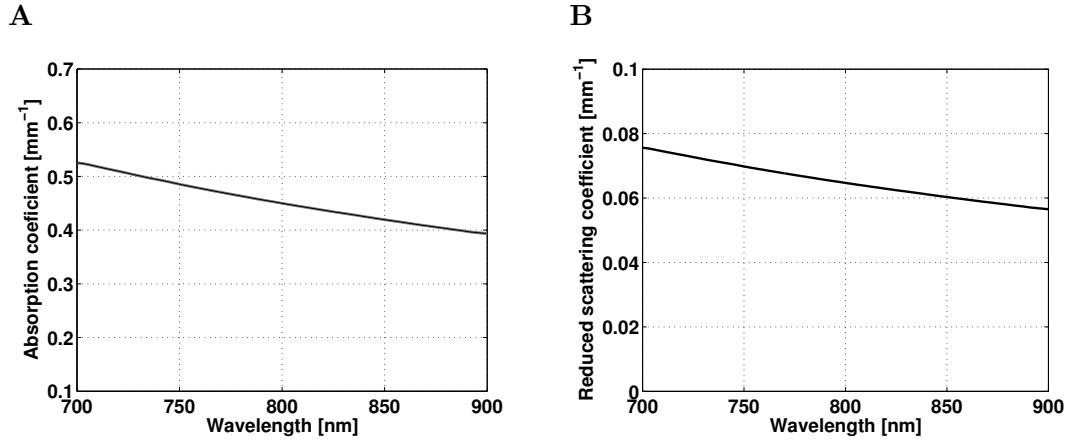
Figure 4.6: Optical properties of India ink: **A**, absorption coefficient (measured); and **B**, reduced scattering coefficient (data from [Madsen et al., 1992]).

Blood absorption was specified by the absorption coefficient of oxy-haemoglobin ($SO_2 = 100\%$) at a concentration of 15 g/dL (Fig. 4.7). The scattering of blood was considered as constant over the wavelength range with a value of $\mu'_s = 2.25 \ mm^{-1}$.
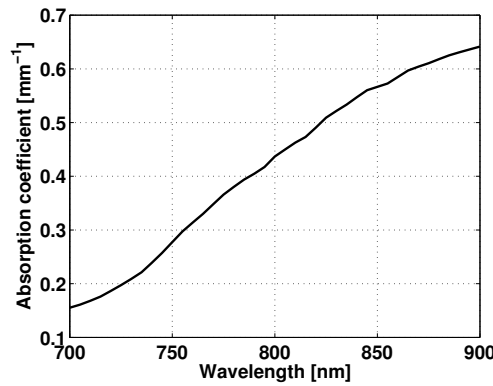
Figure 4.7: Absorption coefficient of oxy-haemoglobin (data from [Prahl]).

4.2.3 MC analysis

Three cases were simulated as shown in Table 4.1, where d is the thickness of the first layer (see Fig. 4.4). A total of 7×10^5 photons were launched for each of the simulations at wavelengths from 700 nm to 900 nm every 40 nm. The results are

shown in Fig. 4.8.

A

B

C

D
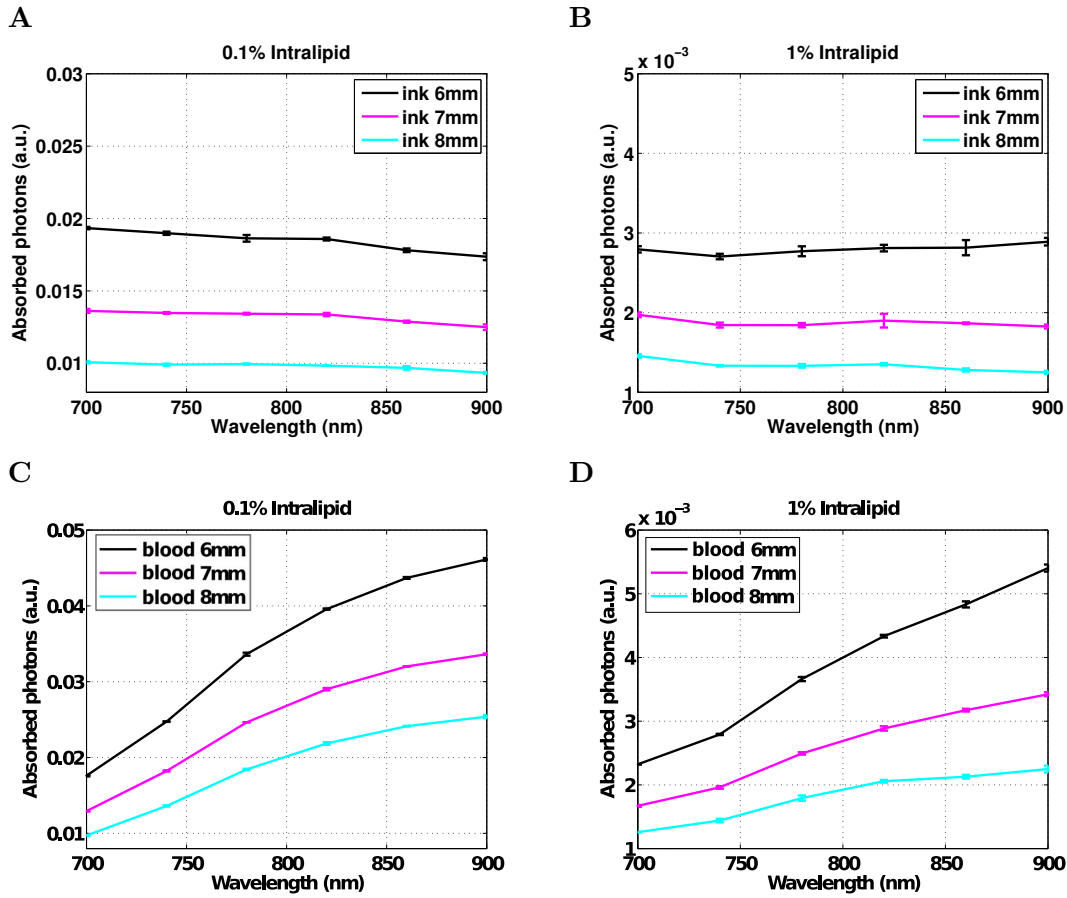
Figure 4.8: Photons detected at the sample, according to MC simulations for the samples **A**, **B**, **C**, and **D** described in Table 4.1.

Table 4.1: Simulated media used for the first and second layer

Sample	Layer 1	Layer 2	d (mm)
A	intralipid 0.1%	India ink	6, 7, 8
B	intralipid 1.0%	India ink	6, 7, 8
C	intralipid 0.1%	Oxygenated blood	6, 7, 8
D	intralipid 1.0%	Oxygenated blood	6, 7, 8

Figure 4.8 A shows a decrease in absorption with wavelength as expected from ink (see Fig.4.6 A). Analogously, for Fig. 4.8 C, absorption increases as anticipated from the haemoglobin absorption (see Fig. 4.7 A). For a higher concentration of intralipid, photons would reach shallower depths at lower wavelengths (Fig. 4.5).

Figure 4.8 B, shows how absorption increases with wavelength at 6 mm, which would correspond to an increase in light penetration, while at larger distances the curves tend to resemble the inverse of water absorption given that photons in the first layer had scatter enough to be absorbed by intralipid. This behaviour is not present in Fig. 4.8 D, due to the high scattering and absorption by blood.

4.3 Ink experiments

The first experiment was performed on the tubing filled with India ink, and immersed in intralipid. The ink was diluted with deionised water to a concentration of 0.01 % V/V to approximate the absorption of whole of blood with a haemoglobin concentration of 150 g Hb/L at wavelengths between 700 nm to 900 nm (see Fig. 4.6 A).

The diluted India ink was circulated by means of a peristaltic pump (Watson-Malow 502S at 10% of maximum revolutions) to prevent overheating of the tubing. This preventive measure was taken after noticing air bubbles being formed within the tubing when the ink was left still.
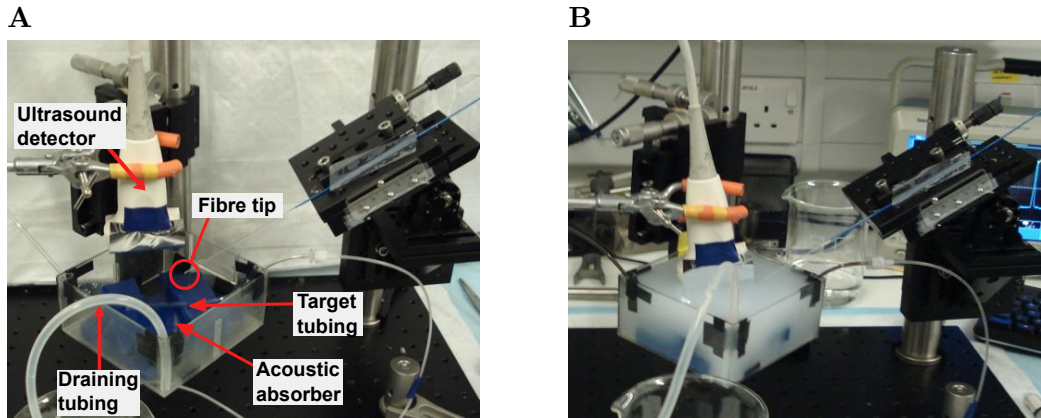
Figure 4.9: Filling of the tank with intralipid. Here the tubing contains diluted India ink.

For the experiments shown in this section, the tubing was surrounded by intralipid 0.1%. Although a higher concentration (intralipid 1%) has been used to mimic physiological properties, intralipid 0.1% was used in preliminary tests to find appropriate fibre-tubing distances to interrogate. The tank with the tubing can be seen in Fig. 4.9. Control measurements were performed with the tubing filled with

water, these acquisitions were done after the acquisitions with ink in the tubing since the PA signal from the ink was used to align the fibre with the tubing.

The signal from the OPO was attenuated before being coupled to the fibre with a metallic neutral filter 05 SN 25 with 32 % transmittance (Comar Optics). The distal end of the fibre was positioned at approximately 5 mm from the tubing at the beginning of the experiment. A series of 15 acquisitions were performed every 20 nm from 700 to 900 nm. This was repeated while moving away the fibre from the tubing by means of a translational stage.

4.3.1   Results

Two sets of experiments were performed with ink. In the first, the source power is slightly higher and the fibre is placed closer to the tubing.

Ink set A

Averaged power delivered by the fibre ranged from 21.1 mW to 38.8 mW as shown in Fig. 4.10 with the highest value measured at 720 nm. Here and in the following experiments, the power was measured at the end of the image acquisitions.
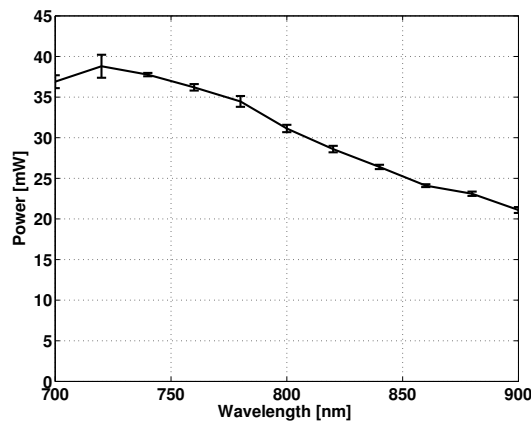
Figure 4.10: Power measured at the end of the optical fibre.

The US/PA images shown in this chapter were obtained from the frames after the processing mentioned in 4.1.2. Each set of frames obtained for a given distance was normalised by the maximum value of the PA signal within ROI_{PA} from the entire set comprising all wavelengths. These frames were then compressed and av-

eraged to show the final image with the corresponding superimposed ROI region. It is important to note that this last processing was performed only for the image presentation, the wavelength analysis of the PA information was made using the frames as obtained from 4.1.2. Figure 4.11 show averaged images from the frames at 800 nm for the tubing filled with ink.
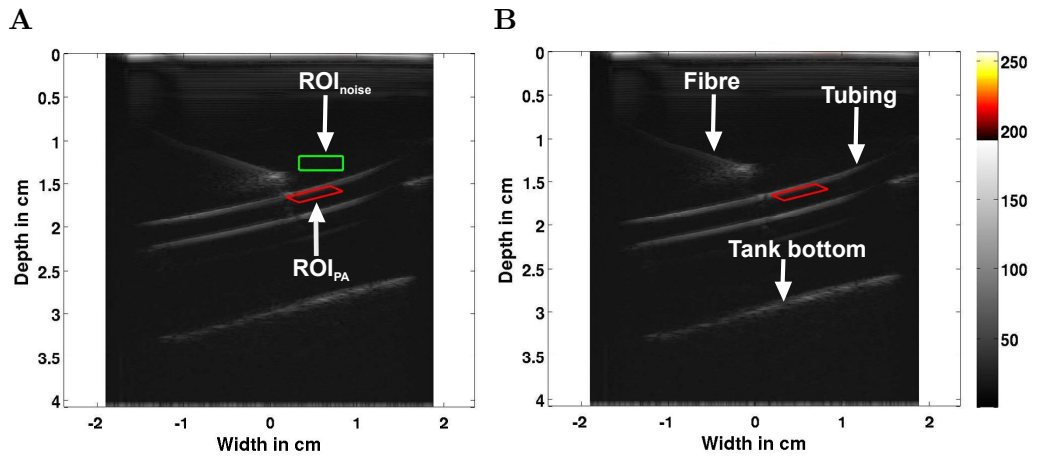
Figure 4.11: Composed PA and US image for the tubing filled with ink at: **A** 4 mm, **B** 6.5 mm. The tubing was immersed in intralipid 0.1%.

Each image is the composition of the US and the PA image at the specified distance. The colour bar here, and in the rest of the figures, uses a 256 colour scale from which 64 values are used for the PA heat-map, and the rest are used to create a conventional grey-scale US image. Brighter colours in the PA signal represent higher intensities. The region enclosed in red corresponds to the ROI_{PA}, while the region enclosed in green (only shown in the first frame) is the region corresponding to ROI_{noise} for the image processing. The initial fibre-tubing distance was calculated from the US images, further distances were referred to this one from the measurements at the translational stage. Images were obtained at four distances: 4.0, 4.5, 5.5 and 6.5 mm. Figure 4.11 A and B show the composed US and PA images at 4 mm and the farthest at 6.5 mm respectively. There is no evident PA signal in the images in Fig. 4.11, which could be caused by the image normalization with a frame with a very high signal.

A
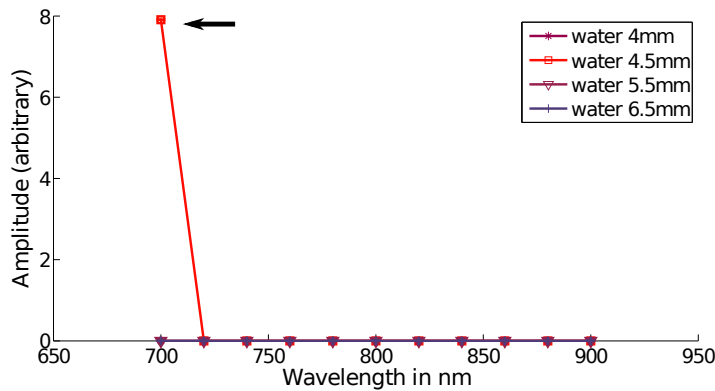
B
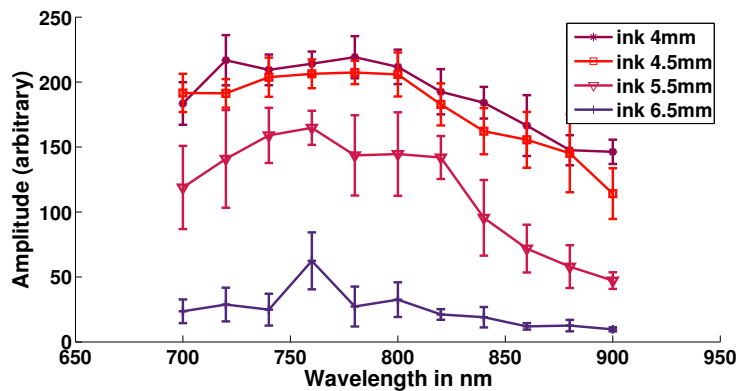
Figure 4.12: Photoacoustic signal from the tubing filled with: **A**, water and **B**, India ink with the tank surrounded by intralipid 0.1%. In the case of water, most of the PA signal fell under threshold levels, leaving just the point shown by the arrow.

Figure 4.12 shows the intensity of the processed signal within ROI_{PA} for the control experiment (Fig. 4.12 A), and ink (Fig. 4.12 B), against the wavelength of the excitation light. Each point of the plot corresponds to the median of the acquisitions remaining after the filtering, with the error bars showing the median absolute deviation.

Almost all the values within the ROI_{PA} for the control measurements were filtered, and no variation was observed while the fibre was moved away from the tubing. Large changes were observed with ink, where a decrease of the PA median with wavelength can be noticed at short distances. This decrease was expected given the ink absorption (see Fig. 4.6 A). However, low intensity at wavelengths under 750 nm (not present in the simulations) was evident in the results at 6.5 mm.

The action of the filter in the control measurements at 4.5 mm was analysed to determine the level of the signal prior to filtering and verify whether the frames were recorded. Figure 4.13 shows the mean PA value at ROI_{PA}, and ROI_{noise} together with the threshold level at each frame. The value noted in Fig. 4.12 A is pointed to by an arrow.
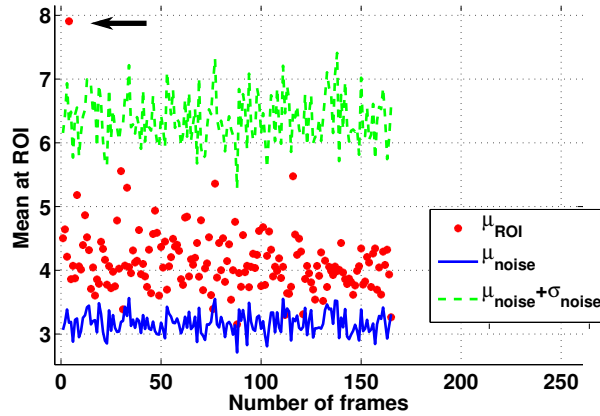
Figure 4.13: The mean PA value from all the frames at 4.5 mm and the tubing filled with water are shown in red dots. The green dashed line correspond to the threshold level. The only value that passes the threshold is pointed to by an arrow, and corresponds to the value shown in Fig. 4.12 A.

The photoacoustic intensity from ink against distance at 700, 800, and 900 nm is shown in Fig. 4.14 to analyse the evolution of the signal. The expected exponential decay after the absorption in ink is not observed in the curves, which may be sign of possible misalignment of the system, and errors in the fine adjustment of the distances in the translational stage where the fibre was mounted. As noticed from the highest amplitude at 800 nm and the lowest at 900 nm, the signal exhibits an intensity rise followed by a decay with wavelength instead of a monotonous decay from ink absorption (see Fig. 4.6 A).
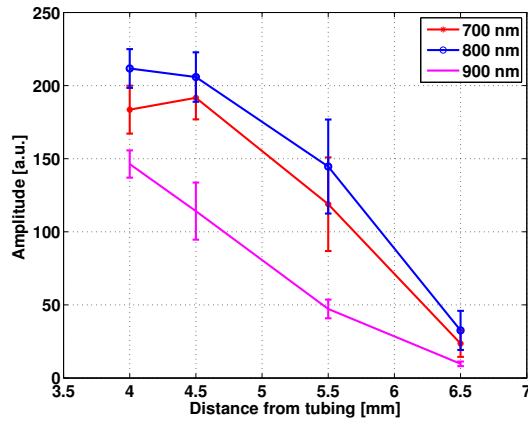
Figure 4.14: Variation of the photoacoustic signal from ink in the selected ROI at different distances.

Ink set B

Averaged power delivered by the fibre ranged from 19.8 mW to 34.9 mW as shown in Fig. 4.15 with the maximum amplitude around 720 -740 nm.
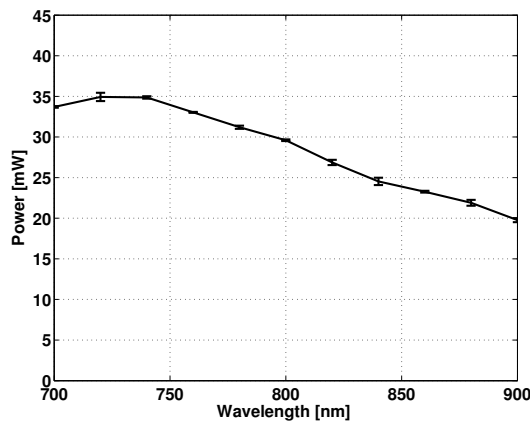
Figure 4.15: Power measured at the end of the optical fibre.

Figure 4.16 shows averaged images from the frames at 800 nm for the tubing filled with ink. The region enclosed in red corresponds to the ROI_{PA}, while the region enclosed in green is the region corresponding to ROI_{noise} in the image processing. Images were obtained at four distances: 6.0, 6.5, 7.0 and 8.0 mm. Figure 4.16 A and B show the composed US and PA images from the closest distance at 6.0 mm and the farthest at 8.0 mm. PA signal in the ROI_{PA} can be observed in both images, and the intensity within the ROI_{PA} for the fibre at 6 mm is visibly higher than that

at 8 mm.
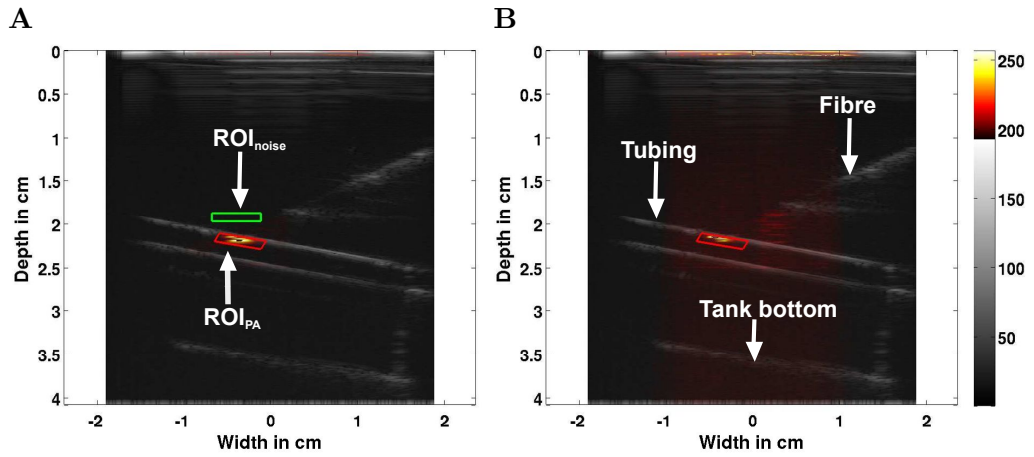
Figure 4.16: Composed PA and US image for the tubing filled with ink at: **A** 6 mm, **B** 8 mm. The tubing was immersed in intralipid 0.1%.

The intensities of the signal within ROI_{PA} against wavelength for the control experiment and ink, are shown in Fig. 4.17 A and B respectively. Each point of the plot corresponds to the median of the filtered acquisitions with error bars showing the median absolute deviation.

In contrast with the previous experiment, here most of the frames from water remained after the filter, and no significant change was observed for these control measurements at different distances. Compared to the control measurements, larger changes were observed for ink (4.17 B), where a decrease in the intensity at wavelengths under 750 nm can be observed at all distances. The closest distance interrogated here (6 mm) is in the order of the furthest distance interrogated in the previous experiment (6.5 mm), where low intensities under 750 nm were also present.
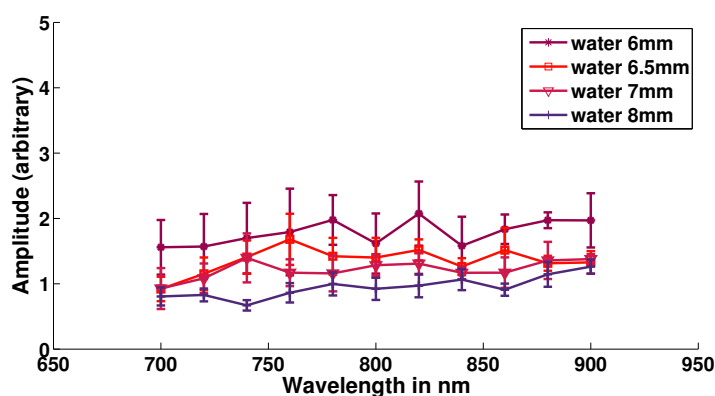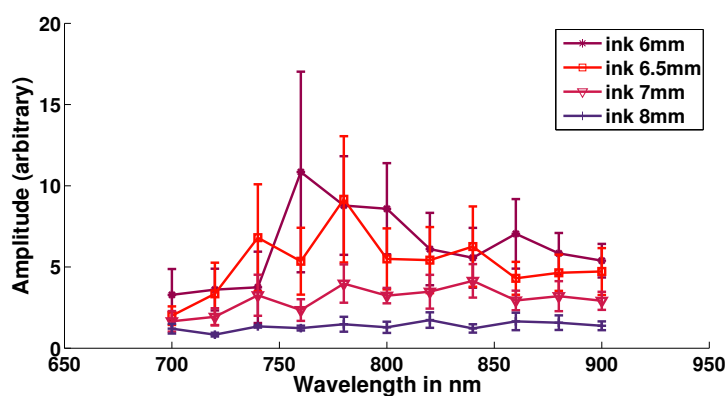
Figure 4.17: Photoacoustic signal from the tubing filled with: **A**, water and **B**, India ink for the tank surrounded by intralipid 0.1%.

PA response at 6 mm is shown in Fig. 4.18 together with the computer simulation for the same distance. It can be noted that the simulated absorption holds no resemblance to the experimental PA signal where very low amplitude is found at wavelength below 740 nm followed by a rapid signal increase at 760 nm. One source of disagreement between the curves can be attributed to the variation of true optical parameters of the media and those used for the simulations. However, the geometry of the problem is expected to be the main cause of nonconformity.

Absorption in the simulations is the result of the integration of all the events taking place in the detection volume. Absorption by ink is therefore enhanced by photons coming from all directions into the volume. For the experiments, the PA signal comes from the boundary of the sample. Given the low scattering of ink, absorption would depend on the distribution of light arriving from the top of the

sample. In this case the incoming light is shaped by the intralipid and reaches low penetration at short wavelengths. Attenuation of the incoming light due to water absorption would also be expected at long wavelengths when the distance to the tubing increases.
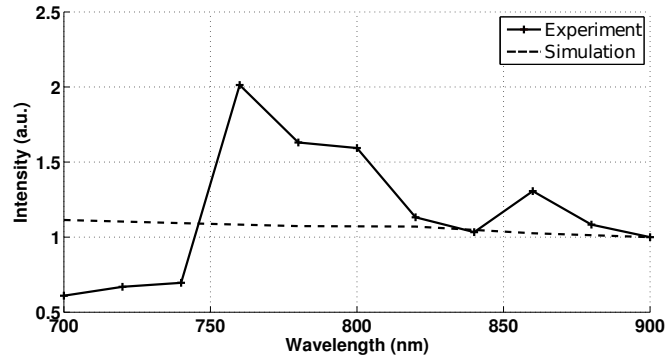
Figure 4.18: PA response at 6 mm and the correspondent result from the MC simulation (Fig 4.8 A). Each curve is scaled by the value of its amplitude at 900 nm.

The intensity of the photoacoustic signal against distance at 700, 800, and 900 nm, is shown in Fig. 4.14. An exponential decay of the signal at 700 and 800 nm was observed. The non-exponential decay at 900 nm is probably due to errors in the adjustment of the distance as mentioned before. In this case the highest amplitude was measured at 800 nm, but in contrast to the previous case (Fig. 4.14), the lowest amplitudes were obtained at 700 nm.
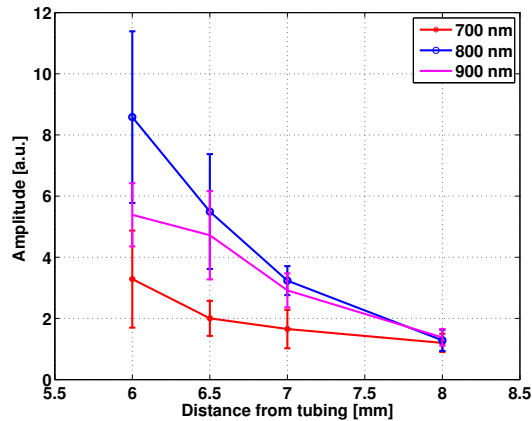
Figure 4.19: Variation of the photoacoustic signal from ink in the selected ROI at different distances.

4.4 Blood experiments

In order to analyse the PA response of blood, a second experiment was performed replacing the content of the THV-500 tubing with a RBC solution prepared by diluting human RBCs (from expired donations) with PBS 0.01 [M] in a proportion to obtain the equivalent of 40% HCT. The RBC solution was oxygenated by stirring; CO-oximeter measurements took place during this process until no further increase of oxygenation level was achieved. After leaving the solution to rest for about 2 minutes, it was circulated by means of the peristaltic pump used in the previous experiment, which in this case also helped to avoid cell sedimentation within the tubing, and damage to the cells caused by heat. Oxygen saturation and haemoglobin content of the RBC solutions were measured with the IL682 CO-oximeter (Instrumentation Laboratory, Massachusetts, USA).

Figure 4.20 shows the absorption coefficient of blood for the measured values of SO_2 and haemoglobin concentration of two RBC solutions (Table 4.2). It can be noted that the absorption coefficient is lower but do not vary significantly from that used for the simulations (Fig 4.6 B), so that comparisons with them are still valid.
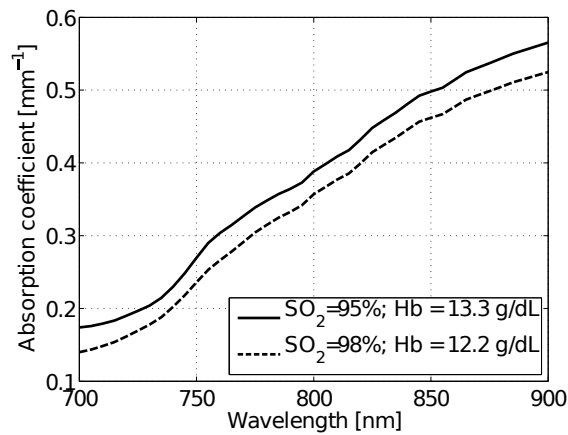
Figure 4.20: Absorption coefficient for the oxygenation values of the prepared RBC solutions (data from [Prahl]).

Table 4.2: Haemoglobin concentration and oxygen saturation of the RBC solutions

Sample	Hb (g/dL)	%SO_2 beginning	%SO_2 end
A	13.3	94.1	96.8
B	12.2	97.4	98.1

Two sets of acquisitions were performed, one for each of the RBC solutions in Table 4.2. The tubing containing the RBC solution A was surrounded with intralipid 0.1 % as was the case for the ink, while the RBC solution B was immersed in a tissue-like concentration of intralipid 1%. The tank and the position of the tubing can be seen in Figures 4.21 to 4.22.
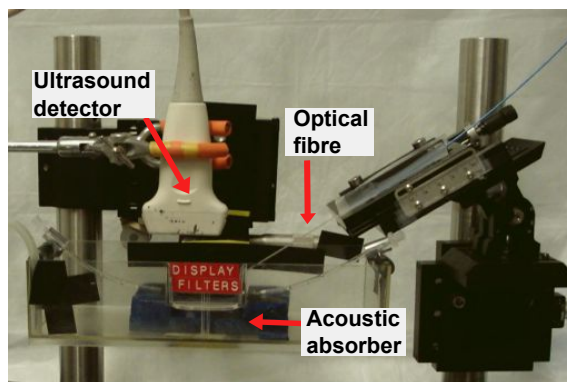
Figure 4.21: Placement of the fibre within the tank prior to be filled. The fibre is aligned with the tubing.
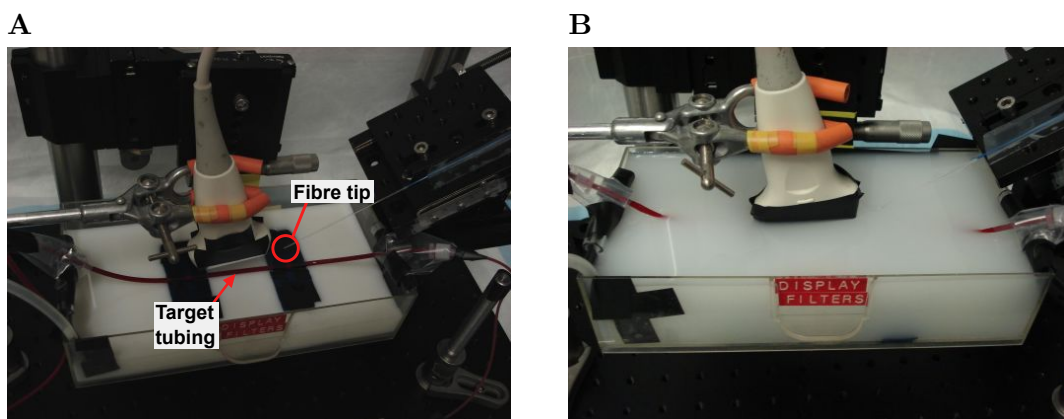
Figure 4.22: Filling of the tank with intralipid. Here the tubing contains RBC solution.

Here, the signal from the OPO was attenuated again with the 05 SN 25 metallic neutral filter, and the fibre was positioned at approximately 5 mm from the tubing. A series of 30 acquisitions were performed every 10 nm from 700 to 900 nm. This was repeated while moving the fibre away from the tubing.

4.4.1   Results

RBC solution A

Averaged power delivered by the fibre ranged from 15.9 mW to 31.2 mW as shown in Fig. 4.23 with a maximum at 740 nm. This first set of experiments correspond to the RBC solution A (see Table 4.2) and the tank filled with intralipid 0.1%.
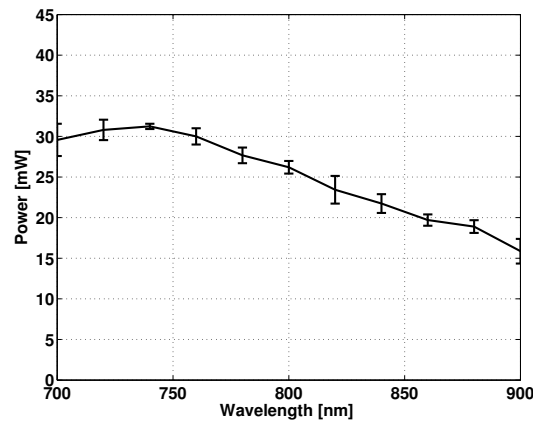

Figure 4.23: Power measured at the end of the optical fibre.

Figure 4.24 shows averaged images at 800 nm for the tubing filled with the RBC solution A. As in the previous figures, the region enclosed in red corresponds to the ROI_{PA}, while the region enclosed in green in the first frame, is the region corresponding to ROI_{noise}. Images were obtained at four distances: 6.0, 6.5, 7.0 and 8.0 mm. Figures A and B show the composed US and PA images at 6.0 mm and 8.0 mm. Image artefacts due to reflections by the tubing are pointed in each image.
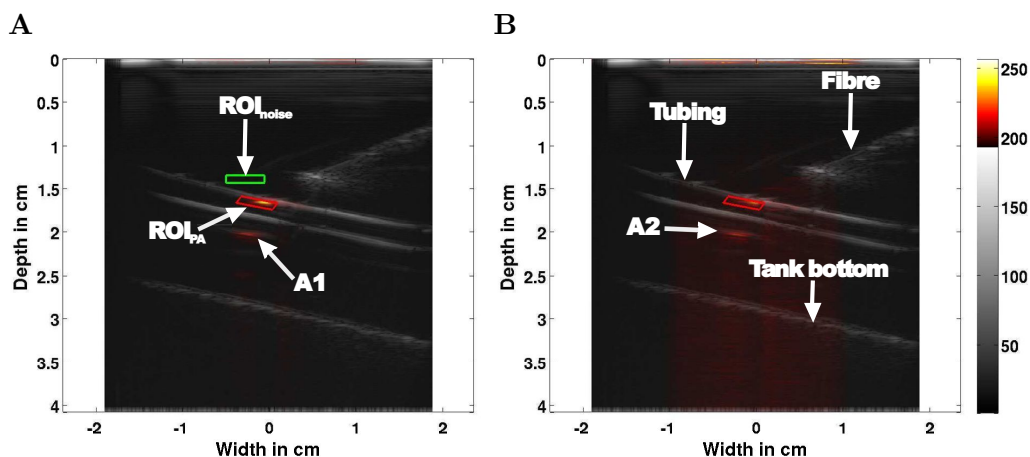
Figure 4.24: Composed PA and US image for the tubing filled with the RBC solution (A from Table 4.2) at: **A** 6 mm, and **B** 8 mm. The tubing was immersed in intralipid 0.1%. A1 and A2 point to artefacts in the image originated by reflections at the lowest side of the tubing.

The amplitude of the signal at ROI_{PA} against wavelength for water and the RBC solution A is shown in Fig. 4.25 A and B respectively. No significant change in amplitude was observed for the control measurements at different distances, but an increase of signal at larger wavelengths can be noted. Stronger changes due to distance were present for the blood sample. An increase with wavelength was present at all distances as expected from blood absorption (see Fig. 4.20). However an unanticipated peak with large variation of the median at 710 nm was observed.

A
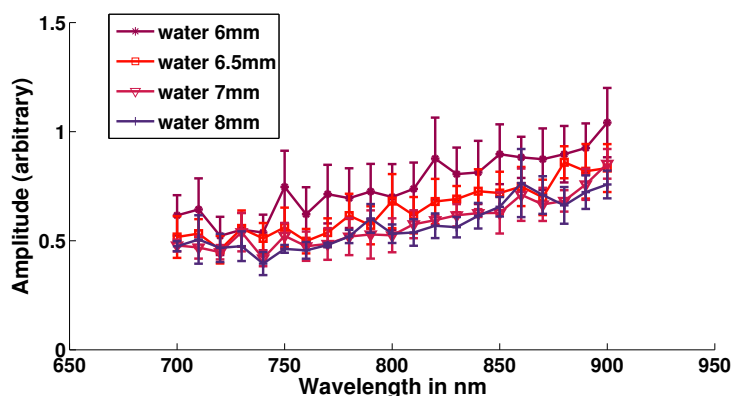
B
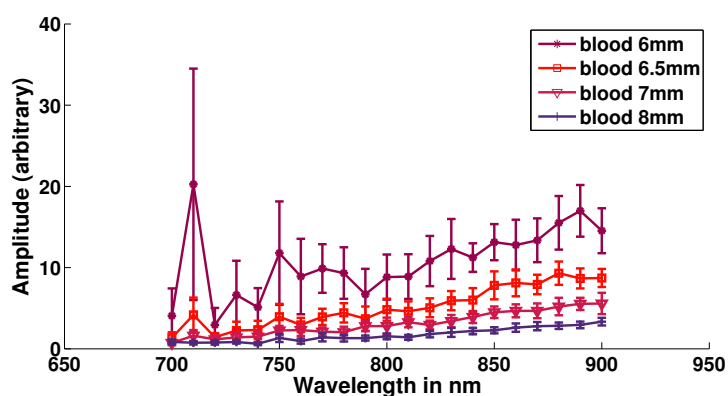
Figure 4.25: Photoacoustic signal from the tubing filled with: **A**, water and **B**, RBC solutions for the tank surrounded by intralipid 0.1 %.

Mean PA values for the frames obtained at 6 mm and wavelengths of 710 nm and 800 nm are shown in Fig. 4.26 for comparison, and to verify whether the 710 nm peak was due to an outlier in the data. A larger variability of the values can be noticed in Fig. 4.26 A, for 710 nm. To further emphasize the amplitude increase and variability of this peak the mean PA values at ROI_{PA} before normalisation are plotted in Fig. 4.27. This figure shows that the variation at 710 nm is due to the widely distributed intensities with no evident outliers such as those clearly seen at 730, 880 and 890 nm.

A

B
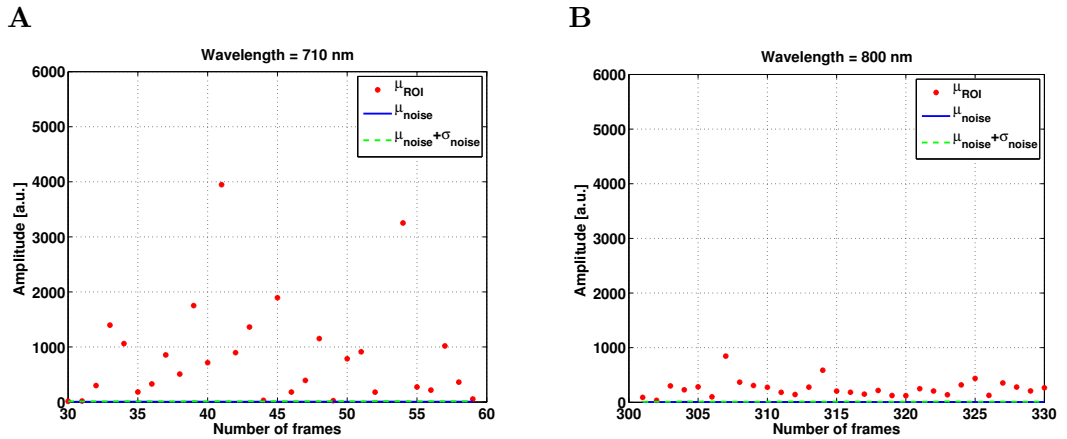
Figure 4.26: The red dots show the mean PA value at 6 mm and the tubing filled with the RBC solution A for all the frames at two specific wavelengths: **A** 710 nm, and **B** 800 nm. The green dashed line correspond to the threshold level. Compared with values at 800 nm, the mean values at 710 nm show large variability and higher intensity, with most of the values falling above noise levels.
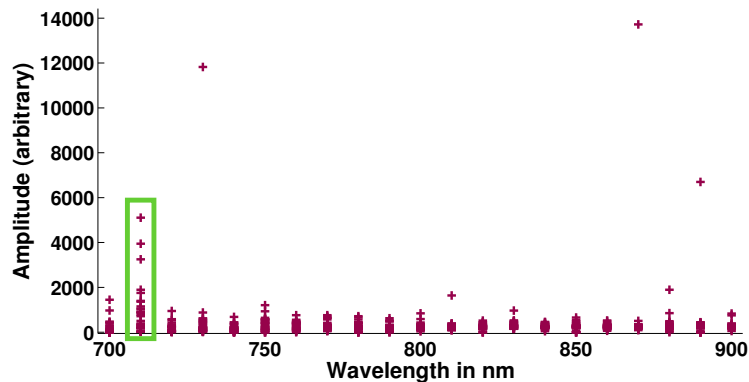
Figure 4.27: Mean PA values at ROI_{PA} after filtering and before normalisation. The square encloses the data at 710 nm showing the distribution of the mean PA values. Compared with other wavelengths the outliers can be visually identified, the points at 710 nm are more distributed among the range of values.

Figure 4.28 shows the PA signal at 6 mm together with the correspondent simulation of blood absorption with a layer of intralipid 0.1 %. Good agreement between the curves is observed. A possible reason is that the large scattering and absorption of blood in the simulations causes light being absorbed rapidly after entering the second medium, thus preventing the influence of photons coming from any other direction than the top.
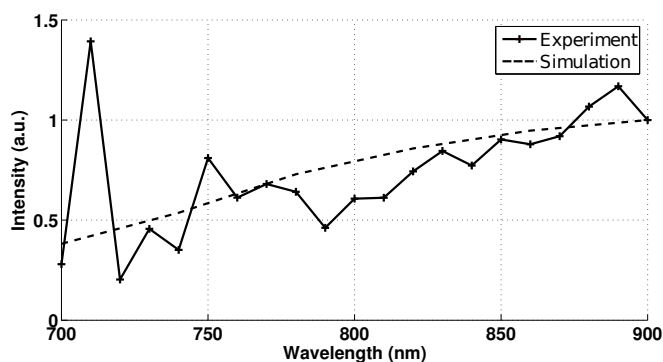
Figure 4.28: PA response at 6 mm and the correspondent result from the MC simulation (Fig 4.8 C). Each curve is scaled by the value of its amplitude at 900 nm.

The intensity of the photoacoustic signal from blood surrounded by intralipid 0.1% is plotted against distance at 700, 800, and 900 nm in Fig. 4.29. An exponential decay was observed for all the curves. Larger intensities were present at longer wavelengths despite the rise of the signal at 710 nm shown in the previous figure.
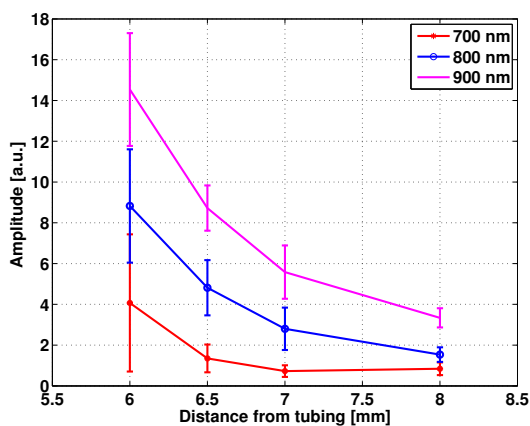
Figure 4.29: Variation of the photoacoustic signal from blood in the selected ROI at different distances.

RBC solution B

These experiments correspond to the RBC solution B (see Table 4.2) and the tank filled with intralipid 1 %. Averaged power delivered by the fibre ranged from 18.9 mW to 33.2 mW as shown in Fig. 4.30 with a maximum at 740 nm.
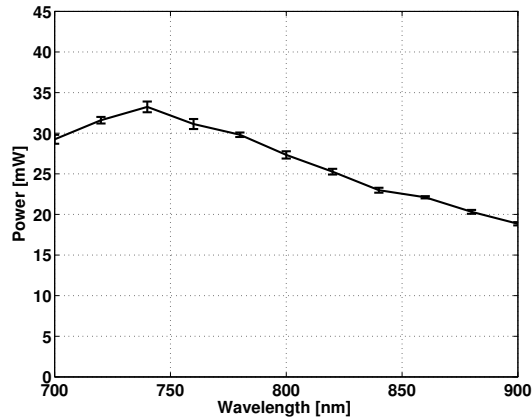
Figure 4.30: Power measured at the end of the optical fibre.

Figure 4.31 shows averaged images at 800 nm for the blood-like target. Images were obtained at: 4.0, 4.2, 4.5, 5.0, 5.5 and 6.0 mm, shorter distances were required because lower light intensity reached the tubing due to the high intralipid scattering. Figures 4.31 A and B show the composed US and PA images at 4.0 mm and 6.0 mm. Image artefacts are also present in these images showing the reflection of the tubing wall.
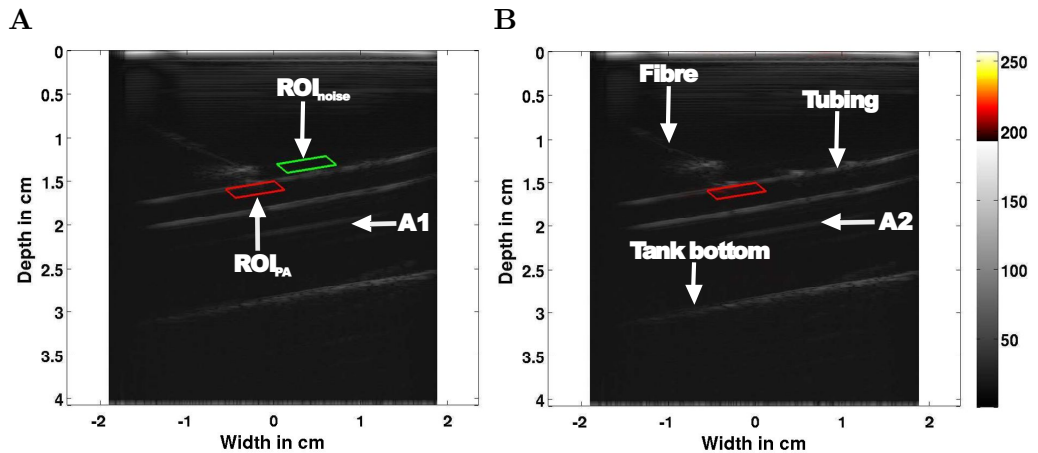
Figure 4.31: Composed PA and US image for the tubing filled with the RBC solution B (Table 4.2) at: **A** 4 mm, and **B** 6 mm. The tubing was immersed in intralipid 1%. A1 and A2 point to artefacts in the image originated by US reflections at the lowest side of the tubing.

Intensities of the signal for the control experiment and the RBC solution are shown in Fig. 4.32 A and B respectively. Here, large changes were observed in the control measurements, especially at 4.5 mm, exhibiting noisy behaviour, which

could be possibly caused by an unintentional movement of the system. Aside from the signal at 4.5 mm, the rest of the measurements from water showed similar decrease in intensity with distance, and the peak at 710 nm was present, contrary to the control measurements in Fig. 4.25 A. Stronger changes due to distance and an intensity peak at 710 nm were observed in the results from blood (4.32 B).
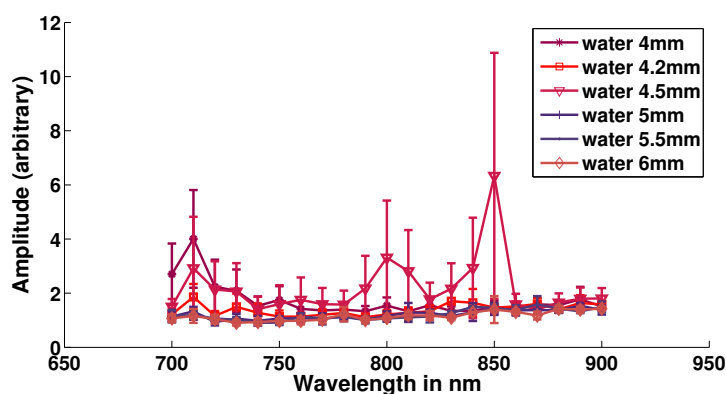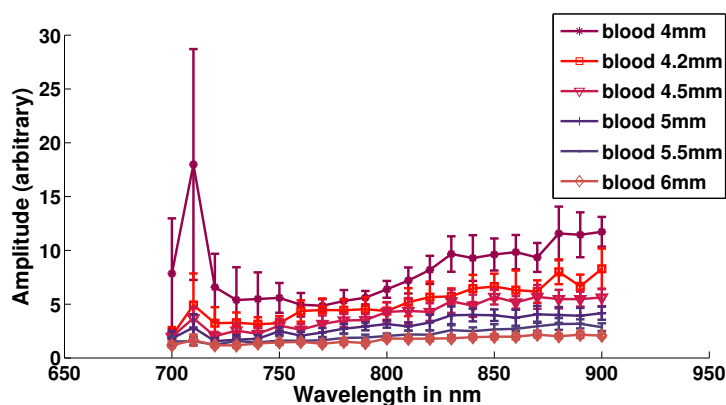
Figure 4.32: Photoacoustic signal from the tubing surrounded by 1.0% intralipid and filled with: **A**, water and **B**, RBC solution B.

Figure 4.33 shows again the PA signal at 6 mm together with the correspondent simulation of blood absorption with a layer of intralipid 1%. Good agreement between the plots is also found in this case.
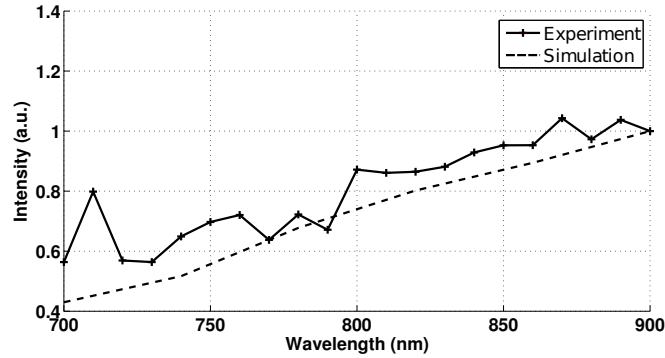
Figure 4.33: PA response at 6 mm and the correspondent result from the MC simulation (Fig 4.8 D). Each curve is scaled by the value of its amplitude at 900 nm.

In order to analyse the largest distances at which blood was detected, the PA signal from the control measurements at 4, 5, and 6 mm, and the signal from the RBC solutions at 5.5 and 6 mm are shown together in Fig. 4.34. The peak at 710 nm is more evident here for measurements of water at a distance of 4 mm. When compared to the PA signal of water at the same distances, the signal from blood can still be differentiated mainly at longer wavelengths for which oxyhaemoglobin exhibits higher absorption. Here, blood PA response at 900 nm is about two fold of that for water for a 6 mm fibre-tubing separation.
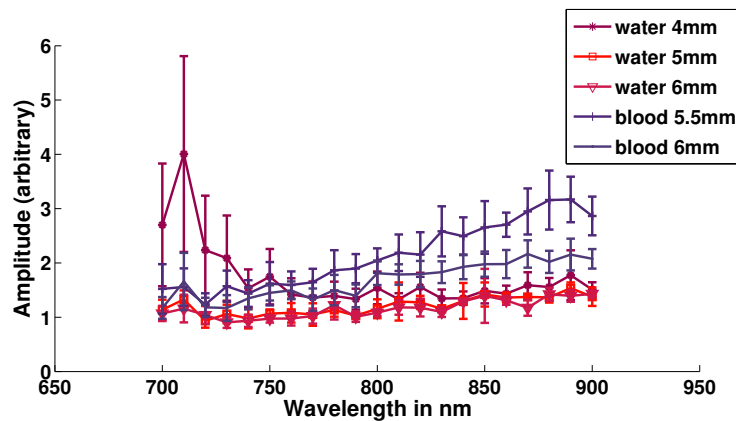
Figure 4.34: Comparison of the PA signal obtained with water and the farthest distances measured with the RBC solution.

The intensity of the photoacoustic signal against distance is shown in Fig. 4.35. An exponential decay at 900 nm was observed. Decay of the signal at 800 nm and 900 nm, however do not exhibit a smooth exponential decay, and the amplitude of the signal at 700 nm overtakes the value of the signal at 800 nm for the clos-

est fibre-tubing position, although this comes from the unexpected 710 nm peak. With exception of this point, the amplitude of the signals showed an increase with wavelength.
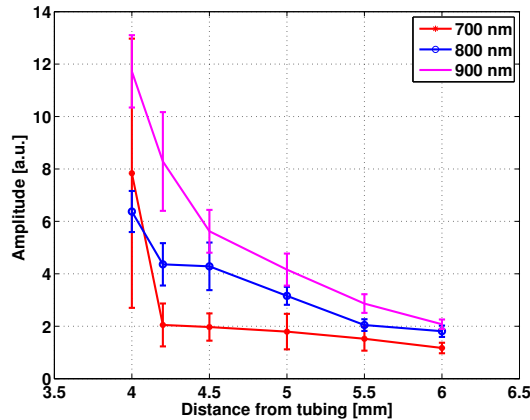
Figure 4.35: Variation of the photoacoustic signal from blood in the selected ROI at different distances.

4.5 Discussion

This chapter introduced the possibility of using multispectral photoacoustic imaging for the detection of a blood vessel during a needle puncture. The prompt detection of vascularities may be crucial while performing peripheral nerve blocks, where a vessel puncture could lead to toxicity and haematoma.

The photoacoustic technique proposed here uses illumination from an optical fibre that can be fitted into a needle. In comparison with surface illumination, placing the fibre into the needle would overcome any movement restriction imposed from attaching the illumination system to the ultrasound detector. As emphasized in the work of [Piras et al., 2013], in this configuration the needle could still generate a PA signal from the (illuminated) needle tip where the fibre's end would be placed. This feature would be useful to discern the distal end of the needle from the rest of its metal body in a transversal view. During the experiments shown here, the fibre was not placed into a needle in order to have good control over the position and alignment of the fibre, tubing, and detector. The coating diameter of 1035 μm of the actual fibre would allow to use needle gauges up to 17 gauge (1.473/1.067 mm OD/ID). If used within a needle, the fibre could be placed into the stylet to be safely removed after the injection point has been located [Balthasar et al., 2012b],

in this case larger gauges or smaller fibres would be required.

A very advantageous feature of this PA technique is that acoustic detection instruments (such as the one use in this research) are being built in cases similar to US probes. Therefore, there will be no added complexity to the current US guidance technique.

Aside from the real time image being displayed for the evaluation by the physician, another factor to be taken into account in a clinical setting is the wavelength dependant information, which in this work has been post-processed. One option to gain information from the multispectral possibilities of the technique in a real-time setting is to use the (known) spectral response of the needle material so that the photoacoustic signal coming from the needle tip could be used as a reference for the photoacoustic response of the target tissue. In this way, a smaller set of selected wavelengths could be use to differentiate between specific tissues.

The results for four acquisition sessions were presented. In the first two, a tubing with ink was imaged in a medium with intralipid 0.1 % . For one experiment, the power was slightly higher than the other and fibre-tubing distances were shorter. Next, two set of tests were performed with the tubing filled with RBC solutions. The experiments were performed with the tubing immersed in intralipid 0.1 % and 1% in each case. The second set was interrogated at closest distances given that the higher scattering of the intralipid 1% attenuated more rapidly the signal.

As it was seen in Eq. 1.20, the properties of the sample influencing the PA signal are the illumination, the absorption and scattering coefficient, and the Grüneisen parameter. At room temperature the Grüneisen parameter has a value of 0.11 and 0.25 for aqueous solutions and blood respectively [Oraevsky et al., 1997; Cox et al., 2009] (so it might be expected a larger PA response from blood when ink's absorption is matched). Assuming constant Grüneisen parameters and an absorption-dominated process at the sample, the photoacoustic response was expected to be mainly dependant on the illumination of the sample and its absorption coefficient.

The illumination of the sample in this case depended on laser power, the intralipid optical properties, and the fibre-tubing distance. The power of the light delivered to the tubing was wavelength dependant being highest for wavelengths around 740 nm. This condition was compensated by normalisation of the output by the power measurements taken at the end of the image acquisition. As seen from Figs. 4.15, 4.10, 4.23, and 4.30, the delivered power by the fibre differed, but it was assumed to remain approximately constant during the time of the experiment.

Signal decay after the passage of light through intralipid was expected to be accentuated by the chromophore within the tubing. To corroborate this, the intensity of the signal was plotted against distance at different wavelengths, but the curves did not exhibit a rapid exponential decay in all cases. It is possible that the distance for the ink experiments shown in Fig. 4.14 was not well registered (i.e. human error due to parallax). Additionally, misalignments of the system could also be a source of error in these plots. The size and extent of the ROI may also have been influencing the curves.

In the 700 to 900 nm range, water absorption is very low and no PA signal was expected. However, with exception of the first session of acquisitions, control measurements in water exhibited considerable absorption and wavelength dependence. In this case, the PA signal obtained with water may have been influenced by the blood measurement carried beforehand for alignment.

In Fig. 4.5 the scattering by intralipid is higher at shorter wavelengths, so that light reaches shallower depths than it does at larger wavelengths. This phenomenon would help to explain the signal decrease with distance observed at short wavelengths in figures 4.12 B from ink and the rapid decrease in the 710 nm peak for figures 4.25 B and 4.32 B.

The PA response in Fig. 4.18, significantly differs from the absorption trend expected to be following from the simulations. In this figure lower PA signal is detected at wavelengths below 750 nm followed by a rapid increase in signal and a decay afterwards. The experiments with the RBC solutions showed good agreement with simulations (see Figs. 4.28 and 4.33).

MC simulations helped to estimate the trend which PA signals would follow from tissue absorption. As already mentioned, MC results come from rough approximations of the geometry and optical parameters so that in Fig. 4.18 may indicate that higher scattering from intralipid was present at shorter wavelengths in a way that fewer photons remained to be absorbed at the tubing. Further, the MC simulation for the blood experiment points out the rare peak at 710 nm addressing the possibility that this peak originates from other causes than the presence of RBCs.

An increase in intensity and variation of the PA signal around 710 nm was observed for the RBC experiments. Although intralipid is responsible of attenuating rapidly the signal at larger distances, the origin of the specific rise at 710 nm remained unclear.

Possible trigger issues may have also affected the experiments increasing the median absolute deviation. Imperfect synchronization of the acquisition with the laser pulses may have some frames been created by either no pulse or by portions of two pulses instead of by one single laser pulse. In an effort to mitigate this problem, multiple acquisitions were taken at each wavelength and the median was reported, however a better solution is needed.

Overall, the multispectral feature of the method resulted in distinguishable signals from India ink and the RBC solutions. For the more realistic scenario shown here with the RBC solution in intralipid 1% , signal from a fibre tubing distance of 5 mm was obtained with values above those of the control measurements.

Conclusions and future work

Blood vessels encountered during a needle or catheter insertion are delicate structures. Consequences of a vascular puncture vary among procedures, in some cases carrying severe complications such as cardiac arrest [Mulroy, 2002]. In this thesis, the versatility of optical guides was explored for the detection of blood during minimally invasive and anaesthesiology procedures.

Reflectance spectroscopy with a double clad fibre was investigated for the differentiation of venous and arterial blood. The small size of the fibre offers great versatility for its integration into a number of medical devices and their respective accessories such as stylets and guidewires. Computer simulations showed that the double clad fibre was able to respond to SO_2 variations, and experimentally measured slopes of the response curve (Fig. 2.17) confirmed this sensitivity to SO_2 changes showing repeatable values. When crossing from oxygenated (100% SO_2) to deoxygenated (70% SO_2) blood an increase of the signal was detected. This discrimination would be particularly valuable for the confirmation of a correct puncture during procedures such as venous cannulation, or during a transseptal puncture.

Reflectance spectroscopy via optical epidural catheter was tested ex vivo in the lumbar region of a swine. The haemoglobin parameters extracted from the spectra at 796 and 545 nm and the average intensity showed qualitative differentiation between tissues including withdrawn blood (extracted less than 2.5 hours after death). An automated method for discrimination between blood related and non-blood related tissues was tested using a set of spectra recorded on ex vivo chicken tissue. This approach employed information from a larger number of wavelengths to improve tissue classification. A simple classifier, based on logistic regression, was able to classify blood and non-blood related tissues with an accuracy of 98%. It is important to note that in this case blood related tissues included vessels of various sizes, and that these intact vessels were interrogated by placing the probe on their surface.

The aforementioned methods for haemoglobin detection rely on reflectance spectroscopy, a purely optical method, that is limited by the attenuation of light in biological tissue. The double clad fibre, for instance, might be suited for *in situ* verification of a correct puncture, while the optical catheter would be suitable for the monitoring of catheter migration. However the physician may want to receive feedback while manoeuvring a device prior to specific procedures. Thus, photoacoustic imaging was examined as a possible option for invasive device placement.

It was possible to acquire and display in real time simultaneous conventional ultrasound image and a photoacoustic image from an illuminated target, which would help to take more informed decisions in a clinical context. Experiments with solutions of India ink and of RBC's showed distinguishable patterns of the photoacoustic multispectral signals. Based on the expectations from MC simulations, it was possible to highlight the importance of the close environment of the structure being imaged, since it would affect the amount of light reaching the structure. The multispectral curves from blood did not show a homogeneous increase in the photoacoustic signal as expected, but exhibit a peak in the amplitude at 710 nm, which needs to be explored further. Using the system described, photoacoustic imaging was used to detect a signal at a distance of up to 5.5 mm from a target within the blood-like solution.

A limitation of the prototypes mentioned above and their use of optical fibres is the direct connectorisation of light sources and detectors. For instance, during an epidural procedure a Tuohy needle is first placed into the epidural space and then a catheter is placed into this needle. After the catheter is advanced to the desired position the Tuohy needle needs to be removed. The needle is then gently pulled out while providing counter-traction to the catheter. With the current optical fibre connections, a needle could not be freely removed from the catheter.

In the case of the DCF, experiments were limited to samples which simulate concentrations of blood at physiological levels in normal conditions. However, it is also important to consider cases in which patients suffer from a condition or disease that alters their blood properties. Distinction between deoxygenated and oxygenated blood in a clinical scenario may be hampered in patients with diseases, such as congenital heart disease [Oliver Jr. et al., 1997], where venous and arterial blood is combined. The results shown here suggest that the response to changes in oxygen saturation were not strongly dependant on haemoglobin concentrations. However more experiments employing a larger range of haemoglobin concentrations would help to determine whether this fibre is capable to resolve such differences.

While photoacoustic imaging increased the distance over which signal from the tissue of interest can be obtained, the safety limits on the amount of delivered energy (20 $\frac{mJ}{cm^2}$ [Kim et al., 2010]) is not yet being taken into account. Therefore, the detection distances with the present system would become shorter under this restriction.

As mentioned previously, the actual distance over which a needle with an optical fibre would detect a blood vessel will depend not only on the laser energy, but also on the tissue structure. In this thesis the case of a homogeneous medium surrounding a blood vessel was analysed. However, it is possible to encounter multiple structures and tissues (e.g. muscle, ligament, fat) in the path of the needle that also modify the light distribution between the probe and the vessel. Ultrasound can be used to image the shape and size of the structure of interest together with the adjacent areas, which can be then used to infer the cause of unexpected features in the PA signal. Yet, this analysis would require previous knowledge of the optical characteristics of the tissues.

Improvements in the optical catheter would include the connection design and the manufacture of a more flexible prototype. In this case contact-less coupling will be necessary due to the nature of the catheter insertion which requires a needle to be removed from around the catheter. Here the connectorisation may involve dissolving the material of the catheter body in a very reduced area enough to expose the optical guides for illumination and light detection. In this case the connection would leave most of the catheter material in place, waiving the need of attaching another catheter for the feeding of the device.

Since catheters are used for continuous drug administration, the effect of an injected substance in the region surrounding the catheter distal end will need to be investigated. It is possible that the presence of delivered drugs, and that of other chromophores like carotenes in the epidural space would still allow for the detection of blood vessels given the strong haemoglobin absorption, yet they may limit light penetration, reducing the distance at which a vessel can be detected.

In terms of getting closer to an automated tool, a greater amount of spectral data needs to be obtained from the epidural region and intact blood vessels within the region in order to train the classification algorithm. After such training, the automatic detection method could be tested and evaluated. With a larger set of data it may be possible to add the differentiation of veins and arteries to the classification problem.

To improve the utility for the DCF in a clinical setting a prototype of the integrated needle and fibre needs to be developed, and evaluated in the presence of blood flow. It will be important to investigate whether the sensitivity varies under this condition, and how is the noise in the signal been affected. The need for contact-less optical coupling will depend on the intended application of the device.

Detection of deoxygenated blood may also be explored in order to get a better scope of photoacoustic blood imaging. The current work was limited to oxygenated blood to avoid uncertainties in the optical properties due to the presence of yeast (the de-oxygenation method used through this work). Blood deoxygenation can be carried out using a mixture of gases as described by [Laufer et al., 2004].

Future research in the use of optical methods in minimally invasive devices may include the extension of the working wavelength range. The optical fibre materials used in this project, worked well in the near-infrared range allowing for haemoglobin detection, but their use at longer wavelengths was not investigated. Research within an extended wavelength range would potentially allow detection of other chromophores. Distinctive absorption peaks have been identified for lipids between 900 nm and 1600 nm [Nachabé et al., 2010]. The identification of lipids in combination with blood would facilitate the identification of a greater variety of tissues.

Another aspect that can be developed in the future is the creation of algorithms that allow for the quantitative estimation of blood properties such as oxygen saturation and haemoglobin concentration, as well as the presence of different haemoglobin forms. In general, being able to obtain quantitative information would provide the device not only with blood detection capabilities but also with the ability to retrieve valuable information for tissue diagnosis.

Inverse Monte Carlo methods have been use for the estimation of properties from reflectance spectra [Roggan et al., 1999; Brown et al., 2009], however these approximations can be very time consuming. On the other hand, quantitative results obtained from photoacoustic data have proven to be a difficult task mainly by the non-linear dependence on fluence and actual variations of the Grüneisen parameter [Cox et al., 2009]. Moreover, any inverse method may rely on the knowledge of the optical properties from any tissue that can be encountered during a procedure. The extraction of tissue's optical properties can be itself a complicated task as can be inferred from the variations on the blood optical properties found in the literature as seen in Chapter 2.

Classification algorithms can be explored as an alternative for tissue diagnosis

[Keller et al., 2010; Chandra et al., 2010]. These tools would require a large set of data for training and testing, and would result in a set useful only for a particular region of the body (in contrast with the deterministic methods for which by having all the optical data available would, in theory, allow for the specification of tissue composition). Moreover, the data set would be highly dependant on the conditions of the experiment (e.g. instrument variations, and environmental conditions), so higher control measures would need to be implemented.

However, a promising feature of these classification algorithms could be the implementation of a more complex tissue classification given a certain group of patients such as adults and children. For instance, fat cells in the epidural space of children are smaller and less numerous than in adults [Reina et al., 2006], resulting in a difference of scattering. Age-related diseases can also cause variation in the composition of the epidural space, such as the formation of epidural haematoma [Reina et al., 2007]. Therefore, the influence of various factors in the optical response of tissue makes this field open to further research.

As seen in this thesis, the correct placement of an interventional device is essential during minimally invasive and anaesthesiology procedures, and the identification of a blood vessel can not only avoid complications, such as bleeding toxicity as mentioned previously, but can also be used as an indicator of anomalies, such as cancerous tissues. Identifying and quantifying blood content in tissue will be very useful for assisting diagnosis and therapy as well aiding placement of interventional devices.

The techniques analysed in this thesis offer a relatively simple solution which make use of devices during common procedures to retrieve information about the distal end environment. The work presented suggests that the use of optical fibres coupled to interventional devices such as needles and catheters, are able to feedback information about the correct placement of the device leading to significant benefits to the patient.

Appendix A

Preliminary tests (Double Clad Fibre)

The performance of the DCF (shown in Figure A.1) to detect oxygenation differences within the wavelength range from 790 to 860 nm was empirically analysed in RBC's solutions. The RBC's solutions were prepared from expired donated red blood cells diluted with phosphate buffered saline solution 0.01 M to achieve a haematocrit level about 40%. De-oxygenation of the sample was obtained by adding sodium hydrosulfite.
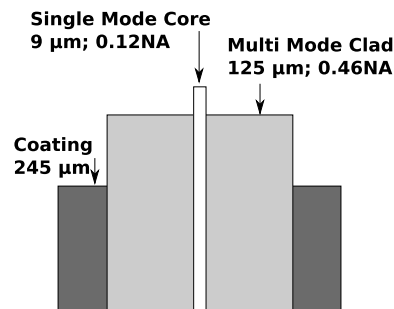
Figure A.1: Dimensions of the double clad fibre used in these tests.

A.1 Setup

Light from a supercontinuum source (Superlum BLM-S-820) was attenuated by introducing a gap of 7 cm in its pathway and re-focusing the light using a pair of collimators. Once attenuated, the light was directed via a monomodal fibre to the

core of a the DCF. The tip of the DCF was placed in direct contact with the sample whose spectrum was to be acquired. Reflected light from the sample was detected by the inner core of the DCF, and coupled into a multimodal fibre to a spectrometer (MayaPro, Ocean Optics, Inc). The setup is shown in Figure A.2.
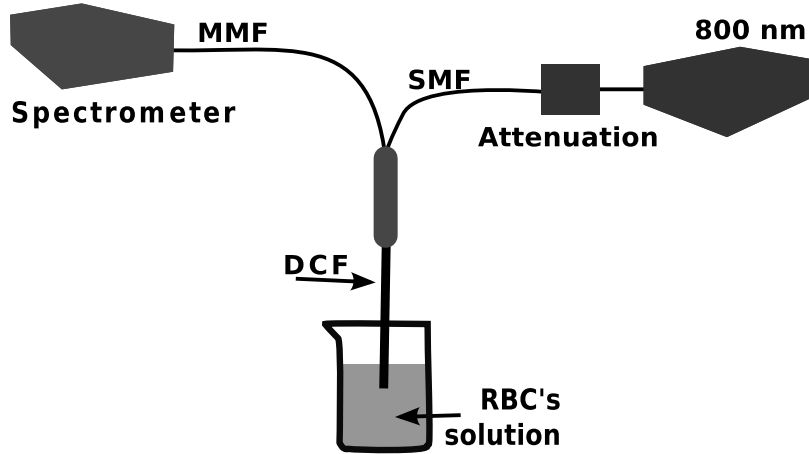
Figure A.2: Experimental setup. A broadband light source deliver light to the DCF single-mode core. The detected light at the inner cladding is sent to a spectrometer and the data are acquired with LabVIEW.

A.2   Stability of the SO_2

One problem when dealing with ex vivo blood experiments is that exposure to air at room temperature can be enough for the blood to fully oxygenate. This is particularly problematic when performing measurements at specific oxygenation values. Since the present work deals with this situation, a time window where the oxygenation values remain relatively stable was estimated. For this purpose, deoxygenated RBC solutions were monitored over time.

Two 15 mL RBC's solutions (sample A and B) were prepared by mixing RBCs and PBS. For deoxygenation, 2.5 mg/mL and 5 mg/mL of sodium hydrosulfite were added to sample A and B respectively. The samples were left for about an hour in a closed container. After this time the achieved decrease in oxygenation was from 85.3% to 74.9% for sample A, and from 86.0% to 70.9% for sample B.

The two blood samples were then left in an opened container to rest for an hour at room temperature, and the value of oxygenation was taken at 0, 10, 20 and 60 min. The results of these measurements are shown in Table A.2. These

data give an estimate of the time window within which no significant changes in the oxygen saturation of blood are expected. For the achieved oxygenation levels, it can be assumed that that saturation values were stable during the first 20 min after deoxygenation was achieved.

Table A.1: Oxygenation increase during an hour, starting from the lowest oxygenation value achieved.

	0 min	10 min	20 min	60 min
Sample A	74.9%	74.9%	76.2%	77.7%
Sample B	70.9%	71.3%	72.1%	73.5%

A.3 Response to SO_2

The deoxygenated sample B was gently stirred for allowing gradual re-oxygenation. CO-oximeter and spectroscopic measurements were taken consecutively at differents steps during this process, and after having rest the sample for a couple of minutes after each stirring. Re-oxygenation was achieved to 90.8%. Figure A.3 **a** shows three of the resulting spectra for a SO_2 of 70.9%, 80.8%, and 90.8%.

Figure A.3 **b** shows the intensity from all the achieved oxygenation levels of the sample at 790, 825, and 860 nm. Overall tendency in the amplitude of the signal suggests low sensitivity of the fibre to differentiate spectra over the studied wavelength range which might be caused by the small differences of haemoglobin absorption at those wavelengths, together with the influence of possibly variant scattering.

a
b
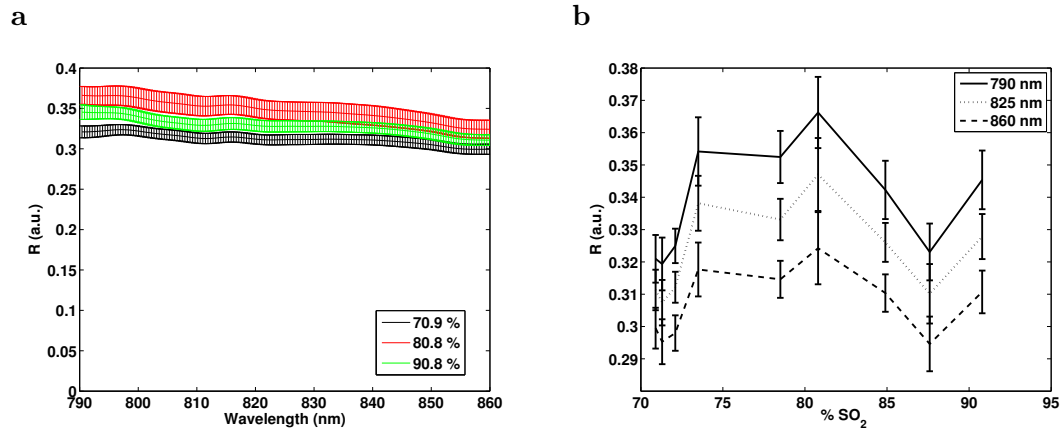
Figure A.3: a)Spectral measurements taken at different oxygenation values. Black and red lines correspond to the mean value and standard deviation of a set of 100 spectra acquired at each measurement. b) Intensity from all the oxygenation steps of the sample at 790, 825, and 860 nm

The results of this series of experiments revealed two main points that had to be tackled for the following experiments: 1) sodium hydrosulfite was not able to deoxygenate the RBCs for more than 20%, which is not ideal given that some batches of the RBC donations were almost fully oxygenated; 2) absorption changes in the range of 790 to 860 nm are not enough to produce an oxygen dependant response with the small source-detector separation of the fibre.

Appendix B

Photoacoustic detection, additional steps

As mentioned in Section 4.1.1, both, the US and PA response are detected by the Winprobe system which carries out data acquisition, beam-forming and image generation. The system has the capacity of adjusting for tissue depth by means of time gain compensation for the data acquisition.

After this step, the detected acoustic signal is digitized (at 40 MHz), and the echos that can be summed together are selected (the echoes coming from the same point in the tissue). Following, the signal goes through the apodization step, which is a necessary stage to remove aliasing effects due to data sampling.

To obtain the envelope of the signal, a Hilbert transformation is applied to the resultant radiofrequency signal so that its magnitude can be estimated. The resulting envelope is then compressed to 8 bits for display and storage.

As an example of the resulting envelopes, Fig. B.1 **a** and **b** show the resulting image and log(image) of these data respectively using the Matlab function imagesc[1]. This information corresponds to the image shown in Fig. B.2 for the tubing filled with blood and immersed in 0.1% intralipid, and a 6 separation from the optical fibre at 800 nm.

These resulting envelopes are the ones being stored in the PA frames, and which later are processed in Section 4.1.2. Here, the processing focuses on eliminating

---

[1]imagesc scales image data to the full range of the current colormap and displays the image.

blank frames that carries no information, and which were possibly acquired by a bad synchronisation of the Winprobe system with the laser pulse. This processing also corrects the data from the uneven power delivered by the laser. After these steps, the data is used for the analysis of wavelength dependance.

a   **b**
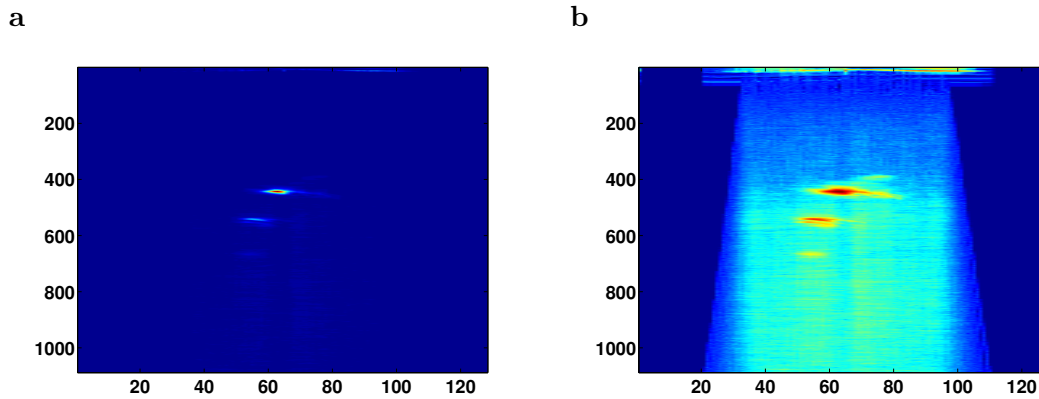
Figure B.1: Data from the PA experiments for the tubing filled with blood and immersed into 0.1% intralipid. **a** Raw data covering the full color range; **b** log(image) covering the full color range.

Additionally, an overlay image (Fig. B.2) is presented. This image was obtained after normalising the whole set at a given distance with respect to the largest value of all the regions of interest in the set. The reason behind this is to be able to compare the amplitude of the PA response at one wavelength with respect to another.
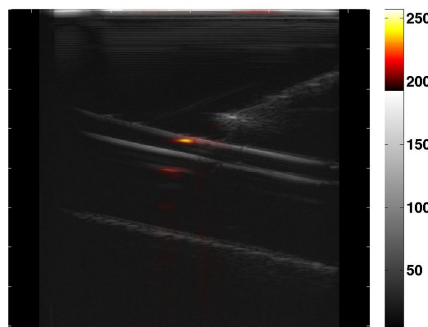
Figure B.2: Processed image (Fig. 4.24 accounting for normalisation over the whole experimental set and average over number of samples for each wavelength for the same data used in Fig. B.1.

Bibliography

J. Abbas, K. Hamoud, Y. M. Masharawi, H. May, O. Hay, B. Medlej, N. Peled, and I. Hershkovitz. Ligamentum flavum thickness in normal and stenotic lumbar spines. *Spine*, 35(12):1225–1230, 2010.

T. J. Allen, A. Hall, A. P. Dhillon, J. S. Owen, and P. C. Bearda. Spectroscopic photoacoustic imaging of lipid-rich plaques in the human aorta in the 740 to 1400 nm wavelength range. *Journal of Biomedical Optics*, 17(6), 2012.

Katherine Arendt and Scott Segal. Why epidurals do not always work. *Rev Obstet Gynecol*, 1(2):49–55, 2008.

D. Arifler, R. A. Schwarz, S. K. Chang, and R. Richards-Kortum. Reflectance spectroscopy for diagnosis of epithelial precancer: model-based analysis of fiber-optic probe designs to resolve spectral information from epithelium and stroma. *Applied Optics*, 44(20):4291–4305, Jul 10 2005.

D. Arifler, C. MacAulay, M. Follen, and R. Richards-Kortum. Spatially resolved reflectance spectroscopy for diagnosis of cervical precancer: Monte Carlo modeling and comparison to clinical measurements. *Journal of Biomedical Optics*, 11(6), Nov-Dec 2006.

V. C. Babaliaros, J. T. Green, S. Lerakis, M. Lloyd, and P. C. Block. Emerging applications for transseptal left heart catheterization. old techniques for new procedures. *Journal of the American College of Cardiology*, 51(22):2116–2122, 2008.

P. L. Baele, J. C. McMichan, H. M. Marsh, J. C. Sill, and P. A. Southorn. Continuous monitoring of mixed venous oxygen-saturation in critically ill patients. *Anesthesia and Analgesia*, 61(6):513–517, 1982.

A. Balthasar, A. E. Desjardins, M. Van Der Voort, G. W. Lucassen, S. Roggeveen, K. Wang, W. Bierhoff, A. G. H. Kessels, M. Sommer, and M. Van Kleef. Optical detection of vascular penetration during nerve blocks: An in vivo human study. *Regional Anesthesia and Pain Medicine*, 37(1):3–7, 2012a.

A. Balthasar, A. E. Desjardins, M. Van Der Voort, G. W. Lucassen, S. Roggeveen, K. Wang, W. Bierhoff, A. G. H. Kessels, M. Van Kleef, and M. Sommer. Optical detection of peripheral nerves: An in vivo human study. *Regional Anesthesia and Pain Medicine*, 37(3):277–282, 2012b.

B. A. Barth, S. Banerjee, Y. M. Bhat, D. J. Desilets, K. T. Gottlieb, J. T. Maple, P. R. Pfau, D. K. Pleskow, U. D. Siddiqui, J. L. Tokar, A. Wang, L. . Wong Kee Song, and S. A. Rodriguez. Equipment for pediatric endoscopy. *Gastrointestinal endoscopy*, 76(1):8–17, 2012.

A. N. Bashkatov, E. A. Genina, V. I. Kochubey, and V. V. Tuchin. Optical properties of human skin, subcutaneous and mucous tissues in the wavelength range from 400 to 2000 nm. *Journal of Physics D: Applied Physics*, 38(15):2543–2555, 2005.

B.Braun. B.Braun Regional Anesthesia . `http://www.bbraun.no/documents/Products/Regional_Anesthesia_03.12.pdf`.

P. Beard. Biomedical photoacoustic imaging. *Interface Focus*, 1(4):602–631, 2011.

B. Beauvoit, H. Liu, K. Kang, P. D. Kaplan, M. Miwa, and B. Chance. Characterization of absorption and scattering properties for various yeast strains by time-resolved spectroscopy. *Cell Biophysics*, 23(1-3):91–109, 1993.

J. E. Bender, K. Vishwanath, L. K. Moore, J. Q. Brown, V. Chang, G. M. Palmer, and N. Ramanujam. A robust monte carlo model for the extraction of biological absorption and scattering in vivo. *IEEE Transactions on Biomedical Engineering*, 56(4):960–968, 2009.

F. Bongard, T.S. Lee, T. Leighton, and S.Y. Liu. Simultaneous in vivo comparison of two-versus three-wavelength mixed venous (s vo2) oximetry catheters. *Journal of Clinical Monitoring*, 11(5):329–334, 1995.

L. B. Boschiero, P. Saggin, O. Galante, G. F. Prati, P. Dean, M. Longo, and G. Ancona. Renal needle biopsy of the transplant kidney: Vascular and urologic complications. *Urologia internationalis*, 48(2):130–133, 1992.

Phillip Bridenbaugh and Michael J. Cousins, editors. *Neural blockade in clinical anesthesia and management of pain*. Lippincott-Rave, Philadelphia, 1998.

David Brown. *Atlas of regional anesthesia*. Saunders/Elsevier, Philadelphia, PA, 2010. ISBN 1416063978.

J. Q. Brown, L. G. Wilke, J. Geradts, S. A. Kennedy, G. M. Palmer, and N. Ramanujam. Quantitative optical spectroscopy: A robust tool for direct measurement of breast cancer vascular oxygenation and total hemoglobin content in vivo. *Cancer Research*, 69(7):2919–2926, 2009.

M. Brynolf, M. Sommer, A. E. Desjardins, M. Van Der Voort, S. Roggeveen, W. Bierhoff, B. H. W. Hendriks, J. P. Rathmell, A. G. H. Kessels, M. Söderman, and B. Holmström. Optical detection of the brachial plexus for peripheral nerve blocks: An in vivo swine study. *Regional Anesthesia and Pain Medicine*, 36(4):350–357, 2011.

H. F. Bunn and B. G. Forget. *Hemoglobin–molecular, genetic, and clinical aspects*. W.B. Saunders Co, Philadelphia, 1986. ISBN 0721621813.

S. M. Burns, C. M. Cowan, P. M. Barclay, and R. G. Wilkes. Intrapartum epidural catheter migration: A comparative study of three dressing applications. *British Journal of Anaesthesia*, 86(4):565–567, 2001.

L. Cale and R. Constantino. Strategies for decreasing vascular complications in diagnostic cardiac catheterization patients. *Dimensions of Critical Care Nursing*, 31(1):13–17, 2012.

E. D. Cashwell and C. J. Everett. A practical manual of the monte carlo method for random walk problems. Technical report, Los Alamos Scientific Laboratiry, 1957.

M. Chandra, J. Scheiman, D. Simeone, B. McKenna, J. Purdy, and M. A. Mycek. Spectral areas and ratios classifier algorithm for pancreatic tissue classification using optical spectroscopy. *Journal of Biomedical Optics*, 15(1), 2010.

B. Chandrasekar, S. Doucet, L. Bilodeau, J. Crepeau, P. Deguise, J. Gregoire, R. Gallo, G. Cote, R. Bonan, M. Joyal, G. Gosselin, J. . Tanguay, I. Dyrda, M. Bois, and A. Pasternac. Complications of cardiac catheterization in the current era: A single-center experience. *Catheterization and Cardiovascular Interventions*, 52(3):289–295, 2001.

Y. C. Chang, J. Y. Ye, T. Thomas, Y. Chen, J. R. Baker, Jr., and T. B. Norris. Two-photon fluorescence correlation spectroscopy through a dual-clad optical fiber. *Optics Express*, 16(17):12640–12649, Aug 18 2008.

P. A. Cheng. The anatomical and clinical aspects of epidural anesthesia. i. *Anesthesia and Analgesia*, 42:398–406, 1963.

C. B. Collier. Why obstetric epidurals fail: A study of epidurograms. *International Journal of Obstetric Anesthesia*, 5(1):19–31, 1996.

B. T. Cox, J. G. Laufer, and P. C. Beard. The challenges for quantitative photoacoustic imaging. In *Progress in Biomedical Optics and Imaging - Proceedings of SPIE*, volume 7177, 2009.

J. C. Crockett. The thyroid nodule fine-needle aspiration biopsy technique. *Journal of Ultrasound in Medicine*, 30(5):685–694, 2011.

D. T. Delpy and M. Cope. Quantification in tissue near-infrared spectroscopy. *Philosophical Transactions of the Royal Society B: Biological Sciences*, 352(1354):649–659, 1997.

D. T. Delpy, M. Cope, P. Van Der Zee, S. Arridge, S. Wray, and J. Wyatt. Estimation of optical pathlength through tissue from direct time of flight measurement. *Physics in Medicine and Biology*, 33(12):1433–1442, 1988.

A. E. Desjardins, B. H. W. Hendriks, M. van der Voort, R. Nachabé, W. Bierhoff, G. Braun, D. Babic, J. P. Rathmell, S. Holmin, M. Söderman, and B. Holmström. Epidural needle with embedded optical fibers for spectroscopic differentiation of tissue: Ex vivo feasibility study. *Biomedical Optics Express*, 2(6):1452–1461, 2011.

M. F. Dillon, A. D. K. Hill, C. M. Quinn, A. O'Doherty, E. W. McDermott, and N. O'Higgins. The accuracy of ultrasound, stereotactic, and clinical core biopsies in the diagnosis of breast cancer, with an analysis of false-negative cases. *Annals of Surgery*, 242(5):701–707, 2005.

M. J. Earley. How to perform a transseptal puncture. *Heart*, 95(1):85–92, 2009.

D. J. Faber, M. C. G. Aalders, E. G. Mik, B. A. Hooper, and T. G. Van Leeuwen. Oxygen saturation dependent absorption and scattering of blood. In *Proceedings of SPIE - The International Society for Optical Engineering*, volume 5316, pages 78–84, 2004.

K. A. Faccenda and B. T. Finucane. Complications of regional anaesthesia: Incidence and prevention. *Drug Safety*, 24(6):413–442, 2001.

T. J. Farrell, M. S. Patterson, and B. Wilson. A diffusion theory model of spatially resolved, steady-state diffuse reflectance for the noninvasive determination of tissue optical properties in vivo. *Medical Physics*, 19(4), 1992.

T. Fivez, S. Deblonde, and M. Van De Velde. Late intravascular migration of a previously well functioning labour epidural catheter. *European journal of anaesthesiology*, 27(7):634–636, 2010.

M. Friebel, A. Roggan, G. Mueller, and M. Meinke. Determination of optical properties of human blood in the spectral range 250 to 1100 nm using monte carlo simulations with hematocrit-dependent effective scattering phase functions. *Journal of Biomedical Optics*, 11(3), May-Jun 2006.

M. Friebel, J. Helfmann, U. Netz, and M. Meinke. Influence of oxygen saturation on the optical scattering properties of human red blood cells in the spectral range 250 to 2000 nm. *Journal of Biomedical Optics*, 14(3), 2009.

K. E. Friedl, J. P. DeLuca, L. J. Marchitelli, and J. A. Vogel. Reliability of body-fat estimations from a four-compartment model by using density, body water, and bone mineral measurements. *American Journal of Clinical Nutrition*, 55(4): 764–770, 1992.

C. Friedrich, M. P. Mienkina, C. Brenner, N. C. Gerhardt, M. Jörger, A. Strauß, M. F. Beckmann, G. Schmitz, and M. R. Hofmann. Quantitative photoacoustic blood oxygenation measurement of whole porcine blood samples using a multi-wavelength semiconductor laser system. In *Progress in Biomedical Optics and Imaging - Proceedings of SPIE*, volume 8088, 2011.

Fujifilm. Colonoscopes (product site). `http://www.fujifilmusa.com/products/fujinon_endoscopy/endoscopes/colonoscopes`.

D. S. Gareau, F. Truffer, K. Perry, T. Pham, C. K. Enestvedt, J. Dolan, J. G. Hunter, and S. L. Jacques. Optical fiber probe spectroscopy for laparoscopic monitoring of tissue oxygenation during esophagectomies. *Journal of Biomedical Optics*, 15 (6), Nov-Dec 2010.

M. C. Guilbert, S. Elkouri, D. Bracco, M. M. Corriveau, N. Beaudoin, M. J. Dubois, L. Bruneau, and J. F. Blair. Arterial trauma during central venous catheter insertion: Case series, review and proposed algorithm. *Journal of Vascular Surgery*, 48(4):918–925, 2008.

Z. Guo, L. Li, and L. V. Wang. On the speckle-free nature of photoacoustic tomography. *Medical Physics*, 36(9):4084–4088, 2009.

M. Hall, E. Frank, G. Holmes, B. Pfahringer, P. Reutemann, and I. H. Witten. The weka data mining software: An update. *SIGKDD Explorations*, 11(1), 2009.

M. Hammer, D. Schweitzer, B. Michel, E. Thamm, and A. Kolb. Single scattering by red blood cells. *Applied Optics*, 37(31):7410–7418, 1998.

M. Hammer, A. N. Yaroslavsky, and D. Schweitzer. A scattering phase function for blood with physiological haematocrit. *Physics in Medicine and Biology*, 46(3), 2001.

J. C. Hu, X. Gu, S. R. Lipsitz, M. J. Barry, A. V. D'Amico, A. C. Weinberg, and N. L. Keating. Comparative effectiveness of minimally invasive vs open radical prostatectomy. *Journal of the American Medical Association*, 302(14):1557–1564, 2009.

N. A. Kama, M. Doganay, M. Dolapci, E. Reis, M. Atli, and M. Kologlu. Risk factors resulting in conversion of laparoscopic cholecystectomy to open surgery. *Surgical Endoscopy*, 15(9):965–968, 2001.

N. S. Kapany and N. Silbertrust. Fibre optics spectrophotometer for in vivo oximetry. *Nature*, 204:138–&, 1964.

H. Kehlet and D. W. Wilmore. Multimodal strategies to improve surgical outcome. *American Journal of Surgery*, 183(6):630–641, 2002.

M. D. Keller, S. K. Majumder, M. C. Kelley, I. M. Meszoely, F. I. Boulos, G. M. Olivares, and A. Mahadevan-Jansen. Autofluorescence and diffuse reflectance spectroscopy and spectral imaging for breast surgical margin analysis. *Lasers in Surgery and Medicine*, 42(1):15–23, 2010.

C. Kim, T. N. Erpelding, W. J. Akers, K. Maslov, L. Song, L. Jankovic, J. A. Margenthaler, S. Achilefu, and L. V. Wang. Photoacoustic image-guided needle biopsy of sentinel lymph nodes. In *Progress in Biomedical Optics and Imaging - Proceedings of SPIE*, volume 7899, 2011.

Chulhong Kim, Todd N. Erpelding, Ladislav Jankovic, Michael D. Pashley, and Lihong V. Wang. Deeply penetrating in vivo photoacoustic imaging using a clinical ultrasound array system. *Biomedical Optics Express*, 1(1):278–284, Aug 2 2010.

S. Koizuka, K. Nakajima, and R. Mieda. Ct-guided nerve block: A review of the features of ct fluoroscopic guidance for nerve blocks. *Journal of Anesthesia*, 28 (1):94–101, 2014.

P. G. Kranz, P. Raduazo, L. Gray, R. K. Kilani, and J. K. Hoang. Ct fluoroscopy-guided cervical interlaminar steroid injections: Safety, technique, and radiation dose parameters. *American Journal of Neuroradiology*, 33(7):1221–1224, 2012.

J. Laufer, C. Elwell, D. Delpy, and P. Beard. Pulsed near-infrared photoacoustic spectroscopy of blood. In *Progress in Biomedical Optics and Imaging - Proceedings of SPIE*, volume 5, pages 57–68, 2004.

J. Laufer, C. Elwell, D. Delpy, and P. Beard. In vitro measurements of absolute blood oxygen saturation using pulsed near-infrared photoacoustic spectroscopy: Accuracy and resolution. *Physics in Medicine and Biology*, 50(18):4409–4428, 2005.

J. Laufer, E. Zhang, and P. Beard. Quantitative in vivo measurements of blood oxygen saturation using multiwavelength photoacoustic imaging. In *Progress in Biomedical Optics and Imaging - Proceedings of SPIE*, volume 6437, 2007.

Edwards Lifesciences. Theory and clinical application of continuous fiberoptic central venous oximetry monitoring. `http://ht.edwards.com/scin/edwards/sitecollectionimages/products/mininvasive/ar06577-preseptheoryclinicalapp_1lr.pdf`, 2011.

S. P. Lin, M. S. Mandell, Y. Chang, P. T. Chen, M. Y. Tsou, K. H. Chan, and C. K. Ting. Discriminant analysis for anaesthetic decision-making: An intelligent recognition system for epidural needle insertion. *British Journal of Anaesthesia*, 108(2):302–307, 2012.

W. Lin, S. A. Toms, M. Johnson, E. D. Jansen, and A. Mahadevan-Jansen. In vivo brain tumor demarcation using optical spectroscopy. *Photochemistry and photobiology*, 73(4):396–402, 2001.

Q. Liu and T. Vo-Dinh. Spectral filtering modulation method for estimation of hemoglobin concentration and oxygenation based on a single fluorescence emission spectrum in tissue phantoms. *Medical Physics*, 36(10):4819–4829, 2009.

J. Machi, B. Sigel, T. Kurohiji, H. A. Zaren, and J. Sariego. Operative ultrasound guidance for various surgical procedures. *Ultrasound in Medicine and Biology*, 16 (1):37 – 42, 1990. ISSN 0301-5629. doi: 10.1016/0301-5629(90)90084-P.

S. J. Madsen, M. S. Patterson, and B. C. Wilson. The use of india ink as an optical absorber in tissue-simulating phantoms. *Physics in Medicine and Biology*, 37(4): 985–993, 1992.

S. Manohar, S. E. Vaartjes, J. C. G. Van Hespen, J. M. Klaase, F. M. Van Den Engh, W. Steenbergen, and T. G. Van Leeuwen. Initial results of in vivo non-invasive cancer imaging in the human breast using near-infrared photoacoustics. *Optics Express*, 15(19):12277–12285, 2007.

P. Marhofer and V. W. S. Chan. Ultrasound-guided regional anesthesia: Current concepts and future trends. *Anesthesia and Analgesia*, 104(5):1265–1269, 2007.

D. McKay and G. Blake. Optimum incision length for port insertion in laparoscopic surgery. *Annals of the Royal College of Surgeons of England.*, 88(1):78, 2006.

M. Meinke, G. Müller, J. Helfmann, and M. Friebel. Optical properties of platelets and blood plasma and their influence on the optical behavior of whole blood in the visible to near infrared wavelength range. *Journal of Biomedical Optics*, 12 (1), 2007.

G. B. Meloni, M. P. Becchere, D. Soro, C. F. Feo, S. Profili, G. Dettori, M. Trignano, G. Navarra, and G. C. Canalis. Percutaneous vacuum-assisted core breast biopsy with upright stereotactic equipment indications, limitations and results. *Acta radiologica*, 43(6):575–578, 2002.

R. Michels, F. Foschum, and A. Kienle. Optical properties of fat emulsions. *Optics Express*, 16(8):5907–5925, 2008.

MicroGroup. Hypodermic tubing. `http://www.microgroup.com/capabilities/cutsom_sizing_shaping.asp`.

R. Miller and M. C. Pardo Jr. *Basics of anesthesia*. Elsevier/Saunders, Philadelphia, PA, 2011. ISBN 1437716148.

G. A. Millikan. The oximeter, an instrument for measuring continuously the oxygen saturation of arterial blood in man. *Review of Scientific Instruments*, 13(10): 434–444, 1942.

M. F. Mulroy. Systemic toxicity and cardiotoxicity from local anesthetics: Incidence and preventive measures. *Regional anesthesia and pain medicine*, 27(6):556–561, 2002.

R. Nachabé, B. H. W. Hendriks, A. E. Desjardins, M. Van Der Voort, M. B. Van Der Mark, and H. J. C. M. Sterenborg. Estimation of lipid and water concentrations in scattering media with diffuse optical spectroscopy from 900 to 1600 nm. *Journal of Biomedical Optics*, 15(3), 2010.

A. Nima-Shariat, P. M Horan, K. Gratenstein, C. McCally, and A. P. Frulla. Equipment for peripheral nerve blocks. `http://www.nysora.com/regional-anesthesia/foundations-of-ra/3009-equipment-for-peripheral-nerve-block.html`, 2013.

G. A. Nuttall, W. C. Oliver Jr., M. H. Ereth, P. J. Santrach, S. C. Bryant, T. A. Orszulak, and H. V. Schaff. Comparison of blood-conservation strategies in cardiac surgery patients at high risk for bleeding. *Anesthesiology*, 92(3):674–682, 2000.

W. C. Oliver Jr., G. A. Nuttall, F. M. Beynen, H. S. Raimundo, J. P. Abenstein, and J. J. Arnold. The incidence of artery puncture with central venous cannulation using a modified technique for detection and prevention of arterial cannulation. *Journal of Cardiothoracic and Vascular Anesthesia*, 11(7):851–855, 1997.

A. A. Oraevsky, S. L. Jacques, and F. K. Tittel. Measurement of tissue optical properties by time-resolved detection of laser-induced transient stress. *Applied Optics*, 36(1):402–415, 1997.

Pajunk. Epilong and epispin systems for epidural anesthesia. `http://www.pajunk.com.cn/pdf/EpilongEpispin.pdf`.

C. J. Pallister and Watson M.S. *Haematology*. Scion Publishing Ltd, Banbury, second edition, 2011. ISBN 9781904842392.

G. Palumbo and R. Prates, editors. *Lasers and Current Optical Techniques in Biology*. Royal Society of Chemistry, 2004.

M. S. Patterson, B. C. Wilson, and D. R. Wyman. The propagation of optical radiation in tissue i. models of radiation transport and their application. *Lasers in Medical Science*, 6(2):155–168, 1991.

Daniele Piras, Chiel Grijsen, Peter Schutte, Wiendelt Steenbergen, and Srirang Manohar. Photoacoustic needle: minimally invasive guidance to biopsy. *Journal of Biomedical Optics*, 18(7), Jul 2013.

M. L. Polanyi and R. M. Hehir. New reflection oximeter. *Review of Scientific Instruments*, 31(4):401–403, 1960.

M. L. Polanyi and R. M. Hehir. In vivo oximeter with fast dynamic response. *Review of Scientific Instruments*, 33(10):1050–1054, 1962.

S. Prahl. Optical properties spectra. `http://omlc.ogi.edu/spectra`.

S. A. Prahl, M. Keijzer, S. L. Jacques, and A. J. Welch. A Monte Carlo Model of Light Propagation in Tissue. In G. J. Müller and D. H. Sliney, editors, *SPIE Proceedings of Dosimetry of Laser Radiation in Medicine and Biology*, volume IS 5, pages 102–111, 1989.

B. C. Quirk, R. A. McLaughlin, A. Curatolo, R. W. Kirk, P. B. Noble, and D. D. Sampson. In situ imaging of lung alveoli with an optical coherence tomography needle probe. *Journal of Biomedical Optics*, 16(3), 2011.

J. P. Rathmell, A. E. Desjardins, M. Van Der Voort, B. H. W. Hendriks, R. Nachabe, S. Roggeveen, D. Babic, M. Söderman, M. Brynolf, and B. Holmström. Identification of the epidural space with optical spectroscopy: An in vivo swine study. *Anesthesiology*, 113(6):1406–1418, 2010.

M. A. Reina, A. López García, J. A. De Andrés, F. Sellers, M. Arrizabalaga, and M. J. Mora. Variation in the thickness of the dural sac. *Revista Española de Anestesiología y Reanimación.*, 46(8):344–349, 1999.

M. A. Reina, P. Pulido, J. Castedo, M. C. Villanueva, A. López, and R. G. Sola. Characteristics and distribution of normal human epidural fat. *Revista Española de Anestesiología y Reanimación.*, 53(6):363–372, 2006.

M. A. Reina, P. Pulido, J. Castedo, M. C. Villanueva, A. López, J. A. De Andrés, and R. G. Sola. Epidural fat in various diseases: contribution of magnetic resonance imaging and potential implications for neuro axial anesthesia. *Revista Española de Anestesiología y Reanimación.*, 54(3):173–183, 2007.

M. A. Reina, M. C. Villanueva, F. Machés, A. Carrera, A. López, and J. A. De Andrés. The ultrastructure of the human spinal nerve root cuff in the lumbar spine. *Anesthesia and Analgesia*, 106(1):339–344, 2008.

M. Reuber, L. A. Dunkley, E. P. L. Turton, M. D. D. Bell, and J. M. Bamford. Stroke after internal jugular venous cannulation. *Acta Neurologica Scandinavica*, 105(3):235–239, 2002.

L. O. Reynolds and N. J. McCormick. Approximate two-parameter phase function for light scattering. *Journal of the Optical Society of America*, 70(10):1206–1212, 1980.

C. Robards, S. Clendenen, and R. Greengrass. Intravascular injection during ultrasound-guided axillary block: Negative aspiration can be misleading. *Anesthesia and Analgesia*, 107(5):1754–1755, 2008.

B. Roe. C version of ranmar and rmarin. `http://www-mhp.physics.lsa.umich.edu/~roe/ranmar.c`.

K. Rogers. *Blood: Physiology and Circulation*. Human body. Britannica Educational Pub., 2010. ISBN 9781615301218.

A. Roggan, M. Friebel, K. Dörschel, A. Hahn, and G. Müller. Optical properties of circulating human blood in the wavelength range 400-2500 nm. *Journal of Biomedical Optics*, 4(1):36–46, 1999.

S. Y. Ryu, J. Na, H. Y. Choi, Z. Ding, and B. H. Lee. Double clad fiber devices for combined oct-fs system. In *2008 Asia Optical Fiber Communication and Optoelectronic Exposition and Conference, AOE 2008*, 2008.

S. Y. Ryu, H. Y. Choi, M. J. Ju, J. Na, W. J. Choi, and B. H. Lee. The development of double clad fiber and double clad fiber coupler for fiber based biomedical imaging systems. *Journal of the Optical Society of Korea*, 13(3):310–315, 2009.

L. M. Schnapp and N. H. Cohen. Pulse oximetry; uses and abuses. *Chest*, 98(5): 1244–1250, 1990.

E. M. Sevick, B. Chance, J. Leigh, S. Nioka, and M. Maris. Quantitation of time- and frequency-resolved optical spectra for the determination of tissue oxygenation. *Analytical Biochemistry*, 195(2):330–351, 1991.

P. M. Shah, S. C. Babu, A. Goyal, R. B. Mateo, and R. E. Madden. Arterial misplacement of large-caliber cannulas during jugular vein catheterization: Case for surgical management. *Journal of the American College of Surgeons*, 198(6): 939–944, 2004.

V. Sharma, J.W. He, S. Narvenkar, Y. B. Peng, and H. Liu. Quantification of light reflectance spectroscopy and its application: Determination of hemodynamics on the rat spinal cord and brain induced by electrical stimulation. *Neuroimage*, 56 (3):1316–1328, Jun 1 2011.

N.K. Shinton, editor. *Desk Reference for Hematology*. CRC desk reference series. Second edition, 2007. ISBN 9780849333934.

B. D. Sites, A. H. Taenzer, M. D. Herrick, C. Gilloon, J. Antonakakis, J. Richins, and M. L. Beach. Incidence of local anesthetic systemic toxicity and postoperative neurologic symptoms associated with 12,668 ultrasound-guided nerve blocks: An analysis from a prospective clinical registry. *Regional anesthesia and pain medicine*, 37(5):478–482, 2012.

Jimmy Su, Andrei Karpiouk, Bo Wang, and Stanislav Emelianov. Photoacoustic imaging of clinical metal needles in tissue. *Journal of Biomedical Optics*, 15(2), Mar-Apr 2010.

Jimmy L. Su, Andrei B. Karpiouk, Yun-Sheng Chen, and Stanislav Y. Emelianov. Photoacoustic imaging to guide needle injections. In AA Oraevsky and LV Wang, editors, *Photons plus Ultrasound: Imaging and Sensing 2011*, volume 7899 of *Proceedings of SPIE*, 2011.

S. Takatani and J. Ling. Optical oximetry sensors for whole blood and tissue. *IEEE Engineering in Medicine and Biology Magazine*, 13(3):347–357, 1994.

Terumo. Finecross®MG-Coronary Micro-Guide Catheter. `http://www.terumo-europe.com/cardiology/products/finecross-mg_coronary_micro_guide_catheter.php`.

The Royal College of Anaesthetists. Anaesthesia explained (2008). `http://www.rcoa.ac.uk/system/files/PI-AE-2008.pdf`.

T. P. Thomas, Y. C. Ye, J. Y.and Chang, A. Kotlyar, Z. Cao, I. J. Majoros, T. B. Norris, and J. R. Baker, Jr. Investigation of tumor cell targeting of a dendrimer nanoparticle using a double-clad optical fiber probe. *Journal of Biomedical Optics*, 13(1), Jan-Feb 2008.

C. Ting, M. Tsou, P. Chen, K. Chang, M. S. Mandell, K. Chan, and Y. Chang. A new technique to assist epidural needle placement: Fiberoptic-guided insertion using two wavelengths. *Anesthesiology*, 112(5), 2010.

P. Trubiano, E. J. Heyer, D. C. Adams, D. J. McMahon, I. Christiansen, E. A. Rose, and E. Delphin. Jugular venous bulb oxyhemoglobin saturation during cardiac surgery: Accuracy and reliability using a continuous monitor. *Anesthesia and Analgesia*, 82(5):964–968, 1996.

V.V. Tuchin. *Handbook of Optical Biomedical Diagnostics*. Press Monographs. Society of Photo Optical, 2002. ISBN 9780819442383.

UC Davis Vascular Center. Pseudoaneurysm evaluation and treatment. `http://www.ucdmc.ucdavis.edu/vascular/lab/exams/pseudoaneurysm.html`.

UC Irvine School of Medicine. Central line procedures. `http://www.anesthesiology.uci.edu/clinical_centralline.shtml`.

U. Utzinger and R. Richards-Kortum. Fiber optic probes for biomedical optical spectroscopy. *Journal of Biomedical Optics*, 8(1):121–147, Jan 2003. doi: 10.1117/1.1528207.

A. L. Wagner. Ct fluoroscopy-guided epidural injections: Technique and results. *American Journal of Neuroradiology*, 25(10):1821–1823, 2004.

J. L. Waller, J. A. Kaplan, D. I. Bauman, and J. M. Craver. Clinical-evaluation of a new fiberoptic catheter oximeter during cardiac-surgery. *Anesthesia and Alagesia*, 61(8):676–679, 1982.

B. Wang, J. L. Su, J. Amirian, S. H. Litovsky, R. Smalling, and S. Emelianov. Detection of lipid in atherosclerotic vessels using ultrasound-guided spectroscopic intravascular photoacoustic imaging. *Optics Express*, 18(5):4889–4897, 2010.

B. Wang, A. Karpiouk, D. Yeager, J. Amirian, S. Litovsky, R. Smalling, and S. Emelianov. In vivo intravascular ultrasound-guided photoacoustic imaging of lipid in plaques using an animal model of atherosclerosis. *Ultrasound in Medicine and Biology*, 38(12):2098–2103, 2012.

H. W. Wang, J. K. Jiang, C. H. Lin, J. K. Lin, G. J. Huang, and J. S. Yu. Diffuse reflectance spectroscopy detects increased hemoglobin concentration and decreased oxygenation during colon carcinogenesis from normal to malignant tumors. *Optics Express*, 17(4):2805–2817, Feb 16 2009.

L. Wang, H. Y. Choi, Y. Jung, B. H. Lee, and K. Kim. Optical probe based on double-clad optical fiber for fluorescence spectroscopy. *Optics Express*, 15(26):17681–17689, 2007.

L. H. Wang, S. L. Jacques, and L. Q. Zheng. Mcml - monte-carlo modeling of light transport in multilayered tissues. *Computer Methods and Programs in Biomedicine*, 47(2):131–146, Jul 1995.

L. V. Wang. Multiscale photoacoustic microscopy and computed tomography. *Nature Photonics*, 3(9):503–509, 2009.

L. V. Wang and H. I. Wu. *Biomedical optics : principles and imaging*. Wiley-Interscience, Hoboken, N.J, 2007. ISBN 9780471743040.

W. White. Perfluorinated graded index plastic optical fiber gigapof ®. `http://www.chromisfiber.com/pdf/OFC2010Wwhite1105.pdf`.

M. Wiegel, U. Gottschaldt, R. Hennebach, T. Hirschberg, and A. Reske. Complications and adverse effects associated with continuous peripheral nerve blocks in orthopedic patients. *Anesthesia and Analgesia*, 104(6):1578–1582, 2007.

A. N. Yaroslavsky, I. V. Yaroslavsky, T. Goldbach, and H. Schwarzmaier. Influence of the scattering phase function approximation on the optical properties of blood determined from the integrating sphere measurements. *Journal of Biomedical Optics*, 4(1):47–53, 1999.

Anna N. Yaroslavsky, Ilya V. Yaroslavsky, Thomas Goldbach, and Hans-Joachim Schwarzmaier. Optical properties of blood in the near-infrared spectral range. In *Proceedings of SPIE - The International Society for Optical Engineering*, volume 2678, pages 314–324, 1996.

H. Y. Yu, Y. W. Chiu, H. H. Lin, T. C. Chang, and Y. Z. Shen. Blood content in guinea-pig tissues: Correction for the study of drug tissue distribution. *Pharmacological Research*, 23(4):337–347, 1991.

J. Zubia and J. Arrue. Plastic optical fibers: An introduction to their technological processes and applications. *Optical Fiber Technology*, 7(2):101–140, 2001.